uOttawa

UNCOVERING THE PHYSICAL CONTROLS OF SLOW SLIP ALONG CASCADIA AND OTHER GLOBAL ACTIVE TECTONIC MARGINS

BY

MORGAN ELYSE MCLELLAN

B.SC., UNIVERSITY OF OTTAWA

M.SC., UNIVERSITY OF OTTAWA

A thesis submitted to the University of Ottawa

in partial fulfillment of the thesis requirement for the degree of

DOCTOR OF PHILOSOPHY

IN

EARTH AND ENVIRONMENTAL SCIENCES

FACULTY OF SCIENCE

EXAMINING COMMITTEE

The following served on the Examining Committee for this thesis.

External Examiner: Yajing Liu
Professor, Dept. of Earth and Planetary Sciences
McGill University

Internal Members: Glenn Milne
Professor, Dept. of Earth and Environmental Sciences
University of Ottawa

Claire Perry
Seismologist, Dept. of Natural Resources Canada
Adjunct Professor, Dept. of Earth and Environmental Sciences
University of Ottawa

Maurice Lamontagne
Adjunct Professor, Dept. of Earth Sciences
Carleton University

Supervisor: Pascal Audet
Professor, Dept. of Earth and Environmental Sciences
University of Ottawa

DECLARATION

I hereby declare that the work described here represents the results of original research preformed while I was a candidate for the degree of Doctor of Philosophy at the University of Ottawa under the supervision of Dr. Pascal Audet.

Morgan E. McLellan
November, 2022

PUBLICATION LIST

Chapter I is published as the following article:

1. McLellan, M. and Audet, P. (2020). Uncovering the physical controls of subduction zone slow slip using supervised classification of subducting plate features. Geophysical Journal International. 223(1): 94-110
   I conceptualized this study, as well as contributed to development of software coded in the programming language PYTHON. I collected the geospatial data from online public data sources as well as conducted a full literature review to determine the locations of observed slow slip to use as input to machine learning models. I also wrote the article with input from my co-author. This paper is published in *Geophysical Journal International.*

Chapter II is published as the following article:

2. McLellan, M., Audet, P., Rosas, J.C., Currie, C. (2022). Margin-wide variations in slab dehydration in Cascadia and their relationship to slow slip. Lithos. 434-435, 10.1016/j.lithos.2022.106912
   I conceptualized this study as well as developed thermal models using the software PGCTherm2D. I conducted a full literature review to determine key parameter values as input to the thermal models. I used the outputs of the thermal models to determine fluid flux rates by employing a previously applied petrologic model. I also wrote this article with input from my co-authors. This paper is published in *Lithos.*

Chapter III is in preparation for submission as:

3. McLellan, M., Audet, P. Serpentinization of the Cascadia mantle wedge corner and its relationship to slow slip. *In prep.*
   I applied a novel receiver function inversion code to real data to estimate parameters associated with subsurface structure. I interpreted the results and wrote the article with input from my co-author. This paper is in preparation for submission.

ACKNOWLEDGEMENTS

This thesis was made possible with the support and guidance of many people over the past 5 years. Firstly, I would like to thank my supervisor, Pascal Audet, for giving me the opportunity to work on many interesting research topics. This thesis represents the culmination of nearly 10 years of collaboration in which I have developed an eagerness to explore challenging problems and the skills to tackle them.

I extend sincere gratitude to my collaborators who lent their expertise to allow for my ideas to reach their full potential. I thank Claire Currie for her insightful discussions and Juan Rosas for his technical support in learning new and challenging software.

I would like to thank all members of the University of Ottawa geophysics group. Thank you to Jeremy, Clement, Steve, and Hao for all the advice and suggestions given at our group meetings in the pre-pandemic phase of my PhD! I also extend thanks to the rest of the geophysics group: Taylor, Quan, Erica, and Pasan.

Thank you to all my friends and family who have provided unending support through all the ups and downs of the past five years. I could not have done it without you.

I would like to extend a very special thank you to my Mother, who has provided unwavering support for the past year as I balanced my research and my new role as a mother. Thank you for always pushing me to be my best and being a continuing source of inspiration in my life.

Finally, I would like to thank my husband, Anthony, and son, Everett for all their love and support. Anthony, you have been a constant source of motivation as I have pursued my research, from beginning my masters 8 years ago to completing my PhD. Everett, you bring so much joy to my life and make each day worth it. For that I am forever grateful.

To my son Everett,

TABLE OF CONTENTS

LIST OF TABLES

LIST OF FIGURES

LIST OF IMPORTANT ACRONYMS

CSZ	Cascadia Subduction Zone
ETS	Episodic Tremor and Slip
GNB	Gaussian Naïve Bayes
GNSS	Global Navigation Satellite Systems
GPS	Global Positioning System
KNN	K Nearest Neighbour
LDA	Linear Discriminant Analysis
LR	Logistic Regression
LVL	Low Velocity Layer
MORB	Mid-Ocean Ridge Basalt
M_w	Moment Magnitude
NOAA	National Oceanic and Atmospheric Administration
P-T	Pressure-Temperature
RF	Random Forest (Chapter I)
RF	Receiver Function (Chapter III)
SSE	Slow Slip Event
SVM	Support Vector Machine

SUMMARY

The discovery of slow slip, an intermediary form of strain release characterized by slow slip rates, has been one of the most important advances in seismology in recent decades. We attempt to further our understanding of the physical controls of slow slip in subduction zones using three different approaches. We generate and train statistical learning models through supervised classification with the goal of determining the relationship between five subduction zone parameters and slow slip observations. These parameters include subducting plate age, relative plate velocity, sediment thickness entering the trench, slab dip, and seafloor roughness. We find that young subducting lithosphere is strongly correlated with slow slip in the case of short-term events but not in the case of long-term events. We use the trained models to predict slow slip observations in regions that are sparsely instrumented. Slow slip is predicted to occur in many subduction zones globally, most notably in South America where it is expected to be widespread. In our second approach, we generate thermal models along strike in Cascadia to estimate fluid flux rates near the depths of observed slow slip. We observe a correlation between shorter recurrence times for slow slip and higher fluid flux rates near the location of the mantle wedge corner. This provides support for models where the recurrence interval is dependent on the rate of processes that generate and trap fluids. Finally, we use teleseismic receiver functions to characterize seismic anisotropy in the Cascadia mantle wedge corner. We examine the potential role that widespread serpentinization may have in generating the conditions for slow slip. We observe seismic P-to-S velocity ratio (Vp/Vs) values that are consistent with 40-50% serpentinization. A slow axis of symmetry is estimated, which corresponds with subparallel foliation consistent with a serpentinized shear zone being deformed by the downgoing slab. Overall, these results provide further constraints on the physical controls of slow slip, and thus stress accommodation in subduction zones as a whole. As subduction zones are the site of some of the most devastating earthquakes on Earth, furthering our understanding of subduction zone processes is critical for improving earthquake hazard mitigation efforts.

PART I: INTRODUCTION

1

1.1 EARTHQUAKES IN SUBDUCTION ZONES

Subduction zones are the regions where the dense oceanic lithosphere is driven beneath the more buoyant continental lithosphere. The sinking of the oceanic lithosphere is the driving force behind plate movement (i.e., plate tectonics), making it a central feature of the Earth system as whole. The forces generated by the weight of the subducting slab as it pulls the rest of the plate cause mid-ocean ridges to spread, creating new lithosphere, where it is then recycled in a subduction zone. This mechanism delivers oceanic lithosphere, sediments and fluids into the overlying continental mantle which triggers the melting responsible for creating the continental crust. The entire subduction system is the source of diverse geological phenomena including volcanism, orogenesis, accretionary prisms, and arc-trench complexes (Fig. 1.1). This process has far-reaching societal implications, as they produce megathrust earthquakes which release substantial amounts of energy causing intense ground shaking and tsunamis. They are thus some of the most destructive earthquakes on earth, making the understanding of stress release mechanisms critical.

Subduction zones exist on a spectrum where they display different back-arc structures, depths of seismicity, and levels of volcanism (Stern, 2002). These differences largely depend on the pressure-temperature (P-T) structure of the subduction zone which is primarily constrained by the age of the incoming oceanic crust. Old lithosphere has substantially cooled, since its creation at spreading ridges, resulting in a cold, dense slab, while young lithosphere remains hot and more buoyant. Due to its increased density, old lithosphere readily sinks creating a steeply dipping plate. Young lithosphere, on the other hand, resists subduction resulting in shallower dips (Fig. 1.2) (Jarrard, 1986). As a result of contrasting thermal structure and plate geometry, the stress regime in the back-arc differs substantially in each case. The young lithosphere endmember generally produces a compressional regime in the back-arc, resulting in significant crustal seismicity, while

extension is observed in the case of old lithosphere. Additionally, the P-T structure of a subduction zone has important implications with respect to the nature of stress accommodation. Our traditional understanding of stress release within subduction zones involves two types of behaviour: earthquakes, where elastic strain is suddenly released causing ground shaking and stable sliding, where rocks follow the ductile regime and the two plates slide past one another. The difference in mechanism is a response to the changing physical conditions at the plate interface, most importantly the change in pressure and temperature conditions that control the rheological behaviour of the rocks (Hyndman and Wang, 1993).

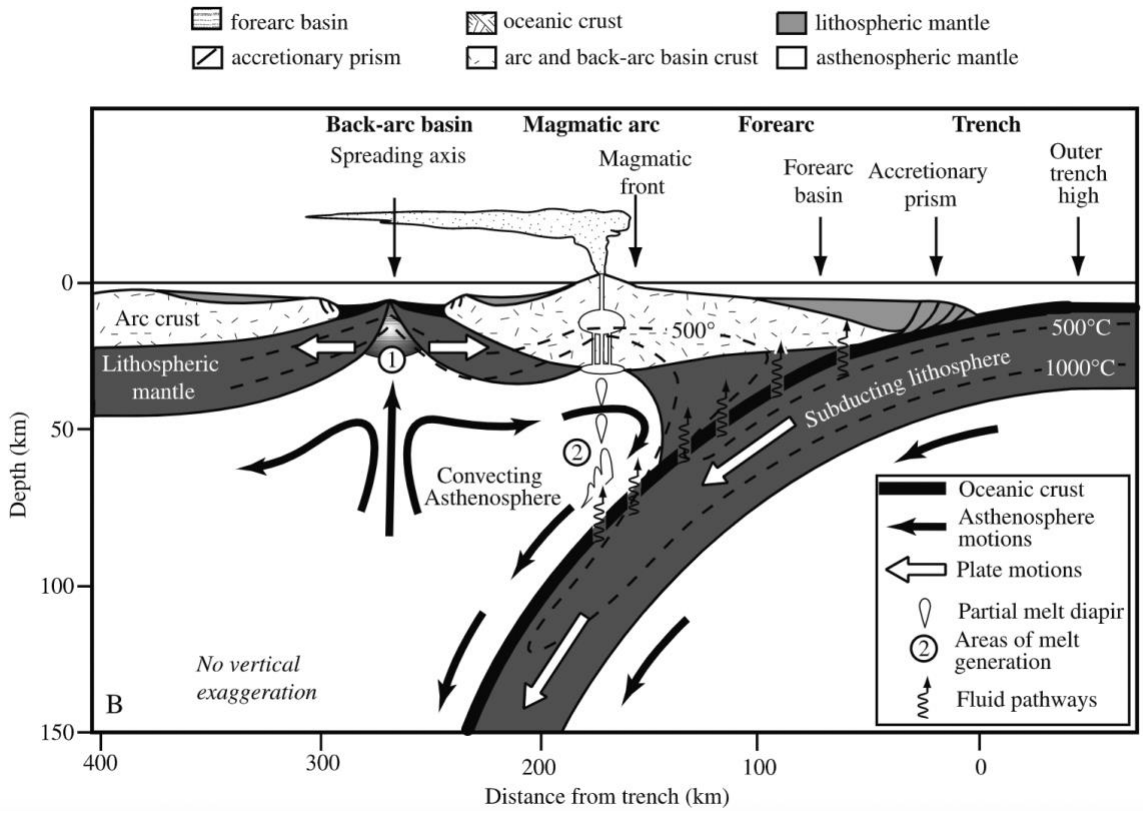

FIGURE 1.1 SCHEMATIC DIAGRAM OF A SUBDUCTION ZONE WITH IMPORTANT STRUCTURAL COMPONENTS HIGHLIGHTED INCLUDING THE TRENCH, FOREARC, MAGMATIC ARC, AND BACK-ARC BASIN. GEOLOGICAL PHENOMENA PRODUCED IN THESE SETTINGS ARE DISPLAYED INCLUDING THE ACCRETIONARY PRIM AND VOLCANISM. NUMBER 1 INDICATES THE PROCESS OF BACK-ARC SPREADING WHICH IS OBSERVED IN OLD/COLD, STEEPLY DIPPING SUBDUCTION ZONES. NUMBER 2 INDICATES THE PROCESS OF MELT GENERATION AS FLUIDS ARE RELEASED VIA METAMORPHIC DEHYDRATION REACTIONS AND ARE INTRODUCTED INTO THE OVERRIDING CONTINENTAL LITHOSPHERE. (STERN, 2002)

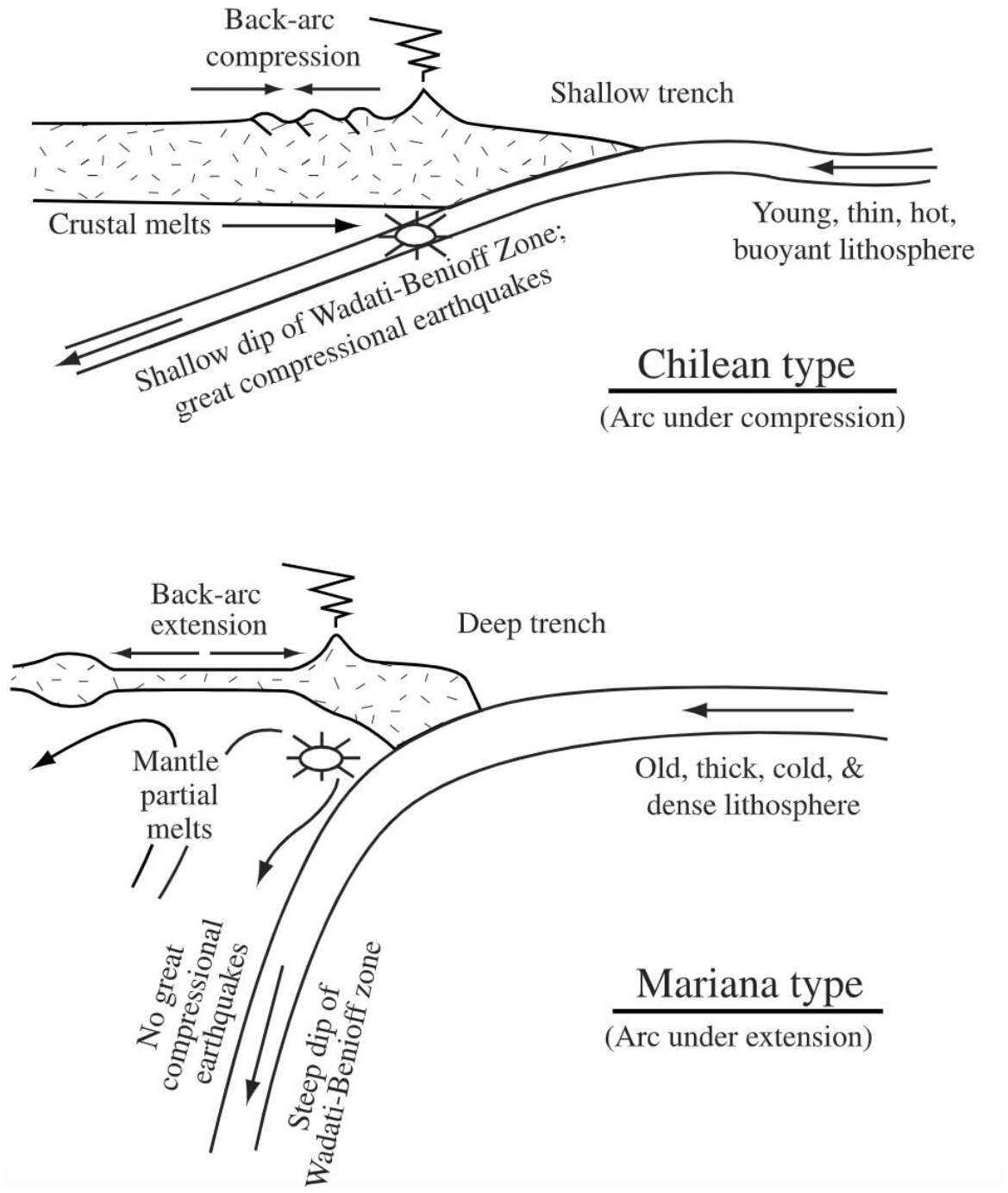

FIGURE 1.2: SUBDUCTION ZONE ENDMEMBERS BASED ON AGE OF SUBDUCTING LITHOSPHERE. YOUNG LITHOSPHERE RESULTS IN A HOT BUOYANT SLAB LEADING TO A SHALLOW DIP AND BACK-ARC COMPRESSION. OLD LITHOSPHERE RESULTS IN A COLD DENSE SLAB LEADING TO A STEEP DIP AND BACK-ARC EXTENSION. (STERN, 2002).

At shallow depths (<50 km), stress is accommodated through fault rupture, which is a consequence of the coupling between the subducting and overriding plate in a region known as the seismogenic zone. The continuous convergence of the incoming plate with the overriding plate leads to the periodic accumulation and release of elastic strain known as the earthquake cycle. This cycle is defined by three phases which include (1) the inter-seismic phase, where the plates are locked (no slip) and strain is accumulating, (2) the co-seismic phase, where sudden rupture occurs, releasing the accumulated strain, and (3) the post-seismic phase where the fault and surrounding material adjust visco-elastically to the modified stress state. This final phase may consist of minor instances of slip called aftershocks. In standard models of stick-slip (i.e., earthquakes) friction, failure is observed when the ratio of shear stress to normal stress on the surface reaches a critical value μ_s, known as the static coefficient of friction. Once sliding begins, the fault weakens and the frictional resistance decreases to a value known as the dynamic coefficient of friction, μ_d (Scholz, 1998). Rate and state dependent friction (Fig. 1.3) (Dieterich, 1979; Ruina, 1983) describes the relationship between slip behaviour and velocity, time, and slip distance based on experimental data and is defined by:

$$\tau = \left[\mu_0 + aln\left(\frac{V}{V_0}\right) + bln\left(\frac{V_0\theta}{\mathcal{L}}\right)\right]\bar{\sigma}, \qquad \textit{Eq. 1.1}$$

where τ is shear stress, μ_0 is the steady state coefficient at slip rate V_0, V is the slip rate, a and b are material constants, $\mathcal{L}$ is the characteristic slip distance following velocity steps and $\bar{\sigma}$ is the effective normal stress defined as:

$$\bar{\sigma} = \sigma - \sigma_P, \qquad \textit{Eq. 1.2}$$

where σ is the applied normal stress and σ_P is the pore-fluid pressure. Here, elevated pore-fluid pressures weaken the frictional strength of a fault by decreasing the effective normal stress. Velocity-weakening behaviour (when b > a) describes the case in which the frictional resistance of the fault decreases faster than the stress reduction due to movement. This is the behaviour that is observed with earthquakes and are associated with sudden drops in stress. Velocity-strengthening behaviour (when a > b) describes the opposite case in which a decrease in strength is not observed and stable sliding occurs.

The values of parameters a and b are dependent on material properties that vary based on temperature and pressure.

With increasing depth, and thus temperature, a fault will transition from velocity weakening to velocity strengthening frictional behaviour. This transition is observed in subduction zones where the seismogenic zone terminates at temperatures of ~350°C associated with the brittle-ductile transition of continental crustal compositions, and in warm subduction zones will mark the transition from seismic to aseismic behaviour (Hyndman and Wang, 1993). In the case of dry mantle rocks, this transition is observed between 600-800°C (Kirby, 1983), thus we would expect to observe seismic behaviour extend downward into the mantle wedge corner (MWC). This is rarely observed, and the limit of seismic behaviour is generally associated with the intersection of the subducting plate with the forearc mantle. The termination of seismic behaviour here is believed to be a result of the serpentinization of the forearc mantle (Hyndman and Peacock, 2003). Laboratory experiments show that the serpentine minerals generally exhibit stable-sliding aseismic behaviour (Reinen et al., 1991) and are likely responsible for the transition to aseismic behaviour in cool subduction zones. Outside of the seismogenic zone, a region of conditional stability is observed where seismic rupture is found to propagate but not nucleate. This site is known as the frictional transition zone and is the location of a recently discovered form of intermediary stress release called slow slip events (SSEs).

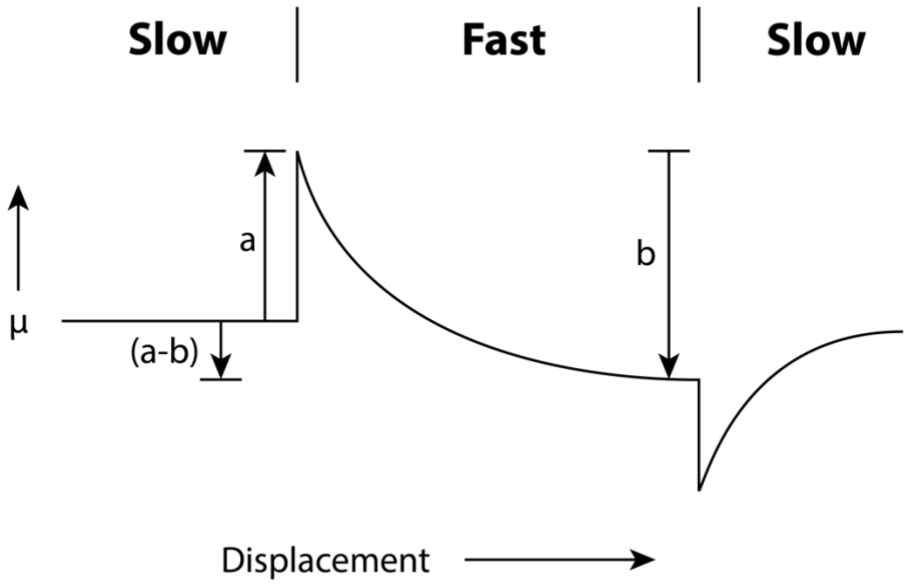

FIGURE 1.3: SCHEMATIC DIAGRAM SHOWING THE EXPERIMENTALLY OBSERVED FRICTIONAL RESPONSE TO AN INCREASE AND THEN DECREASE IN SLIDING VELOCITY. ADAPTED FROM SCHOLZ, 1998.

1.2 THE DISCOVERY OF SLOW SLIP EVENTS

Due to improvements in both Global Navigation Satellite System (GNSS) and seismograph station deployment, the discovery and detection of SSEs has drastically improved our understanding of how accumulated tectonic stress at subduction zones is released. Unlike regular “fast” earthquakes, stress during SSEs is released over a period of days to months rather than seconds to minutes. This is observed as intermediate slip rates between those observed for regular earthquakes, on the order of meters per second, and stable (i.e., continuous) sliding, up to 10 orders of magnitude slower. SSEs are typically observed in the transition zone; thus, the frictional characteristics of this region likely facilitate slow slip occurrence.

Seismologists have noted the existence of a spectrum of elastic deformation events with characteristic durations and different levels of high and low frequency excitation since the mid 20th century (Benioff and Press, 1958; Kanamori, 1972; Kanamori and Stewart, 1979). On one end of the spectrum, “slow” or “silent” earthquakes were described based on their long duration and lack of detectable high frequency radiation (Beroza and Jordan, 1990). Observation of this phenomena includes GNSS-detected anomalous crustal movements. This is characterized by the transient reversal in the direction of crustal motion where the GNSS data shows a temporary signal in the direction opposite of plate movement (Fig. 1.4). Early observations of this behaviour on a continental fault include a week-long event recorded by borehole strainmeters on the San Andreas Fault (Linde et al., 1996). In the case of subduction zones, early observations include a 300-day-long event located in the Bungo Channel in southwest Japan (Hirose et al., 1990) as well as a two-week-long event in Cascadia with an equivalent moment magnitude (M_W) of ~6.7 (Dragert et al., 2001). Following the observation of slow slip, instances of long-period tremor were observed in seismic data, again in southwest Japan (Obara, 2002). Tremor is typically described as a collection of low-frequency earthquakes with periods in the range of 0.2 to 2 s and are often observed at active volcanoes (Chouet, 1996). In this case a characteristic gradual rise time in the seismic envelope, which lacks the typical spike-like signal of a normal earthquake, is observed at multiple stations. By analogy to these “volcanic tremors”, early observations of “non-volcanic tremor” (also called “tectonic

tremor") were originally attributed to the movement of fluid in subduction zones, which are liberated by slab dehydration reactions (Obara, 2002). In later studies of the Cascadia Subduction Zone (CSZ), similar tremor signals were observed, this time being spatially and temporally correlated with Global Positional System (GPS) detected SSEs (Rogers and Dragert, 2003). It was then determined that "silent" earthquake was a misnomer and that in fact slow slip had unique seismic signatures that are different than regular earthquakes.

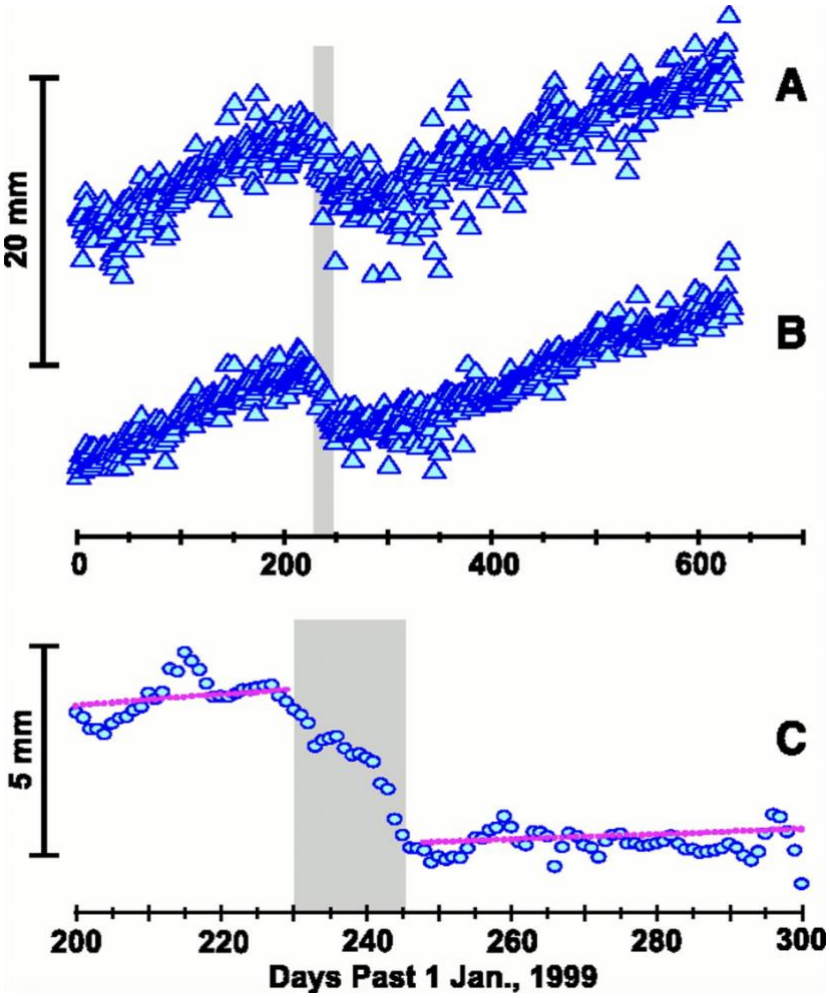

FIGURE 1.4: GNSS DATA OF A SHORT-TERM SLOW SLIP EVENT IN CASCADIA. A REVERSAL IN THE TREND OF PLATE MOVEMENT IS HIGHLIGHTED IN GREY. (A) SHOWS THE RAW TIME SERIES, WHILE (B) SHOWS THE FILTERED TIME SERIES WITH DAILY RESIDUALS REMOVED. (C) SHOWS AN EXPANDED VIEW OF THE REVERSAL WITH THE LINEAR TREND SHOWN BY THE PINK LINE. DRAGERT ET AL. 2001.

1.3 THE GLOBAL OCCURRENCE OF SLOW SLIP EVENTS

A wide variety of these slow slip phenomena is now found at the root of many large plate boundary fault zones (Fig. 1.4), most commonly in the transition zone which is located down dip of the seismogenic zone and up dip of the stable sliding zone (Fig. 1.5) (see reviews in Bürgmann, 2018; Behr and Bürgmann, 2021; Jolivet and Frank, 2020). Typically, SSEs (most often with accompanying tectonic tremor) can be observed as either short-term events, lasting from days to weeks, or long-term events, lasting from months to years. SSEs have not been observed along all subduction zones and are sometimes confined to specific segments along a given subduction zone (Schwartz and Rokosky, 2007).

The Cascadia subduction zone is one of the most reliable sources of SSEs globally (Rogers and Dragert, 2003). It runs along the western edge of North America, from northern California in the south to Vancouver Island in the north and is the site of the subduction of the Gorda, Juan de Fuca Plate, and Explorer plates, from south to north, beneath the North American plate. SSEs and accompanying tectonic tremor, with durations of ~2 weeks (Wech et al., 2009) are observed along the entire subduction margin and are found to occur down dip of the seismogenic zone at the start of the MWC, corresponding with depths of 25-45 km in a region known as the transition zone (Fig. 1.5) (Dragert et al., 2004). The margin is segmented along-strike into three regions of unique SSE behaviour with differences in recurrence time, tremor density, and energy rates (Brudzinski and Allen, 2007; Wech, 2021).

Another subduction zone known for its reliable source of SSEs is the Nankai trough in southwest Japan, where the Philippine Sea Plate is subducting beneath the Eurasian Plate. Short-term SSE's and accompanying tremor are observed along most of the margin with a single gap in occurrence within the Kii Channel (Obara, 2002). These short-term events are found to occur down dip of the seismogenic zone at the start of the MWC and have recurrence times of 3 to 6 months (Ozawa, 2017; Nishimura et al., 2013). In contrast to Cascadia where long-term events have not yet been detected, accompanying long-term events are observed along parts of the margin, just up dip of the site of the short-

term events within the Bungo Channel and western Shikoku (Hirose et al., 1999; Hirose and Obara, 2005).

Along the Middle-American Trench, which is the site of the Cocos Plate subducting beneath the North American Plate along the western coast of Mexico, similar SSE behaviour is observed to that in southwest Japan. Within Oaxaca in the south and Guerrero in the central portion of the margin, short-term and long-term SSEs are observed (Radiguet et al., 2012; Brudzinski et al., 2007; Graham et al., 2015; Correa-Mora et al., 2008). Large long-term events are found to occur every 4 years in Guerrero and every 1-2 years in Oaxaca (Graham et al., 2015). Inter-SSE bursts in tremor activity occur in association with smaller short-term SSEs (Frank et al., 2015; Villafuerte, 2017). The location of these events follows typical patterns with the short-term events occurring near the MWC and long-term events occurring just up dip. In the northern part of the margin, different SSE behaviour occurs as only short-term events are detected, and long-term events are absent (Brudzinski et al., 2016).

A unique case of SSE occurrence is found at the Hikurangi margin along the eastern coast of New Zealand where the Pacific Plate subducts beneath the Australian Plate. Here a diverse range of slow slip behaviour occurs which include shallow (<20 km) offshore short-term events in the north (lasting 1-4 weeks), and deeper long-term events (lasting ~1.5 years) in the south (Wallace and Beavan, 2010; Wallace, 2020). In the north, SSEs are accompanied by spatio-temporally correlated tectonic tremor (Todd et al., 2016). Hikurangi represents an unusual case of SSE occurrence as it is the site of subduction of a relatively old, and therefore cold, plate (>100 Myr). Most other cases of SSEs are found at young and warm subduction zones (e.g., Cascadia, Nankai, Mexico). Current hypotheses suggest that the rough subducting plate in the north, where seamounts protrude above the deposited sediment, create heterogeneous stress distribution that promotes episodic SSEs (Wang and Bilek, 2014).

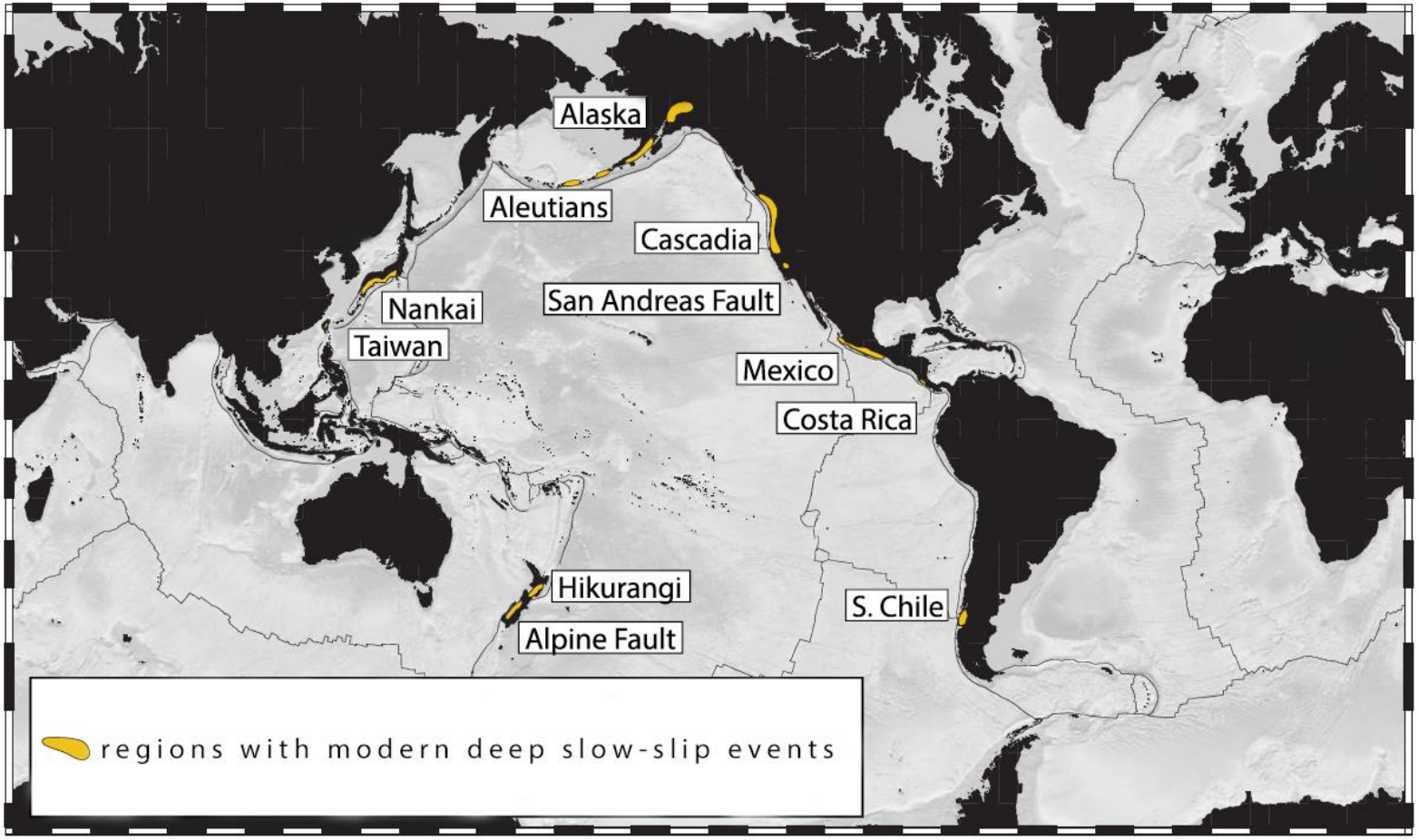

FIGURE 1.5: GLOBAL MAP OF LOCATION OF DETECTED DEEP SSES. ADAPTED FROM BEHR AND BURGMANN, 2021.

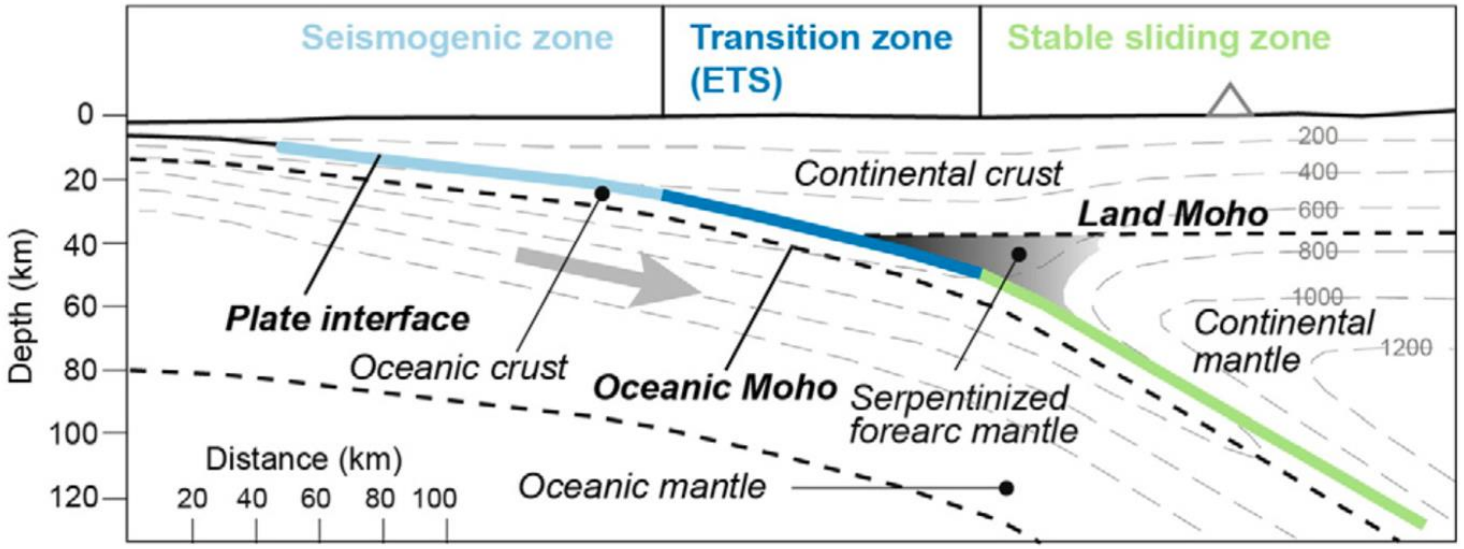

FIGURE 1.6: CONCEPTUAL DIAGRAM OF THE CASCADIA SUBDUCTION ZONE. THE SITE OF SLOW SLIP IS LOCATED IN THE TRANSITION ZONE, NEAR THE LOCATION OF THE MANTLE WEDGE CORNER, WHICH IS LOCATED DOWN DIP OF THE SEISMOGENIC ZONE AND UP DIP OF THE STABLE SLIDING ZONE. AUDET AND KIM, 2016

Other subduction zones with observed SSE include Costa Rica, Alaska, the Aleutians, and southern Chile. SSEs have also been observed at the root of some continental transform faults including the San Andreas Fault in California (Shelly, 2017) and the Alpine Fault in New Zealand (Wech et al., 2012). It is currently unknown whether all large active faults host some type of slow-earthquake behaviour. Current limitation associated with seismic and GNSS station density in some remote areas make detecting slow slip and tremor challenging.

1.4 THE MECHANISM OF SLOW SLIP

In the region where SSEs nucleate, it has been observed that a layer exhibiting low seismic velocities exists with high compressional-to-shear wave velocity ratios (Vp/Vs) (Abers, 2005; Audet et al., 2009) that are consistent with the presence of abundant fluid with near-lithostatic pore fluid pressures. There is still debate on the makeup of the low-velocity layer (LVL) with some arguing it consists of upper oceanic crustal rocks at high fluid pressures (Hansen et al., 2012) and others stating that it is predominately composed of underplated metasedimentary rocks (Abers et al., 2009., Calvert et al., 2011). The exact makeup of the LVL remains unknown, but the presence of elevated pore-fluid pressures which decrease the effective normal stress and thus weaken the frictional strength of the fault, remains a consistent feature of all hypotheses relating to mechanism behind slow slip.

In the case of the CSZ, the location of SSEs correlates well with the MWC. It has been suggested that relationship between SSEs and the MWC is a result of the serpentinization of the mantle forearc. Here, the serpentinized forearc mantle acts as an impermeable surface that channels fluids, which are released via prograde metamorphic dehydration reactions, to the site of SSEs (Hyndman, 2015). According to Audet and Burgmann, (2014), low Vp/Vs ratios in the lower continental crust, above where tremor is observed, are consistent with silica enrichment from slab-derived fluids and mineralization in quartz veins. Here the cyclic nature of SSE is related to changes in pore-fluid pressures because of the breaching and resealing of the plate interface shear zone via mineral precipitation processes. Gosselin et al., (2020) observed changes in the seismic velocity associated with the LVL following SSEs, which is consistent with the temporary reduction in pore-fluid pressure following slow slip. Similar observations have been made in Japan where temporal changes in seismic attenuation associated with slow slip have been observed, also suggesting episodic fluid drainage along the plate interface (Nakajima and Uchida, 2018). In New Zealand, time-dependent changes in the stress state of the oceanic crust are interpreted as being a result of the rise and drop of fluid pressures before and after SSEs (Warren-Smith et al. 2019). Based on these findings, the fault-valve hypothesis for SSE occurrence states that the diverse timescales and recurrence intervals of slow slip

are due to variations in the rate of processes that generate and trap fluids. These processes include the generation of fluids via metamorphic dehydration reactions, the transportation of fluids to the site of slow slip, vein closure via mineral precipitation, and permeability changes due to shearing.

There is some uncertainty in the role of fluid mobilization in generating the elevated pore-fluid pressures necessary for slow slip. For example, Condit et al. (2020) find that in the case of warm subduction zones, dehydration of Mid-Ocean Ridge Basalts (MORB) produce aqueous fluids at the depths of SSEs and up-dip migration of fluids along the slab is not necessary. In this case the location of slow slip depends on the local P-T conditions that trigger mineralogical changes that release H_2O, specifically in this case, the breakdown of chlorite and lawsonite. Other studies note the remarkable correspondence between SSE location and the MWC, specifically in the case of Cascadia (Hyndman, 2015). When fluid mobilization is considered, fluid flux rates may be 5 to 10 times that of in situ dehydration although there is much uncertainty in these values. Another factor to consider in this case, is the increase in silica source as silica solubility will be larger for fluids generated at higher temperatures (Hyndman et al., 2015). It has also been found that the process of fluid release and channelling results in high fluid volumes in shorter time intervals (<1 year) which better reflect the time scale of SSEs (Taetz et al., 2018). Overall, the role of fluid mobilization has important implications for where we observe slow slip as well as the main mechanism behind it. Differentiating between in-situ and mobilized fluid production requires accurate P-T models with complementary geochemistry data which is currently limited.

Other suggested mechanisms for controlling slow slip behaviour include effects of fault dilatancy where the strength of dilatancy can influence modeled SSE behaviour (Segall et al., 2010; Liu and Rubin, 2010; Liu, 2013). In the case of fluid saturated material, dilatancy can decrease the pore fluid pressure by creating void space, which can in turn increase the effective normal stress, strengthening the fault. Increasing the strength of dilatancy is found to lower slip velocities, lead to longer recurrence intervals, and increase slip amounts. Effects of slab geometry on SSE behaviour have also been established, where numerical modeling using rate- and state-dependent friction law show that

segmentation of slow slip in Cascadia is inversely related to the fault dip and strike angles of the slow slip zone (Li and Liu, 2016). This implies that slab geometry may have significant control on the slow slip process. Brudzinski and Allen (2007) note the correlation between the overlying accreted oceanic terranes in Cascadia and slow slip recurrence intervals. In this case, the denser and stronger Siletzia terrane of the overlying continental lithosphere in central Cascadia can accommodate more stress leading to longer recurrence intervals in this region. Which mechanism contributes most to controlling slow slip behaviour is an ongoing topic of study. Expanding the scope of many of these studies to different subduction zones will further establish whether these mechanisms explain the global variation of slow slip behaviour.

1.5 OVERVIEW

The discovery of slow slip as an intermediary form of stress accommodation in subduction zones has been one of the most exciting seismological discoveries in recent decades. The role that slow slip plays in the earthquake cycle has many implications including its potential role in accommodating significant amounts of stress leading to widespread aseismicity (e.g. Cascadia). Stress release via seismic activity is known to account for a small fraction of total plate motion so further quantification of slow slip events will improve estimates of the total seismic moment budget. Additionally, SSEs have also been reported to trigger increases in seismicity within plate segments (Lowry, et al., 2001; Ozawa et al., 2003) by altering the stress field and reducing the frictional stability of the fault interface. Our current understanding of the relationship between SSEs and megathrust earthquakes is limited, but the potential ability for SSEs to influence their nucleation makes understanding these processes critical (Obara and Kato, 2016). This work provides key elements in improving our understanding of fault processes at subduction zones, which is critical in the risk assessment of natural hazards in some of the most populated regions on earth. With increased knowledge in this field, we can mitigate the effects of earthquake hazard through improving engineering standards as well as emergency protocol in high-risk regions.

Based on these premises, my thesis is focused on providing insight into the following questions: Why does fault slip behaviour vary across global subduction zones? Can slow slip behaviour be explained by a single process, e.g., slab dehydration, or are there various mechanisms by which the mechanical strength of the slab is altered that can produce these events? What role does the down-going versus overriding plate have in creating the necessary conditions for slow slip nucleation? These questions are addressed in each of the following three separate chapters:

Chapter I

In Chapter I, I address the first question by exploring the range of controlling parameters of subduction zones to a global setting through multivariate analysis of global geophysical data. Only a few review articles provide an overview of SSE

behaviour globally with the vast majority focusing on individual subduction zones and investigating single controlling factors in generating SSEs. For example, SSEs are thought to occur preferentially in warm (i.e., young) subduction zones; this factor may not be universal or sufficient by itself to generate SSEs, and other factors have been proposed. However, most studies use a small number of data summaries (e.g., age of subducting plate), which has the unintended consequence of discarding other potential factors and therefore limiting the applicability of physical models to particular cases. First, we wish to understand which factors (and combinations thereof) are most important in generating SSEs. In machine learning parlance, this problem falls in the category of Supervised Classification problems, where multivariate data and SSE observations are used to train a mathematical model to learn whether a subduction zone segment hosts SSEs or not for regions that are well instrumented.

This chapter also addresses the third question by focusing on physical characteristics of the down-going plate including subducting plate age, relative velocity, sediment thickness, seafloor roughness, and plate dip. The ability for a trained model to accurately predict where SSEs occur provides evidence for the predictive power of the physical characteristics of the down-going plate. In addition, parametric models can quantify the relationship between a feature and the outcome through correlation coefficients. This creates two ways to interpret the potential influence of the down-going plate on SSE generation, with the first considering the combination of features and the second considering individual feature effects.

Chapter II

In Chapter II, I primarily address the second question by testing the hypothesis that metamorphic dehydration reactions and the fluids they produce are a driving mechanism for generating the conditions for slow slip. In addition, I test whether different patterns in slab dehydration can control different slow slip behaviour, including recurrence times, energy rates, and tremor density. Our current understanding of the mechanisms behind slow slip suggests that elevated pore-

fluid pressures are necessary along the interface where slow slip is observed. This has the effect of reducing the effective normal stress and therefore the frictional strength allowing for semi-frictional behaviour where stable sliding would be expected (Gao and Wang, 2017). To test this hypothesis, I construct temperature and pressure models along the entirety of a single subduction zone to estimate slab dehydration rates and compare them to the location of observed slow slip events. The CSZ provides reliable slow slip occurrence with events being observed along the entirety of margin occurring every 10-19 months (Brudzinski and Allen, 2007). In addition to the second question, this chapter addresses the first question by determining how varying subducting parameters affect the pattern of slab dehydration and how they may limit generation of slow slip. For example, must a subduction zone be hot to expel water at the correct depths? This further addresses the third question by modelling a potential mechanism for slow slip which is mainly driven by factors controlled by the subducting slab.

Chapter III

In Chapter III, to address the third question, I characterize the anisotropic structure of the mantle wedge corner (MWC) in northern Cascadia to provide further insights into the role that this area may play in the generation of slow slip. The MWC in Cascadia is thought to be widely serpentinized which produces a highly foliated fabric that may play an important role in the channelling of fluid near the site of slow slip occurrence. I use teleseismic scattering data (known as receiver functions) to determine the structure of the overriding plate including the MWC. This produces estimates of the changing 1D isotropic velocity structure, which can be used to infer layering in the sampled subsurface, as well as the anisotropic structure, which can be interpreted as being a result of the preferential alignment of material through foliation in the case of a highly foliated rock such as serpentinite. This chapter provides constraints on the potential role the overriding plate has in creating an impermeable layer near the site of SSEs which may be necessary to weaken the fault through trapping fluids and generating fluid overpressures.

PART II: THESIS CHAPTERS

2

UNCOVERING THE PHYSICAL CONTROLS OF SLOW SLIP USING SUPERVISED CLASSIFICATION

ABSTRACT

Deep slow slip events (SSEs) at subduction zones have significantly contributed to refining our understanding of the megathrust earthquake cycle at the brittle-ductile transition. However, the specific combination of factors that determine their occurrence has not yet been fully explored. Here we evaluate the contribution of several of these characteristics using globally mapped geophysical data that are used as proxies for physical properties of the subducting plate. This is performed by classifying 25 km-wide, trench-parallel segments into binary classes based on the observation (or lack thereof) of deep, short- or long-term SSEs. The five characteristics explored here include subducting plate age, sediment thickness, relative plate velocity, slab dip, and plate surface roughness. We use these characteristics to train six Machine Learning models based on different learning algorithms: Gaussian Naïve Bayes, Logistic Regression, Linear Discriminant Analysis, Random Forest, Support Vector Machine, and K-Nearest Neighbour. Short-term SSE models show that subducting plate age, relative velocity, and sediment thickness have the strongest predictive power with the first two characteristics negatively correlating and sediment thickness positively correlating with SSE occurrence, respectively. These results are consistent with a conceptual model where slow slip is controlled by conditions favoring the enduring release (and possible storage) of fluids near the source region. However, the relationship between these features and elevated pore fluid pressures is not established here and further evidence is needed to validate this hypothesis. We then use a final model constructed as a weighted average of the best performing models to make predictions on the probability of SSE occurrence, with predicted short-term SSE occurrence in South America, the Aleutians, Sumatra, Vanuatu and Solomon, as well as long-term SSE occurrence in the Aleutians, Izu-Bonin, Kuril-Kamchatka, Mariana, and Tonga-Kermadec. Overall, long-term SSE models do not perform as well as the short-term SSE models which may indicate that long-term SSEs are controlled by a different and/or extended set of physical characteristics than the short-term SSEs.

2.1 INTRODUCTION

The discovery of slow slip events (SSEs) from GPS monitoring has drastically altered our understanding of how accumulated tectonic stress at subduction zones is released (Obara and Kato, 2016). Unlike regular “fast” earthquakes, stress during SSEs is released over a period of days to months and is often associated with tectonic tremor (Rogers and Dragert, 2003). This is observed as intermediate slip rates between those observed for regular earthquakes, on the order of meters per second, and stable sliding, up to 10 orders of magnitude slower (Schwartz et al., 2007). When the geodetic and seismic signals are correlated spatially and temporally, this is referred to as a single event of episodic tremor and slip, or ETS (Rogers and Dragert, 2003). SSEs have not been observed along all subduction zones and are sometimes confined to specific segments along a given subduction zone. The segmentation of SSEs is further complicated by its complex and variable behaviour. SSEs have been observed with and without tectonic tremor, up- and down dip of the seismogenic zone, and with varying time scales including short-term SSEs (with durations of days to a few weeks) and long-term SSEs (with durations of months to years). Currently, subduction zones with observed episodic slow slip include: Cascadia (Dragert et al., 2001; Miller et al., 2002; Dragert et al., 2004; Schmidt and Gao, 2010; Melbourne et al. 2005), Nankai (Hirose et al., 1999; Hirose and Obara, 2005; Sekine et al., 2010), Mexico (Kostoglodov et al., 2003; Maury, 2018; Burdzinski, 2016), Costa Rica (Voss et al., 2017; Jiang et al. 2017; Walter et al., 2013), Hikurangi (Wallace and Beavan, 2006; Beavan et al., 2007; Wallace et al. 2012; Wallace and Eberhart-Phillips, 2013; Todd and Schwartz, 2016), and Alaska (Wei et al., 2012; Ohta et al., 2006; Fu and Freymueller, 2013).

Despite two decades of research into slow slip events, there is still no consensus on the range and combination of physical properties that are both necessary and sufficient to explain their occurrence, with only a few review articles that provide an overview of deep slow slip behaviour globally (e.g., Schwartz and Rokosky, 2007; Beroza and Ide, 2011; Wang and Bilek,, 2014; Audet and Kim, 2016; Bürgmann, 2018). The vast majority of studies focus on individual subduction zones and investigate single controlling factors in generating slow slip events, which has the unintended consequence of discarding other

potential factors. Furthermore, there is a lack of global studies of subduction zone slow earthquakes that quantitatively investigate the possible combination of controlling factors. For example, SSEs are thought to occur preferentially in warm (i.e. young) subduction zones (Beroza and Ide, 2011); this factor may not be universal, or sufficient, by itself to generate SSEs, and other factors have been proposed (Yabe, 2014; Wang and Bilek, 2014). Most studies use a small number of data summaries (e.g., age of subducting plate) which has the consequence of discarding other potential factors. Here we attempt to expand these concepts to a global setting through multivariate analysis of globally mapped geophysical data that provide proxies for possible controlling factors. This includes physical, kinematic, and geometric properties of the incoming plate and overriding plate of subduction zones. By doing so we can remove data biases associated with specific subduction zones and uncover universally applicable models. These models can then be used to predict SSE behaviour in poorly monitored areas.

2.2 DATA AND METHODS

2.2.1 FEATURE SELECTION

Subduction zones globally show significant variability as well as along-strike heterogeneity in a large range of physical properties of both the incoming and overriding plates. However, evaluating all possible factors that might contribute to the occurrence of SSEs is prohibitive and likely to yield limited insight. In addition, several factors that are assumed to influence slow fault slip (e.g., high fluid pressure) are difficult to map and compare globally. In our approach, we use proxies for a handful of physical properties using globally mapped geophysical data. We avoid the use of seismic velocity models, as global models do not have sufficient resolution at the spatial scales analyzed here, and high-resolution models are not available everywhere and are highly dependent on the methodology and experimental/field conditions. Furthermore, to develop a predictive model of slow slip behavior, one must first select the physical characteristics that are hypothesized to explain the variability in occurrence, and thus, have a mechanism that relates their contribution to the nature of fault slip.

One of the most widely accepted mechanisms requires near-lithostatic pore-fluid pressures to exist where slow slip occurs (Audet et al., 2009; Kato et al., 2010). This fluid overpressure decreases the effective normal stress, weakening the plate interface and promoting slow slip. At shallow depths, water is introduced through the compaction of subducted sediments that stores free water in its pore space. The presence of abundant sediments near the trench may therefore provide a proxy for fluid availability at depth (Yabe, 2014; Wallace et al., 2017). At greater depths, fluids are further generated through various metamorphic reactions involving the dehydration of hydrous minerals as the subducting oceanic crust is subject to higher temperatures and pressures with increasing depth (Hyndman and Peacock, 2003; Peacock et al., 2011). These dehydration reactions occur in high-temperature environments (Peacock, 1990), which is dominantly influenced by subducting plate age, with younger plates being hotter. Therefore, subducting plate age may control the spatial and depth occurrence of fluid overpressure, and therefore slow slip occurrence (Ide, 2012). This is indeed observed, as the majority (excluding Hikurangi) of slow slip events occur in regions of young (<30 Ma) subducting oceanic lithosphere. If there is a given temperature and pressure window that favours the nucleation of slow slip events, we can assume that the physical parameters that influence the time spent within these conditions can increase the probability of their occurrence. Two physical parameters that limit the time spent in specific temperature and pressure conditions include plate relative velocity and subducting plate dip, which have been previously thought to influence slow slip behavior (Brudzinski et al., 2016; Yabe, 2014). Furthermore, to promote the pore-fluid pressures necessary to weaken the plate interface, certain characteristics may be necessary to allow trapped fluids to escape more readily. One such characteristic includes plate surface roughness, where rougher plates are observed to promote the movement of fluids (Wang and Bilek, 2014).

For the remainder of this paper, we refer to scalar summaries of geophysical data that are used as proxy for physical characteristics as “features”, to be consistent with the nomenclature used in machine learning approaches that we adopt here (see section 2.4). Based on the above conceptual model of slow slip, we select a set of five features that includes: 1) subducting plate age, 2) sediment thickness at the trench, 3) relative velocity, 4) subducting plate dip, and 5) plate surface roughness. Note that we ignore features that

are solely associated with the overriding plate, which are much more complicated due to the (variably) long geological history of the convergent margins.

2.2.2 FEATURE DATA COLLECTION

We define 25 km-wide, non-overlapping, trench parallel segments for global subduction zones based on the trench models of Bassett and Watts (2017). Each segment is characterized by an array of scalar values representing each feature of interest (Fig. 2.1). We collect global spatial data for oceanic crustal age, ocean floor sediment thickness, subducting slab dip, relative plate velocity, and free air gravity anomalies. Oceanic crustal age data (Mueller et al., 2008) and ocean floor sediment thickness data (Mueller et al., 2008) are extracted from the National Oceanic and Atmospheric Administration (NOAA) with 2-minute and 5-minute resolution, respectively. The grid data are sampled within the 25 km-wide and 200 km-long segments, where each segment is centered on the trench position with a long axis orthogonal to the trench. The sampled values are averaged to provide a scalar value for age and sediment thickness for each segment. Free-air gravity anomaly data (Bonvalot et al., 2012) are extracted from the International Gravimetric Bureau with 2-minute resolution. Following the procedure described above, the grid data are sampled for each segment and the standard deviation of the sampled data is assigned as an estimate for surface roughness. We use gravity data rather than bathymetry to define roughness in order to avoid a possible negative correlation between seafloor relief and sediment thickness. Relative velocities between subducting and over-riding plates are calculated from the UNAVCO online plate motion calculator at the midpoint of each segment using the HS3-NUVEL1A model (Gripp and Gordon, 2002). Subducting plate dip values are extracted 100 km landward of the midpoint of each segment from dip contours defined by the Slab2.0 model (Hayes et al., 2018).

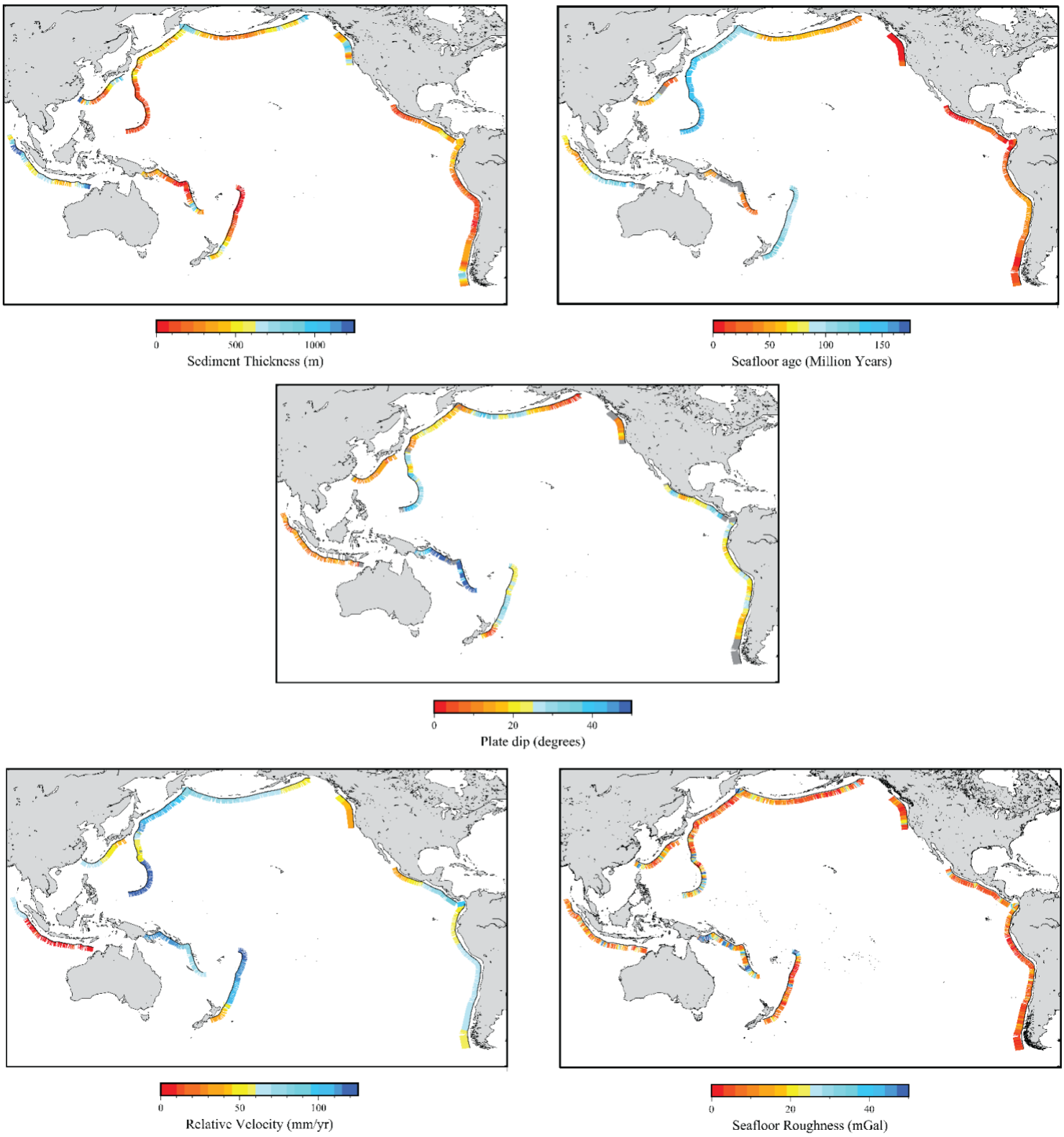

FIGURE 2.1: GLOBAL MAPS DISPLAYING THE MAGNITUDE OF THE SCALAR VALUE ASSIGNED TO EACH SEGMENT FOR EACH FEATURE USED IN THE ANALYSIS. (A) SEDIMENT THICKNESS (MUELLER ET AL., 2008), (B) SEAFLOOR AGE (MUELLER ET AL., 2008), (C) PLATE DIP (HAYES ET AL., 2018

2.2.3 SEGMENT CLASS ASSIGNMENT

In our approach, we seek to provide a first-order discrimination of the features responsible for the occurrence of SSEs through binary classification. Although a more sophisticated study could use regression analysis to investigate the features contributing to particular SSE variables in more detail (e.g., moment rate, slip area, hypocentral depth, etc.), our preliminary work suggests that the small size of the feature data set is a limiting factor in these types of analysis. Each segment is therefore assigned a binary class label based on the observation (label “Yes”), or lack thereof (label “No”), of SSEs. We further assemble two datasets, based on the occurrence of either short-term or long-term SSEs. In the literature, short-term events are typically described as those with a total duration on a scale of days to weeks and long-term events are those lasting from months to years (Obara and Kato, 2016). We use 1 month (30 days) as the cut-off limit for each event classification. We exclude shallow events (i.e., those that occur at depths of <20 km) in the classification due to the difficult nature of their detection. Due to variable levels of instrumentation in different regions, special consideration is given to regions that are insufficiently monitored and poorly studied. We do not include these segments in the development of the machine learning models and they are left as unknowns. GNSS station density is shown in Fig. S2.1 of the supplementary material which can aid in the determining of the detection threshold for a given subduction zone (i.e. segments with no observed SSEs but with similar station density as segments that do host SSEs can be more confidently assigned to the “No” class. SSE occurrence is defined based on measured slip contours for individual slow slip events as well as cumulative slip contours over a given period of time depending on data availability. We use tremor as a proxy for short-term slow slip in regions where small SSEs are suspected but are difficult to detect via GPS due to high levels of noise. Fig. 2.2 shows the along-strike class label of segments along subduction zones with known slow slip behaviour based on spatial constraints of SSEs from previously identified events.

2.2.3.1 ALASKA

Along the Alaskan Trench, deep long-term slow slip events have been observed within the region (Wei et al., 2012; Fu and Freymueller, 2013) with two main slip patches located

in the lower Cook Inlet and upper Cook Inlet. Since no short-term events or tectonic tremor have been observed within the lower Cook Inlet, we assign segments within this region to the “Yes” class for the long-term dataset and to the “No” class for the short-term dataset. Further east, abundant tectonic tremor is observed within the Upper Cook Inlet (Wech, 2016). The along-strike spatial extent of tremor is well constrained as station coverage is sufficient for detection beyond these boundaries. Evidence of short-term events in the region have also been observed as abnormal displacements (Freymueller and Ohta, 2007; Ohta et al., 2006). Due to the observation of both short-term and long-term events, we assign segments along this region to the “Yes” class for both dataset

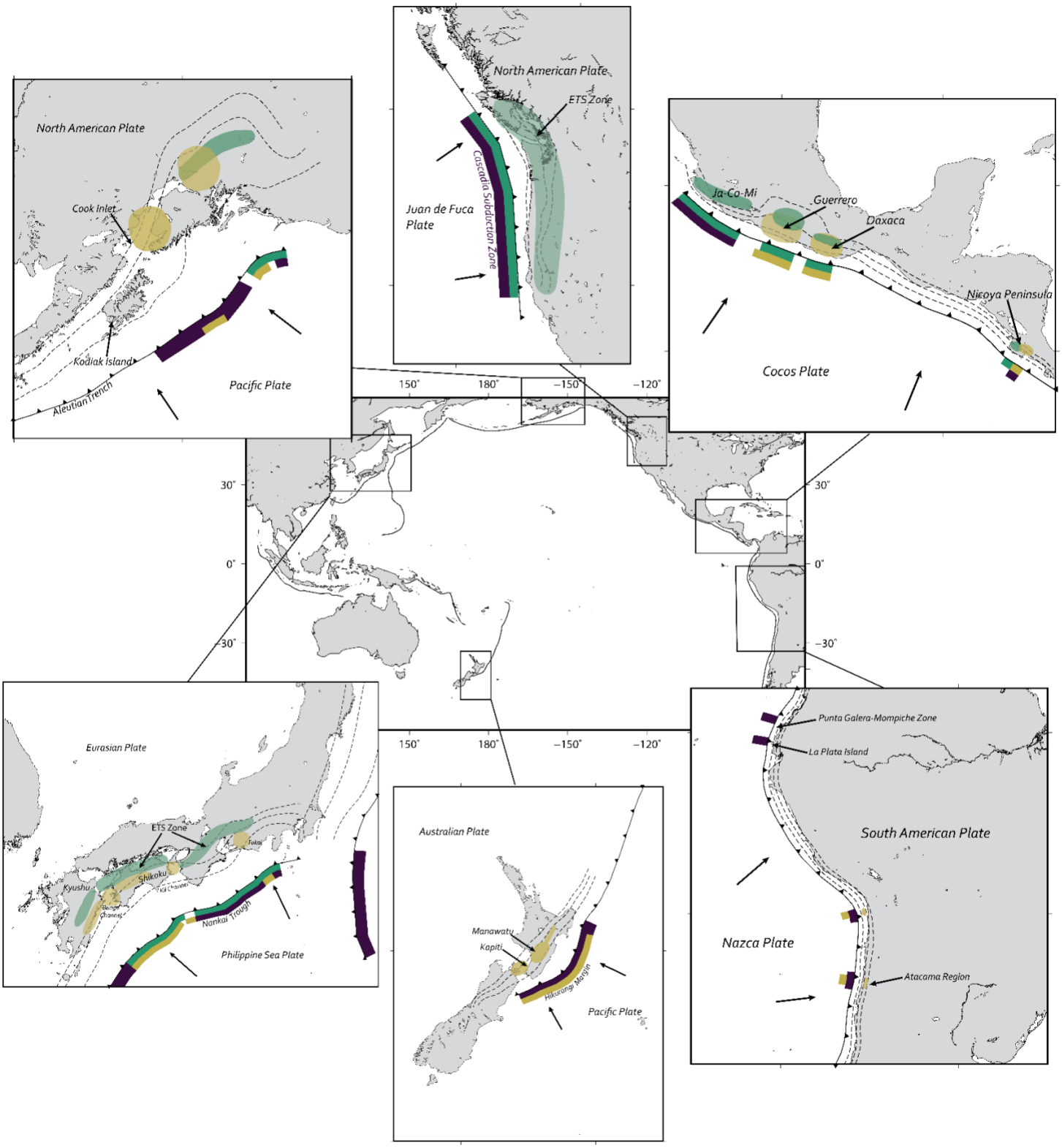
North American Plate
Cook Inlet
Kodiak Island
Aleutian Trench
Pacific Plate
North American Plate
ETS Zone
Cascadia Subduction Zone
Juan de Fuca Plate
Ja-Co-Mi
Guerrero
Oaxaca
Nicoya Peninsula
Cocos Plate
150°
180°
−150°
−120°
30°
0°
−30°
Eurasian Plate
ETS Zone
Tokai
Shikoku
Kyushu
Kii Channel
Bungo Channel
Nankai Trough
Philippine Sea Plate
Australian Plate
Manawatu
Kapiti
Hikurangi Margin
Pacific Plate
Punta Galera-Mompiche Zone
La Plata Island
South American Plate
Nazca Plate
Atacama Region

FIGURE 2.2: OVERVIEW OF GLOBAL SLOW SLIP BEHAVIOUR AND CORRESPONDING SEGMENT CLASSIFICATION. SPATIAL CONSTRAINTS OF SHORT-TERM AND LONG-TERM SSES ARE SHOWN BY GREEN AND YELLOW SHAPES. SEGMENT CLASSES ARE REPRESENTED BY COLOURED AREAS OCEANWARD OF THE TRENCH. THE AREA IN CONTACT WITH THE TRENCH REPRESENTS CLASSIFICATION OF SHORT-TERM EVENTS, WHERE GREEN PORTIONS REPRESENT SEGMENTS WITH OBSERVED SHORT-TERM SLOW SLIP AND THE PURPLE PORTIONS REPRESENT SEGMENTS LACKING SHORT-TERM SLOW SLIP OBSERVATIONS. LONG-TERM SEGMENT CLASSIFICATIONS FOLLOW ALONGSIDE THE SHORT-TERM EVENTS WITH THE YELLOW PORTION REPRESENTING SEGMENTS WITH OBSERVED LONG-TERM SLOW SLIP EVENTS AND THE PURPLE PORTION SEGMENTS LACKING LONG-TERM EVENT OBSERVATIONS. DATA SOURCES: CASCADIA (SSE: BEROZA AND IDE, 2011); MEXICO (SSE: GRAHAM ET AL. 2015; ROUSSET ET AL. 2017; MAURY ET AL. 2018; VILLAFUERTE, 2017); COSTA RICA (SSE: VOSS ET AL. 2017); ECUADOR (SSE: VACA ET AL. 2018); CHILE (SSE: RUIZ ET AL. 2014); HIKURANGI (SSE: WALLACE AND EBERHART-PHILLIPS, 2013); JAPAN (SSE: KOBAYASHI, 2017; TANAKA ET AL. 2018, NISHIMURA, 2013); ALASKA (SSE: FU AND FREYMUELLER, 2013; WEI ET AL. 2012)

2.2.3.2 MEXICO

Along the Middle-American Trench, a wide array of slow slip behaviour has been observed. Within Mexico, three main regions, Guerrero (Radiguet et al., 2012), Oaxaca (Brudzinski, et al., 2007; Graham et al., 2015; Correa-Mora et al., 2008), and the Jalisco-Colima-Michoacan (Ja-Co-Mi) region (Brudzinski et al., 2016) are defined by their varying slip behaviour. Within Guerrero, large long-term SSEs are found to occur every ~4 years. Within Oaxaca, long-term SSEs are also observed, repeating every 1-2 years and lasting ~6 month (Graham et al., 2015). Tectonic tremor is spatially separated from the SSEs and are found to occur down dip of the main slip patch (Kostoglodov et al., 2010; Husker et al., 2012). Inter-SSE bursts in tremor activity are associated with small short-term SSEs that occur down dip of the long-term slow slip patches (Frank et al., 2015; Villafuerte, 2017). Similar observations of short-term SSEs have been made in Oaxaca (Husker et al., 2019) and Ja-Co-Mi (Brudzinski et al., 2016). Due to high observational noise, these events are difficult to detect using traditional methods. Sparse event detection limits our ability to spatially constrain the slip patches using GPS measurements; instead we use tectonic tremor activity to define the spatial constraints of short-term SSEs in the region. Based on the observations above we assign segments in the Ja-Co-Mi region to the “Yes” class for the short-term data set and to the “No” class for the long-term dataset, whereas the segments in Guerrero and Oaxaca are labelled “Yes” in both cases.

2.2.3.3 COSTA RICA

Beneath the Nicoya Peninsula in Costa Rica, both shallow and deep SSEs have been observed (Outerbridge et al., 2010; Voss et al., 2017) with associated tectonic tremor (Outerbridge et al., 2010). The recurrence of these SSEs show variability in both the depth of the slip patch and the slip area, with events lasting from ~1.5 to ~7 months. The observation of tectonic tremor is evidence of likely short-term SSEs so we assign these segments to the “Yes” class for both datasets.

2.2.3.4 NEW ZEALAND

The Hikurangi Trench, located off the eastern coast of the North Island of New Zealand, displays significant along-strike and dip variation in slow slip behaviour. Within the southern portion of the island, long-term SSEs (lasting ~1.5 years) are observed in

the Kapiti and Manawatu regions at depths of 25-60 km (Wallace and Beavan, 2010). In contrast, further north we observe shallow (<20 km), offshore, short-term SSEs lasting approximate 1-4 weeks (Wallace and Beavan, 2010). Further inland, at the central Hikurangi margin, moderate length SSEs lasting 2-3 months at depth of 25-50 km are observed. SSEs along the northern Hikurangi Margin are generally accompanied by detectable spatio-temporally correlated tectonic tremor (Todd et al., 2016). In addition, tremor is also found to occur further inland in bursts lasting 2-3 months. The origin of these events is unknown but currently believed to be associated with undetected long-term SSEs that are below the geodetic detection threshold (Todd et al., 2016). Based on these observations, we assign segments in the central to southern portion of the trench to the “Yes” class in the long-term case and to the “No” class in the short-term case. Segments located in the north are assigned to the “No” class for both datasets.

2.2.3.5 JAPAN

Southwestern Japan hosts diverse slow slip behaviour along the entire extent of the Nankai Trough. ETS events with a recurrence interval of 3 to 6 months occur down dip of the seismogenic zone within Kyushu (Ozawa, 2017), Shikoku (Takagi et al., 2016), Kii and Tokai (Nishimura et al., 2013). Up dip of the ETS events, long-term SSEs have been observed within the Bungo Channel and western Shikoku (Hirose et al., 1999; Hirose and Obara, 2005), in the Tokai region (Ozawa et al., 2002; Suito and Ozawa, 2009; Ozawa et al., 2016), and the Kii Channel (Kobayashi, 2014; Kobayashi, 2017). We assign segments in the southern portion of Kyushu to the “No” class, and the majority of segments in western Shikoku to the “Yes” class for both datasets. Within the Kii Channel a gap in short-term SSEs is observed so we assign “Yes” for the long-term data set only. Further east, segments are found only to host short-term events so we assign “Yes” for the short-term data set until eastern Tokai where we see a return of long-term events.

2.2.3.6 SOUTH AMERICA

South America presents a unique case in which there have been only sparse observations of slow slip behaviour along its ~4000 km extent. The lack of observed SSEs may have implications on the conditions that favour slow slip nucleation but may also be an artifact of poor GPS station coverage. Currently, few regions along the South

American trench have been found to host SSEs, the first of which is located in the North Chile seismic gap (Socquet et al., 2017; Ruiz et al., 2014). Here, an 8-month long event occurred offshore, preceding the 2014 M_w 8.1 North Chile megathrust (Socquet et al., 2017). From the lack of observable tectonic tremor and deep, short-term events, combined with evidence of sufficient GPS station coverage to identify SSEs, we assign the segments including the North Chilean long-term SSEs to the “No” class for both datasets. The second region in which SSEs have been observed is within the Punta Galera Mompiche Zone (PGMZ) in northern Ecuador. In late 2012 to early 2013, a 2-month long, shallow (5-25 km depth) SSE was observed and correlated with seismic swarms. Seismic data shows the recurrence of these seismic swarms with a periodicity of ~2 years (Vaca et al., 2017). Further south in central Ecuador, located beneath La Plata Island, a shallow, short-term SSE event was found to occur (Vallee et al., 2013). Like the PGMZ events in the north, this event was associated with increased seismic activity in the slip region.

2.2.3.7 CASCADIA

The Cascadia Subduction zone in western North America extends from northern California in the south to northern Vancouver Island in the north. It is unique in that widespread ETS has been observed across its entire length. SSEs in Cascadia were first discovered in the early 2000’s (Dragert et al., 2001) where GPS reversals were observed for approximately 2 weeks (Wech et al., 2009). Since then, widespread SSEs have been observed along the Cascadia subduction zone (Miller et al., 2002; Dragert et al., 2004; Schmidt and Gao, 2010; Melbourne et al., 2005) where they are both spatially and temporally correlated with tectonic tremor. These events have a regular periodicity of 10, 14, and 19 months (Brudzinski and Allen, 2007), with slip being measured to occur on the deep portion of the plate interface at depths of 25-45 km (Dragert et al., 2004). We assign the label “Yes” for the entire extent of the Cascadia Subduction Zone for the short-term data set; however, no long-term SSEs have yet been reported despite adequate observational infrastructure.

2.2.3.8 SUMATRA

The Sumatra-Andaman subduction zone is one of the most seismically active regions in the world. The widespread occurrence of abundant seismicity makes it difficult to identify SSEs through traditional methods due to the saturation of GPS time series with regular (seismic) fault motion. A systemic search for SSEs was conducted by Feng et al., (2015) to determine if the Sumatran GPS array had detected any SSEs since its installation in 2002. Feng et al., conclude that there is no evidence for SSEs at the scale of slow slip that is most commonly observed. Based on the determined resolution, it is concluded that Cascadia-type events are unlikely to occur in the region studied. Based on these observations, we assign segments located within central Sumatra to the “No” class for our short-term data set.

2.2.4 MACHINE LEARNING APPROACH

Machine learning (ML) is a computer science approach to uncovering complex patterns within data that are not obvious based on human observation. It is rapidly becoming a popular tool for data analytics in the geosciences due to the complex and interactive nature of the earth system (Bergen et al., 2019). The advantage of machine learning over other data processing approaches is the ability to learn from data without being explicitly programmed. Due to the capacity of modern computers to process large amounts of data, the opportunity exists to reveal new information from various types of data. Previous ML applications in solid earth geophysics and seismology include (though not limited to): earthquake detection (Wang & Teng, 1995); earthquake location (Dai & Macbeth, 1997; Gentili and Michelini, 2006; Reynen and Audet, 2017); earthquake classification (Mousavi, et al., 2016; Reynen and Audet, 2017); earthquake prediction (Panakkat and Adeli, 2009); fault slip inversion (Kaufl et al., 2016); predicting mantle dynamics (Shahnas, et al., 2018); and lithological mapping (Kuhn et al., 2018).

Our approach here is to use supervised classification algorithms to determine which subduction zone characteristics have predictive power in determining the occurrence of SSEs. In ML nomenclature, the inputs to ML models are called “features”, as mentioned above. Supervised training algorithms use data with known classes to determine which combination of features is most successful in producing a correct output. There are

various supervised classification algorithms that can be applied, each making unique assumptions about the distribution of the input data and following different strategies to classify the data with some being better suited for our purposes than others. We separate these algorithms based on whether they are linear or non-linear separators. Linear classifiers have the advantage of interpretability due to creating a linear equation with coefficients that can provide information on the contribution of each feature to a correct output. In contrast, non-linear classifiers generally produce better predictions on unknown datasets since it is often the case that the two classes are not linearly separable. We explore various linear and non-linear classifiers in the following sections.

2.2.4.1 LINEAR CLASSIFIERS

Logistic Regression

Logistic Regression (LR) (Cox, 1958) uses the logistic function

$$\frac{e^x}{(1+e^x)}, \qquad \textit{Eq. 2.1}$$

to estimate the probability of a binary event with the output of the model being either 0 or 1. This is done by putting a linear equation with the feature data and parameters into the logistic function as follows:

$$P(y=1) = \frac{1}{1+e^{(-(\beta_0+\beta_1 x_1+\cdots+\beta_n x_n))}}. \qquad \textit{Eq. 2.2}$$

The output of logistic regression is a probability between 0 and 1, therefore we set up the log odds and set it equal to the linear equation:

$$log\left(\frac{P(y=1)}{P(y=0)}\right) = \beta_0 + \beta_1 x_1 + \cdots + \beta_n x_n. \qquad \textit{Eq. 2.3}$$

The coefficients of the linear combination are determined through Maximum-likelihood estimation (MLE) (Fisher, 1912). MLE determines model parameters by finding the ones that maximize the likelihood function. In other words, the best parameters are selected by minimizing the error between the probability of the predicted class and the actual class

observed in the data (e.g. 1 or 0 in the binary case). Logistic regression makes few assumptions about the input data making it widely applicable. The tendency for LR to be unstable with too few training samples is one disadvantage of this method.

Linear Discrimination Analysis

Linear Discriminant Analysis (LDA) (Fisher, 1936) is typically used as a binary classification algorithm where a linear combination of the predictors is used to separate the two classes. LDA makes certain assumptions about the probability distribution function (PDF) of the input data, such as that it is normally distributed and that the distributions have the same covariance for each class. These assumptions are then applied to estimate the statistics (mean and variance) for each class that are used to calculate the discriminant, which in the univariate case is given by:

$$g_k(x) = x\frac{\mu_k}{\sigma^2} - \frac{\mu_k^2}{2\sigma^2} + \log(\pi_k), \qquad \textit{Eq. 2.4}$$

where k represents the kth class, $\mu_k$is the mean, σ^2 is the variance, and π_k is the overall probability of class k. With multivariate data, we can express the same equation using vector notation:

$$g_k(x) = x^T\Sigma^{-1}\mu_k - \frac{1}{2}\mu_k^T\Sigma^{-1} + \log\ \pi_k, \qquad \textit{Eq. 2.5}$$

where Σ^{-1} is the covariance matrix of the gaussian distributions. Solving for x^Tgives a linear equation used to predict class probabilities. When all the assumptions are met, LDA is a very powerful predictor with the ability to perform well on small datasets. Since this is rarely the case, LDA is often outperformed by other classifiers.

Support Vector Machine

The support vector machine (SVM) algorithm (Cortes and Vapnik, 1995) classifies the data by finding the hyperplane that maximizes the distance between the closest points of each class. The hyperplane represents the decision boundary that splits the data into its different classes. The SVM method can be applied to data that are both linearly separable

and non-linearly separable, each using continuous functions to define the SVM classifier. There are various ways of computing the classifier, with the hinge loss function being commonly used in data that are non-linearly separable. The hinge loss function is defined as:

$$\max(0, 1 - y_i(\vec{w} \cdot \vec{x_i} - b)), \qquad \textit{Eq. 2.6}$$

where w is the normal vector to the hyper plane, x_i are support vectors (points that lie nearest to the hyperplane), and b represents an offset from the origin. In this case the function is 0 if the support vector is on the correct side of the plane. If the support vector is on the incorrect side of the plane, the value of the function is proportional to the distance from the margin. We can then minimize the following function to define the hyper plane:

$$\left[\frac{1}{n}\sum_{i=1}^{n} max\ (0, -y_i(\vec{w} \cdot (x_i - \vec{b}))\right] + \lambda\|\vec{w}\|^2, \qquad \textit{Eq. 2.7}$$

where λ is a tradeoff parameter. One benefit of SVM is that it is not affected by the proportion of training data that belong to each class. This is a common problem with observed data since it is often the case that one outcome is more frequently observed than the other.

2.2.4.2 NON-LINEAR CLASSIFIERS

Gaussian Naïve Bayes

The Gaussian Naïve Bayes (GNB) classifiers (Cooper and Herskovits, 1992) is based on Bayes Theorem, which describes the probability of an event based on prior knowledge. Bayes theorem can be written as:

$$P(h|d) = \frac{(P(d|h)P(h))}{P(d)}, \qquad \textit{Eq. 2.8}$$

where $P(h|d)$ is the probability of the hypothesis h given the data, d, $P(d|h)$ is the probability of the data given the hypothesis is true, $P(h)$ is the probability of the hypothesis, and $P(d)$ is the probability of the data. Here, each feature is considered independent of one another, and therefore contributes to the probability of an event separately. The equation is defined by “prior probabilities” that are defined by the input

data. The goal of Naïve Bayes is then to estimate the posterior probability, $P(h|d)$. The hypothesis (or class) that produces the highest probability is the output and the assigned class for the given data. In other words, we can maximize the estimator function:

$$\hat{y} = argmax\ p(C_k) \prod_{i=1}^{n} p(x_i|C_k), \qquad Eq.\ 2.9$$

that is, the output $\hat{y}$ can be determined by computing the maximum of the probability of the feature data, $p(x_i|C_k)$, for a specific class C_k.

This algorithm estimates statistics of the data based on the assumption that they are normally distributed, which is not always the case, and the GNB algorithm is therefore not universally applicable. One advantage to the GNB classifier is its ability to estimate parameters with a relatively small number of training data. In addition, due to its simplicity, it is often a good starting point to test the predictive power of a data set.

Random Forest

The Random Forest (RF) algorithm (Ho, 1998; Breiman, 2001) is a decision tree classifier that works by splitting the dataset at various points (nodes) in the tree structure. The resulting split data are then found in what are called child nodes. This occurs recursively until a specific criterion is met (e.g. the final nodes contain data from a single class). RF generates bootstrap samples to determine an average classification across multiple randomly generated trees. We can define the number of trees that are generated, as well as the number of features that will be split at each level. To determine which feature to split on at each level of the tree, the concept of information gain is used. Information gain uses entropy defined as:

$$H(T) = -\sum_{i=1}^{J} P_i log_2 P_i, \qquad Eq.\ 2.10$$

where P_i is the probability of each class in a child node after a split in the tree. The information gain can be defined as:

$$I = H(T) - H(T|a), \qquad Eq.\ 2.11$$

where $H(T)$ is the entropy of the parent, and $H(T|a)$ is the entropy of the child node given the value of attribute *a*. Due to the random nature of its model generation, RF is a powerful and versatile classifier as it makes no general assumptions about the dataset. Its use of bootstrapping gives insight into the robustness of the generated model making it a robust predictor

K-Nearest Neighbour

The K-Nearest Neighbour (KNN) algorithm (Fix and Hodges, 1951; Cover and Hart, 1961) is a powerful classifier based on the simple assumption that points closer to each other in feature space are more similar than those further apart. It assigns classes to new data by determining the most frequent class of the K nearest neighbours, where K can be adjusted as well as the weights assigned to points based on distance. Cross-validation tests are used to choose values for K that minimize the classification error. As a non-parametric model, no assumptions are made regarding the distribution of the dataset, which broadens its applicability. KNN tends to work best when the sample size is large, which can limit its accuracy in many circumstances.

2.2.4.3 DEALING WITH A SMALL DATASET

One of the major limitations of using spatial data as input to a classification algorithm is the difficulty associated with increasing the size of a dataset. The spatial extent used to describe a single data point is, in a sense, arbitrary, but must also relate to the scale of the event that we are predicting. Due to the finite nature and limited availability of known data points, the size of our dataset is small compared to other ML applications. One concern associated with small datasets is the tendency for them to overfit the data. This occurs when a model corresponds too closely with the data that is was trained on, and therefore does not make accurate predictions on an unknown dataset (Hawkins, 2004). To minimize the effects of overfitting, we use linear models when applicable as their tendency to overfit the data is lower compared to non-linear models. In the case of the RF model, we set the maximum depth of the tree to seven, limiting the number of data splits. Other models (GNB and LDA) make simplifying assumptions that tend towards better performance on small datasets. In general, overfitting can be prevented by weighting the output from different models to produce a final prediction (Dietterich, 2000).

Another limitation associated with small datasets is dealing with unbalanced classes. Many algorithms are optimized when there is an equal number of training data belonging to each class. With larger datasets, data can be disposed of from the majority class with little consequence, which is not the case with small data sets. An alternative approach is to create synthetic data for the minority class to balance the input data. Here we apply the Synthetic Minority Over-sampling Technique (SMOTE) (Chawla et al., 2002) to balance the dataset. This is done by altering feature data one attribute at time within the difference to neighbouring data points of the same class. This creates a new data point that differs from the sampled point by the value for one feature.

2.3 RESULTS

2.3.1 FEATURE EVALUATION

Here we evaluate the relationship between five subduction zone features and the occurrence of slow slip events. Fig. 2.3 shows paired scatter plots depicting the distribution of input feature data based on the segment classification. The scatter plots show the relationship between all features for each segment used as input to the ML model based on their SSE classification. Since the relationship between the features is only represented in two dimensions, caution must be exercised when basing the predictive power of each feature on visual inspection of these plots.

2.3.1.1 SHORT-TERM SLOW SLIP EVENTS

Fig. 2.3 shows the feature plots comparing the short-term SSE “Yes” and “No” classes with 272 segments used as input. The sediment thickness data associated with the “Yes” class is shown to span from low to moderate values for sediment input. Two peaks are observed at the lower and higher ends of the distribution. The “No” distribution shows a smaller range than that observed for the “Yes” dataset with a single large peak at moderate sediment thickness values (~500 m). The distribution for subducting plate age shows a partially bimodal distribution with all segments with a “Yes” classification having an age of < 50 million years. The “No” input data shows a split distribution between young and old subducting lithosphere with the majority being over 50 Ma. We see similar results in the distributions for relative plate velocity. The “Yes” class data favours a slower

incoming plate velocity in comparison to the “No” class, with most segments having a relative velocity of > 65 mm/year. The plate dip input data shows strong overlap between the distributions for both classes. Segments assigned to the “Yes” class have subducting plate dips that span from shallow (< 10°) to steeply dipping (~40°), with the majority being shallowly to moderately dipping. Plate dip values assigned to segments belonging to the “No” class show a narrower range of values with all dips being shallower than 30°. The plate roughness distributions show significant overlap between the two classes with roughness estimates peaking at low to moderate values for both and extending across most observed values.

Table 2.1 shows the coefficients of each feature in the linear equation that is used to separate the two classes for our three linear algorithms: LR, LDA, and SVM. The coefficients can be interpreted as the contribution of each feature in determining the model output, where increasing positive values favour positive predictions and increasing negative values favour negative predictions. Subducting plate age is considered by all three models to most heavily influence the model prediction, with older plates correlating with a reduced likelihood of a positive prediction. Relative plate velocity is also found to consistently favour negative predictions across all three models but with lower absolute values. Sediment thickness values are consistently positively correlated with short-term SSE occurrence across all three models. Neither plate dip or seafloor roughness appear to contribute to the occurrence, or lack thereof, of short-term SSEs.

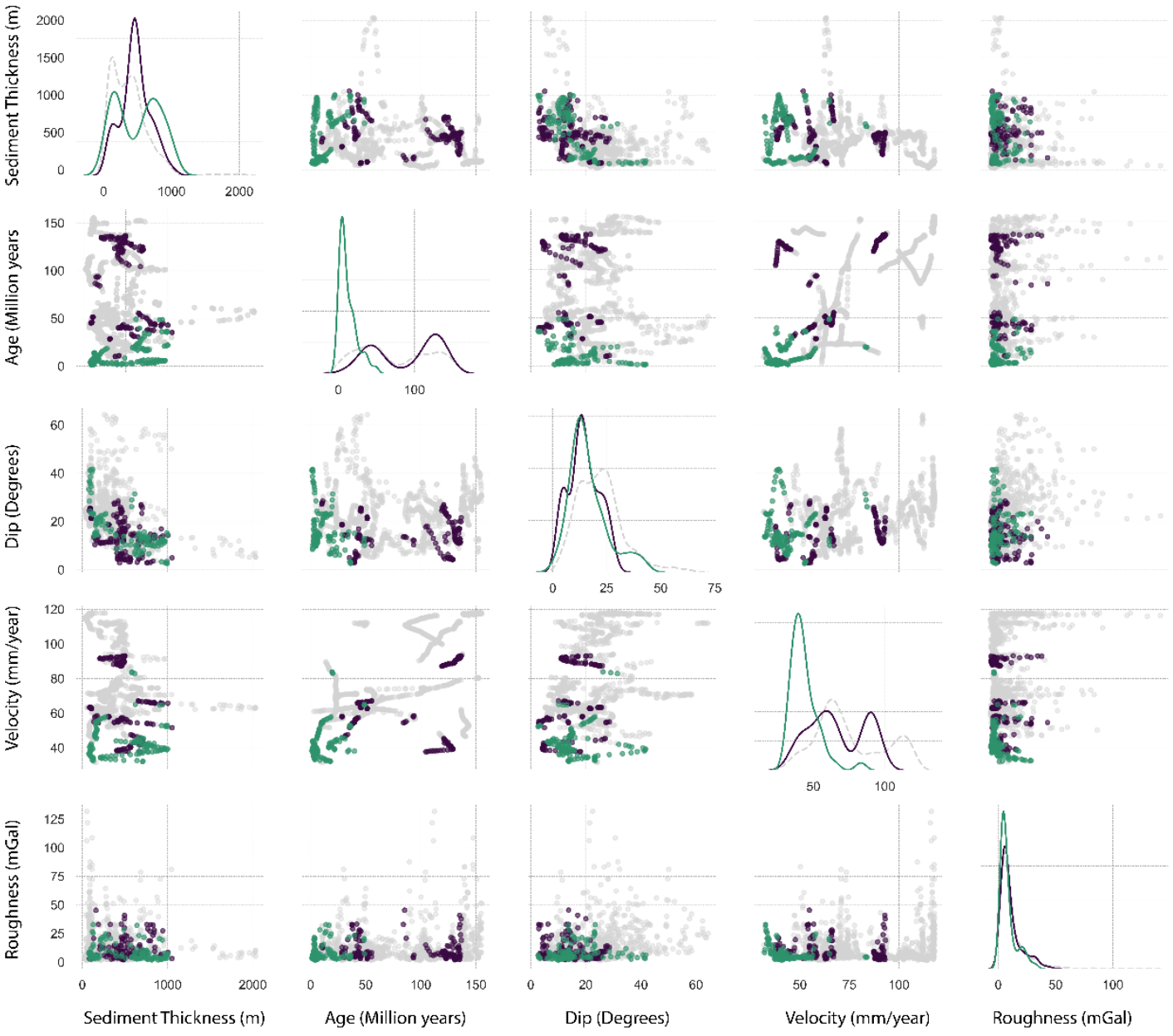
Sediment Thickness (m)
Age (Million years)
Dip (Degrees)
Velocity (mm/year)
Roughness (mGal)

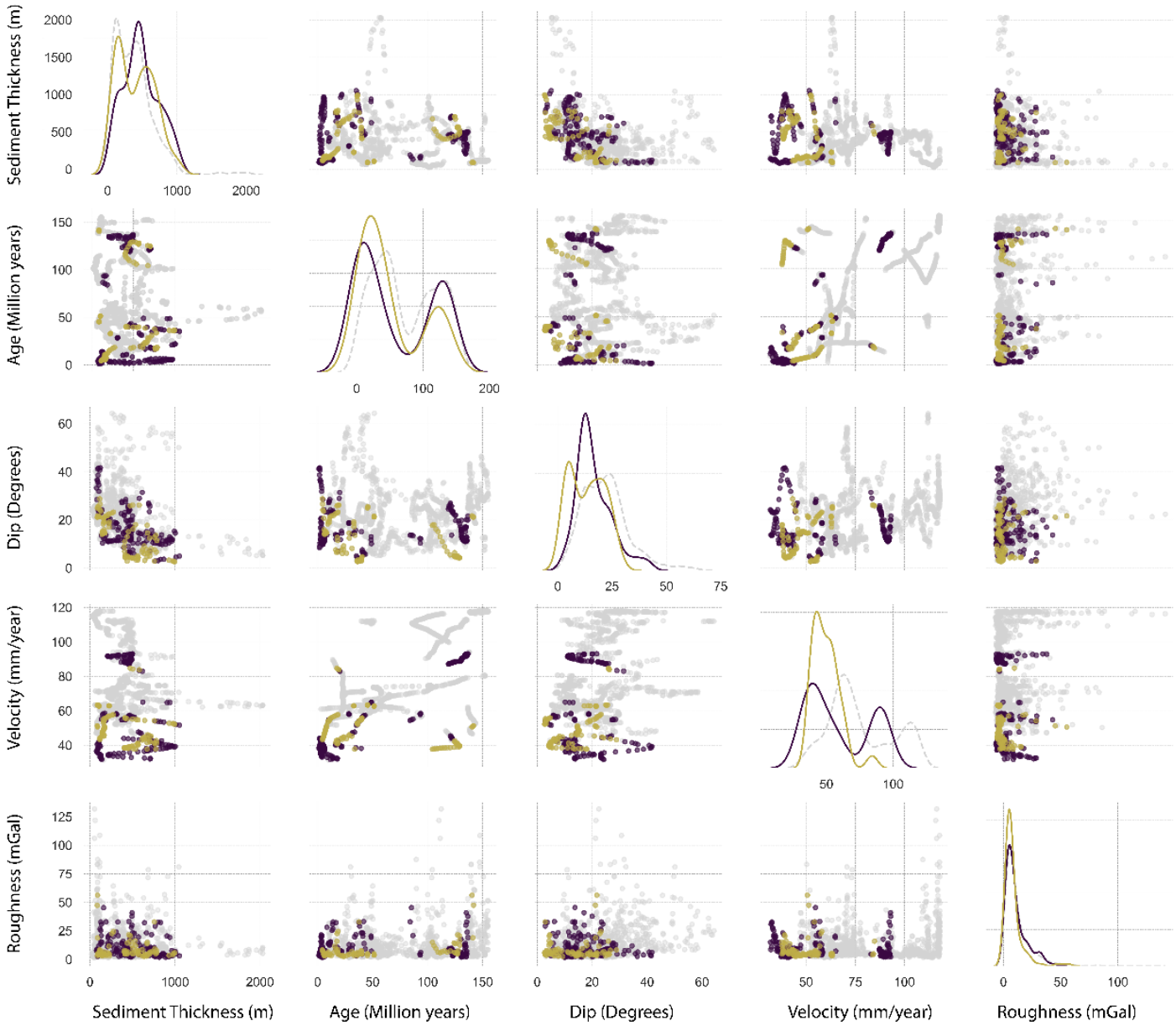

FIGURE 2.3: PAIRED SCATTER PLOTS AND DISTRIBUTIONS OF INPUT FEATURE DATA. SCATTER PLOTS SHOW THE RELATIONSHIP BETWEEN ALL FEATURES FOR EACH SEGMENT USED AS INPUT TO ML MODELS BASED ON THEIR SSE CLASSIFICATION IN THE SHORT-TERM CASE (A): YES (GREEN) OR NO (PURPLE) AND IN THE LONG-TERM CASE (B): YES (YELLOW) OR NO (PURPLE). GREY POINTS AND CURVE REPRESENT INPUT FROM ALL SEGMENTS GLOBALLY. DISTRIBUTIONS SHOW FREQUENCY OF ASSIGNED SCALER VALUE FOR BOTH SSE CLASSES IN OUR TWO DATASETS.

TABLE 2.1: CONTRIBUTION OF EACH FEATURE TO CLASSIFICATION ACCURACY FOR LDA, LR, AND SVM MODELS IN THE SHORT-TERM AND LONG-TERM SSE CASES. FEATURES WITH LARGEST VALUES (POSITIVE OR NEGATIVE) HAVE GREATER EFFECT ON THE REGRESSION VALUE (CLASS LABEL). POSITIVE VALUES IMPLY INCREASED LIKELIHOOD OF A "YES" CLASS LABEL WHEREAS NEGATIVE VALUES IMPLY INCREASED LIKELIHOOD OF A "NO" CLASS LABEL.

	LR Mean	LR Standard Deviation	SVM Mean	SVM Standard Deviation	LDA Mean	LDA Standard Deviation
Short-term SSEs						
Sediment Thickness	1.92	0.87	1.89	0.58	0.50	0.45
Subducting Plate Age	-19.07	6.88	-17.04	5.01	-7.04	0.89
Slab Dip	0.06	0.67	0.09	0.47	0.44	0.28
Relative Plate Velocity	-1.57	1.33	-0.91	0.80	-1.19	0.27
Plate Surface Roughness	-0.32	0.23	-0.19	0.17	-0.57	0.21
Long-term SSEs						
Sediment Thickness	-1.93	0.45	-1.97	0.39	-1.95	0.42
Subducting Plate Age	0.37	0.62	1.01	0.45	0.59	0.56
Slab Dip	-1.37	0.33	-1.27	0.27	-1.37	0.29
Relative Plate Velocity	-1.05	0.42	-1.21	0.25	-1.05	0.34
Plate Surface Roughness	-0.46	0.26	-0.73	0.24	-0.49	0.18

2.3.1.2 LONG-TERM SLOW SLIP EVENTS

Fig. 2.3 shows the feature plots comparing the long-term SSE “Yes” and “No” classes with 257 segments used as input. Sediment thickness values observed for the “Yes” class show a narrower distribution than that of the short-term dataset and a higher proportion of low values. The distributions of age estimates show nearly identical behaviour for both the “No” and “Yes” classes. Here we observe two peaks at ~50 Ma and ~150 Ma with only sparse data at moderate ages. The plate dip distributions for the “Yes” class spans a smaller range than that of the “No” class, varying from shallowly (< 10°) to moderately dipping (~40°). A distinguishing feature between the “Yes” class from both datasets is the tendency for the shallowest dipping values (< 10°) to favour the “Yes” class from the long-term dataset. The relative plate velocity distributions show some clear distinguishing features between the two classes. The “Yes” class has a concentration of observed values between ~40 and ~60 mm/year while the “No” class has two peaks at high and low relative velocities. Overall the distribution is shifted towards slightly higher velocities than those observed from the “Yes” class in the short-term dataset. Roughness values show similar behaviour between the two classes and span from 0 to 50 mGal for both classes.

Coefficients of our linear models shown in Table 2.1, can again be interpreted as the contribution of each feature in determining the model output. Here sediment thickness has the highest absolute value with increasing values leading to a decrease in likelihood of long-term SSE occurrence. Slab dip and relative plate velocity have the next highest absolute values with increasing values, again, decreasing the likelihood of a positive prediction made by the models. Plate age and roughness values have the smallest contribution to all three model outputs with increasing age increasing the likelihood of a positive prediction and increasing seafloor roughness decreasing the likelihood of a positive prediction for long-term SSEs.

2.3.2 MODEL EVALUATION

Here we test the performance of the six ML algorithms using cross validation. The data are shuffled where 70% of the data is selected as training data and the other 30% is reserved as the test set. The resulting trained models are applied to the test set where

the performance of the model is evaluated based on correct predictions. This is repeated 50 times for each of the 10 randomly generated datasets, which have been altered with additional synthetic data, to retrieve performance statistics on each model. To further test model performance, we quantify the *recall* and *precision* (Kent et al., 1955) of the model results, where

$$recall = \frac{true\ positives}{true\ positives + false\ negatives}, \qquad Eq.\ 2.12$$

$$precision = \frac{true\ positives}{ture\ positives + false\ positives}. \qquad Eq.\ 2.13$$

The recall quantifies the fraction of total detections described by the model while precision quantifies the ability of the classifier to not label a sample as positive if it is negative. To determine a representative estimate for each model, we split the input data set into a training set consisting of 2/3 of the data set and a test set consisting of 1/3 of the data set. The model was fitted to the training set for 10 random iterations and the average recall and precision was computed for each model. Table 2.2 shows the resulting statistics for each model.

These results show varying levels of performance for each model. For the short-term SSE models, RF is the best performing algorithm with high accuracy, low standard deviation, high levels of recall and precision. Our worst performing model is LDA, scoring the lowest mean accuracy, highest standard deviation, and low precision. The LDA model recall is very high due to its tendency to over-estimate positive predictions, which is counteracted by its inability to correctly predict true negatives. The GNB, LR, SVM, and KNN models perform similarly, with high mean accuracy, recall, and precision, and low standard deviations.

TABLE 2.2: RESULTS OF CROSS-VALIDATION TEST OF MODEL ACCURACY FOR GAUSSIAN NAÏVE BAYES (GNB), RANDOM FOREST (RF), LOGISTIC REGRESSION (LR), SUPPORT VECTOR MACHINE (SVM), K-NEAREST NEIGHBOUR (KNN), AND LINEAR DISCRIMINANT ANALYSIS (LDA) MODELS FOR THE SHORT-TERM AND THE LONG-TERM SSE CASES. THE CROSS-VALIDATION TEST SHOWS THE STATISTICS OF MULTIPLE CLASSIFYING ROUNDS USING DIFFERENT TRAINING AND TEST SETS AND CAN BE INTERPRETED AS AN INDICATION OF ROBUSTNESS. EACH MODEL'S RANK, WHICH IS ASSIGNED BASED ON PERFORMANCE, AND CORRESPONDING WEIGHT (WHICH SUM TO 1) ARE LISTED.

Short-term SSEs						
Model	Mean Accuracy	Standard deviation	Recall	Precision	Rank	Weight (x2.6)
GNB	93.3	2.0	94.2	92.9	4	0.3
RF	97.4	1.9	96.4	98.8	1	1.0
LR	95.1	1.9	95.0	95.5	3	0.5
SVM	95.8	1.9	95.1	95.7	2	0.5
KNN	92.8	2.4	95.1	92.7	5	0.3
LDA	87.8	3.7	97.7	83.1	6	0
Long-term SSEs						
Model	Mean Accuracy	Standard deviation	Recall	Precision	Rank	Weight (x2.0)
GNB	69.8	5.4	84.3	51.4	6	0
RF	93.2	2.9	95.2	92.6	1	1.0
LR	75.5	4.0	78.2	75.0	4	0
SVM	86.7	3.0	78.4	75.8	3	0.5
KNN	87.1	3.1	91.0	82.6	2	0.5
LDA	74.3	4.3	78.5	71.4	5	0

For the long-term SSE models, RF is again the best performing algorithm with high accuracy scores across all measures. Out of the remaining models only the SVM and KNN perform sufficiently well to include in the final weighted model. Overall, the long-term SSE models perform worse than our short-term SSE models. This may have implications on the validity of using subducting plate features (or these features in particular) in evaluating the conditions that favour long-term events. It is possible that overriding plate features may play a larger role in long-term SSE nucleation. Finally, our models are ranked from 1 to 6, with 1 being the best performing model, and 6 being the worst for both the short-term and long-term models. We use the resulting ranks to assign a weight to each model (Table 2.2), which will be used in predicting SSEs from the "unknown" data set (see below).

2.3.3 PREDICTIONS

2.3.3.1 SHORT-TERM SLOW SLIP EVENTS

Here we present the results of our final model (Fig. 2.4). We use a weighted average of the probability of short-term SSE occurrence using all models, where the weights are related to each model's ranking during cross-validation (Table 2.2). We exclude the LDA model as it is the worst performing algorithm as shown through the cross-validation tests. Along the Aleutian subduction zone, we see high probabilities of short-term SSE occurrence beginning at Unalaska Island and continuing East to Kodiak Island. Further west we see moderate probabilities starting east of the Near Islands and continuing to the Adreanof Islands. West of the Adreanof Islands there is universally low probability of short-term SSE occurrence.

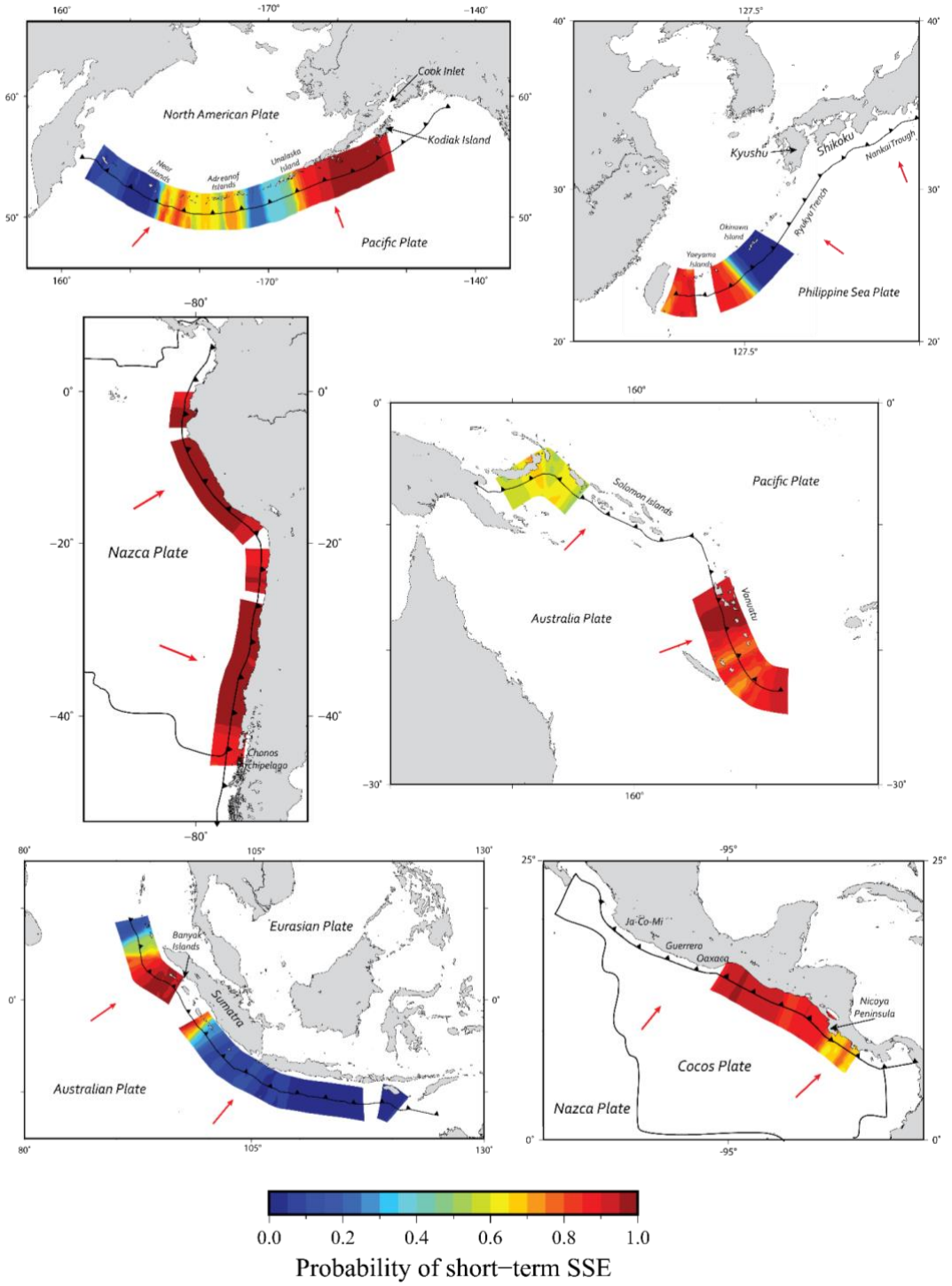

FIGURE 2.4: PROBABILITY OF SHORT-TERM SLOW SLIP OCCURRENCE AS PREDICTED BY OUR WEIGHTED AVERAGED ML MODEL FOR 6 REGIONS OF INTEREST: A) ALASKA/ALEUTIANS; B) SOUTHWEST JAPAN; C) SOUTH AMERICA; D) SOLOMON/VANUATU; E) SUMATRA; F) MIDDLE AMERICA. SUBDUCTION ZONE TRENCHES ARE COLOUR CODED BASED ON THE PROBABILITY OF OCCURRENCE ACCORDING TO THE SCALE.

Along the Middle America subduction zone, our model predicts widespread high probability of short-term SSE occurrence. Probabilities are highest in the north but decrease to less than 60% at the southernmost reach of the Middle America Trench. Along the Ryukyu Trench we observe high probabilities at the western extent, which suddenly decrease at Okinawa Island. The probabilities remain low eastward along the Ryukyu Trench until Kyushu. Along the Solomon Islands, moderate probabilities are predicted across its western portion. Limited data availability prevents predictions from being made further east. Along South America, our model predicts widespread short-term SSE occurrence.

2.3.3.2 LONG-TERM SLOW SLIP EVENTS

Long-term SSE predictions (Fig. 2.5) were made using a weighted average of the three best performing models: RF, KNN, and SVM. Widespread moderate to high probabilities of long-term SSEs are predicted along the Tonga-Kermadec subduction zone with probabilities reaching over 90% along its southernmost extent and most segments having probabilities over 50%. Along Kuril-Kamchatka, high probabilities are predicted throughout its central portion. Similar widespread high probabilities are predicted across the Mariana Trench. These three regions represent our models' favoured locations for long-term SSE nucleation. Moderate probabilities of between 30 and 70% are predicted along Izu-Bonin, Ryukyu, the central to eastern portion of the Aleutians and, the central and eastern portions of the Sumatran Subduction Zone. Primarily low probabilities are predicted across South America and Middle America.

2.4 DISCUSSION

2.4.1 FEATURE EVALUATION

2.4.1.1 SHORT-TERM SSES

We can identify subduction zone characteristics that favor short-term SSEs based on the distribution of observed values for each feature. The universal observation of young subducting lithosphere favouring SSEs provides support for the temperature/pressure

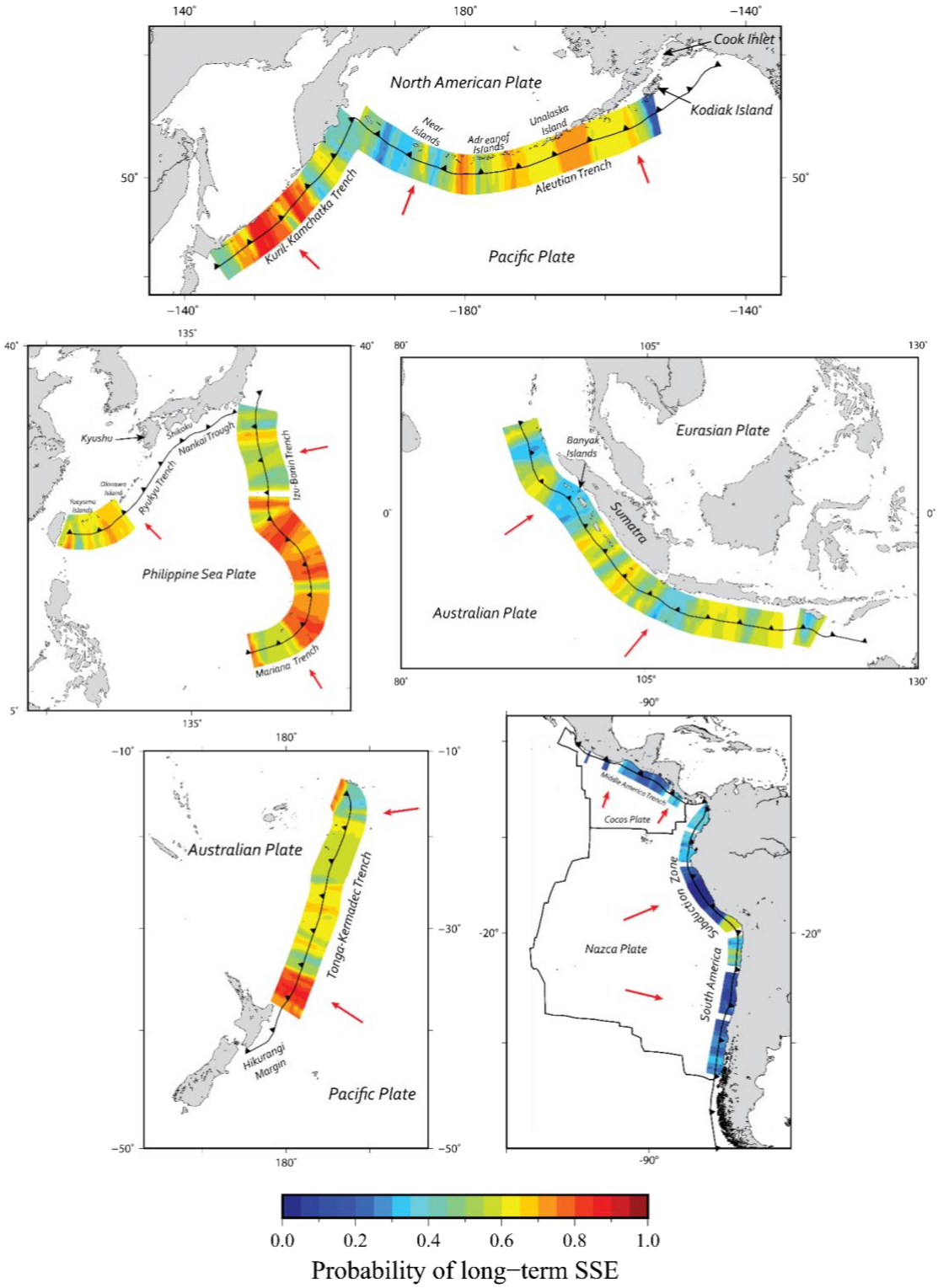

FIGURE 2.5: PROBABILITY OF LONG-TERM SLOW SLIP OCCURRENCE AS PREDICTED BY OUR WEIGHTED AVERAGED ML MODEL FOR 5 REGIONS OF INTEREST: A) NORTHERN PACIFIC B) EASTERN PACIFIC; C) SUMATRA; D); HIKURANGI/TONGA-KERMADEC; E) SOUTH AND MIDDLE AMERICA. SUBDUCTION ZONE TRENCHES ARE COLOUR CODED BASED ON THE PROBABILITY OF OCCURRENCE ACCORDING TO THE SCALE.

driven model of fluid introduction due to metamorphic dehydration reactions, based on the inverse relationship between lithospheric age and temperature. From these observations, it is likely that, in order to provide the necessary conditions for short-term SSEs, high temperatures are required to ensure the threshold conditions for these reactions occur at depths where SSEs are found to occur. The tendency for segments that host short-term SSEs to have slower relative plate velocities also supports this model. In this case, the lower relative velocities increase the amount of time the plate interface spends at specific temperature and pressure conditions. To generate enough fluid pressure to promote specific slip behaviors, it is likely that longer durations spent in these ideal conditions favor short-term SSEs. Subducting sediments is a known source for introducing fluids into a subduction zone. Our observation of a split distribution between high and low amounts of subducting sediment for the “Yes” class suggests that in some cases increased pore fluid pressure from increased sediment input may aid in the nucleation of SSEs, but it is not necessarily required. The wide range of values observed for subduction plate dip and plate roughness associated with segments fr1om the “Yes” class implies that these values do not independently constrain the occurrence of short-term SSEs. This does not mean that these characteristics do not influence their behavior, as the interaction between all features may be still necessary to promote short-term SSE occurrence.

2.4.1.2 LONG-TERM SSES

Here we can observe some apparent differences between the distribution of feature values for short-term and long-term SSEs. Firstly, the universal observation of young subduction lithosphere is not observed with long-term SSEs, therefore the possible requirement of high subducting plate temperatures associated with short-term events may not be important for long-term events. It is possible that the tendency for long-term SSEs to occur up dip of short-term SSEs indicates that different temperature/pressure conditions are necessary to generate these events, and that the metamorphic dehydration reactions that produce the necessary pore fluid pressures to generate short-term SSEs are not needed in this case. The high proportion of low sediment input associated with long-term SSEs may again have implications on the lesser role of fluid introduction in their generation. High sediment input may increase pore fluid associated with short-term SSEs

but this association is less obvious with long-term SSEs. Another notable difference is observed with subducting plate dip. Generally shallower dips are associated with long-term events in comparison with the other classes. This may reflect the requirement for long-term SSEs to occur when the plate interface is in lower temperature/pressure conditions for a greater length of time. This logic applies again to the observation of slow incoming plate velocities for most segments hosting any SSEs. As mentioned previously, it is likely the interaction between the different features that dictates the occurrence of short-term versus long-term SSEs. Overall, the main pathways of fluid introduction into subduction zones seem to be more heavily correlated with short-term rather than long-term SSEs, with implications on the varying role of high fluid pressures in generating these events.

2.4.2 MODEL PREDICTIONS

To interpret the results of model predictions, we must first consider the implications of the model input and the limitations associated with a five-parameter model. Our model predictions relate the probability of slow slip occurrence based on how similar subducting zone characteristics are to ones where SSEs readily occur. The resulting model also assumes predictive power of all features used as input and that these features are sufficient to describe the mechanistic nature of slow slip nucleation. There are likely more complex interactions of many more subduction characteristics (including those of the overriding plate) that influence how accumulated strain is released. These results can be used as a first order estimate of likely slow slip locations based on five easily quantified subducting plate characteristics.

2.4.2.1 SHORT-TERM SSES

Due to sparse station distribution along the Aleutians, short-term SSEs have yet to be observed. Currently there is some evidence to suggest that tectonic tremor does occur in various regions across the Aleutian Islands (Peterson et al., 2011). Our model predicts similar occurrence of short-term SSEs in regions with previously observed tectonic tremor, including along the Adreanof Islands and the eastern portion of Unalaska Island. Additionally, our model predicts a lack of events in regions where tectonic tremor is not detected including the western portion of the Aleutians. These low probabilities are likely

the result of the transition from moderate subducting plate ages (~50 million years) to much older plates (>100 million years).

Along the Ryukyu Trench we observe a shift from high probability to low probability of short-term SSE occurrence corresponding with the changing age of the subducting lithosphere. In comparison with previous observations of short-term SSEs in the region (Nishimura, 2014), the transition to low probabilities corresponds with the observed switch from deeper events (>25 km) to shallow events (<20 km). This could have implications as to the role of temperature conditions in generating deep short-term SSEs.

The next region of interest is along the South America Subduction Zone in southern Chile. Similar to observations in Alaska, tectonic tremor has been observed here with no correlation to short-term SSEs (Gallego et al., 2013). The high probability prediction provides evidence that the conditions here are favourable for short-term SSEs, and that lack of detection may be an artefact of low magnitude events that are below the detection threshold. Our model goes on to predict widespread high probabilities along the entire extent of the subduction zone. This result questions our classification of certain segments along the South American Subduction Zone as hosting no short-term SSEs, which was based on the detection of shallow and/or long-term events but not short-term events in the area. There is no significant change in subducting lithosphere characteristics from the “No” labelled segments and the “Yes” predicted segments so we would expect similar slow slip behaviour in both. A possible alternative explanation to this discrepancy is that our model is likely limited by the predictive power of the features used.

Next, we examine the predictions made along the Sumatra Trench. Geologic evidence using coral microatolls to provide records of vertical deformation have been used as evidence of slow slip events along the Banyak Islands (Meltzner et al., 2015; Tsang, et al., 2015). Current evidence supports the occurrence of a 15-year long event, which occurred from 1966 to 1981, but systematic searches for shorter events have been unsuccessful (Feng et al., 2015). Our model shows similar behaviour here to that observed along South America, with high probabilities of short-term SSEs adjacent to the “No” labelled segments. We observe a general increase in subducting sediment thickness north of the classified “No” segments, which may explain the contrasting high probability

predictions here. Denser station coverage as well as more systematic searches along the northern portion of the island of Sumatra may be necessary to detect short-term SSEs. Further east we observe universally low probabilities, a result of older subducting lithosphere that is negatively correlated with short-term SSEs.

Along the Solomon Islands and Vanuatu, there are no reports of SSE behaviour as a result of sparse station distribution and lack of studies. The moderate age of subducting lithosphere along the western portion of the Solomon Trench makes it a possible candidate for hosting SSEs. The high relative velocity seems to contribute to our model predicting more moderate probabilities of short-term SSE occurrence due to the general negative correlation between the two. Along Vanuatu, even younger subducting plate ages make it an even better candidate for hosting SSEs, as reflected by the widespread high probabilities predicted by our model.

2.4.2.2 LONG-TERM SSES

Here we analyze the predictions of long-term SSEs made by the weighted model. In Sumatra, speculation of long-term slow slip behaviour is based on geological evidence, as mentioned in the previous section. Our model predicts moderate probability of long-term SSE occurrence in this region with estimates within 45-50%. In South America, slow slip events have long been searched for, but with sparse GNSS station distribution, they are difficult to detect. Our models strongly favour the occurrence of short-term over long-term SSEs, which is likely associated with the young subducting lithosphere found across most of the South American Subduction Zone. Recent observations of long-term events in the Atacama region (Klein et al., 2018) are associated with older oceanic lithosphere (~50 million years old), which is in line with the lack of obvious correlation between young subducting lithosphere and long-term SSE occurrence. Our model predicts moderate probabilities of long-term SSE occurrence in this region.

Along the Kuril-Kamchatka, Izu-Bonin, Tonga-Kermadec, and Mariana Trenches, there is a notable lack of megathrust earthquake occurrence. The moderate-to-high probabilities of long-term SSE occurrence predicted by our models suggest that a significant amount of strain accumulation may be accommodated by recurring slow slip

events. Isolated observations of long-term SSEs in the Bonin islands suggest that slow slip events can (and does) occur in these types of subducting environments.

2.5 CONCLUSION

We apply Machine Learning techniques to evaluate subduction zone characteristics and predict slow slip events using scalar values representing certain kinematic, geometric, and physical properties of subducting oceanic lithosphere. We generate various models based on two classification schemes, separated based on the occurrence (or lack thereof) of short and long-term SSEs. The most relevant features used in the classification of short-term SSEs are subducting plate age, relative velocity and sediment thickness, with lower values of the former two correlating with increased probability of short-term SSE occurrence and higher values for sediment thickness correlating with increased probability. These results are consistent with the hypothesis that elevated pore fluid pressures are necessary to generate short-term SSE and ETS like events through prolonged exposition of the subducting plate to specific metamorphic dehydration reactions. However, we cannot conclude based on these results whether the features contribute to slow slip in the way described and further validation is required to confirm this hypothesis. The models predict short-term SSEs in regions where their occurrence has been speculated, including southern Chile and along the Aleutian Subduction Zone, as well as long-term SSEs in a variety of poorly monitored regions (e.g. the Pacific subduction zones). Overall, our models trained on long-term SSE classification perform poorer than those trained on the short-term dataset. This may have implications in the lesser contribution of subducting plate features in the generation of long-term events. It is likely necessary to include overriding plate features to constrain the physical controls of long-term events and, perhaps to a lesser extent, short-term events. The continued detection of slow slip events is overall necessary to improve the characterization of environments hosting these events and provide further constraints of the physical mechanisms that drive their occurrence.

3

MARGIN-WIDE VARIATIONS IN SLAB DEHYDRATION IN CASCADIA AND THEIR RELATIONSHIP TO SLOW SLIP

Abstract

Slow slip events are observed in subduction zones globally, with a wide range of variations in behaviour, including the periodicity and magnitude of events. These variations are observed both within and across different subduction zones. Due to their role in controlling strain accumulation and potential nucleation of regular earthquakes, understanding the physical environment of slow slip events and the source of their observed variability is critical to understanding seismogenic processes. Here we calculate thermal models for 10 trench-normal profiles along the entirety of the Cascadia subduction zone. The models incorporate lateral changes in incoming plate age and sediment input, as well as slab geometry and overriding plate structure. Temperatures at the location of peak slow slip and tremor occurrence (depths of 30-40 km) vary from 525°C in southern Cascadia, to 475°C in central Cascadia, to 550°C in northern Cascadia. The variability in thermal structure and slab geometry leads to changes in the rate of calculated fluid flux in the vicinity of the mantle wedge corner where slow slip events are observed. Fluid flux rates calculated within 25 km and 50 km downdip of the mantle wedge corner show an inverse relationship with the recurrence time of slow slip with highest value observed in southern Cascadia, followed by northern Cascadia, and then central Cascadia. Other along-strike variability in tremor behaviour, such as tremor strength, correlates spatially with changes in calculated fluid flux pattern but the relationship between these parameters is not readily defined. This study provides support for models where variations in the rate of fluid production in the vicinity of the mantle wedge corner are a potential mechanism controlling the rate of pore fluid pressure buildup and fluid release during slow slip.

3.1 INTRODUCTION

The release of accumulated strain at subduction zones has long been thought to occur via either stick-slip (earthquakes) or stable creeping processes (e.g., Scholz, 1998). A transient form of large-scale, slow stress release phenomena, collectively referred to as slow slip events (SSEs; Jolivet and Frank, 2020), were discovered in recent decades using networks of Global Navigation Satellite System receivers at various subduction zones (Hirose et al., 1999; Dragert et al., 2001). A wide variety of these slow slip phenomena are now found at the root of most large plate boundary fault zones (see reviews in Bürgmann, 2018; Behr and Bürgmann, 2021; Jolivet and Frank, 2020). Typically, SSEs (most often with accompanying non-volcanic tremor) can be observed as either short-term, lasting from days to weeks, or long-term, lasting from months to years.

The seismogenic behaviour of subduction zones is thought to be partially controlled by temperature through either rate-and-state dependent friction (e.g., Scholz, 1998) or rheological models (e.g., Hyndman and Wang, 1993). There is evidence that SSEs are at least partially controlled by similar processes (e.g., Gao and Wang, 2017; McLellan and Audet, 2020). For instance, the largest SSEs have been mostly observed in subduction zones of warm (i.e., young) oceanic lithosphere (e.g., Cascadia, Nankai, and Mexico; Schwartz and Rokosky, 2007; Beroza and Ide, 2011) and at the root of continental transform faults (e.g., Shelly, 2017). A direct relationship between SSEs and temperature is more difficult to establish than in the case involving regular “fast” earthquakes as SSEs have been observed at different temperature ranges within the same subduction zone (e.g. ~550°C-600°C in southern Cascadia (Boyarko and Brudzinsk, 2010) and ~450°C-500°C in northern Cascadia (Wech and Creager, 2008)) as well as across different subduction zones (e.g. 100-400°C in Hikurangi (McCaffrey et al., 2008). Instead of a purely thermal control on SSEs, several studies have linked their location to metamorphic dehydration reactions (e.g., Peacock, 2009; Fagereng and Diener, 2011; Condit et al., 2020), where estimated peaks in fluid release along pressure-temperature (P-T) paths of subducting oceanic crust largely coincides with the location of observed SSEs in various subduction zones. Other studies link the location of fluid

release to the mantle wedge corner (MWC) where fluid migration is necessary to channel fluids to the site of SSE occurrence (e.g., Hyndman et al. 2015).

Currently, there are limited studies that examine the variability of the locations of deep slow slip and metamorphic dehydration along an entire subduction zone (e.g., Yabe et al., 2014). The Cascadia subduction zone (CSZ), located along the western coast of North America, provides one of the most reliable sources of SSEs and tremors globally (Rogers and Dragert, 2003). Their occurrence is observed along the entirety of the subduction zone (Fig. 3.1) at depths of 30-45 km near the base of the thick plate interface shear zone (Calvert et al., 2020), with significant along-strike variations in their spatio-temporal and dynamic properties. For instance, recurrence intervals vary from 10 to 19 months (Brudzinski and Allen, 2007) and tremors accompanying slow slip show a large range of radiated seismic energy with highest rates occurring in northern Cascadia, and the lowest rates in central Cascadia (Wech, 2021). Detailed studies of varying slab dehydration along strike of the CSZ are comparatively rare; in those studies, the CSZ is broadly divided into northern, central, and southern regions (e.g., Gao and Wang, 2017; Condit et al., 2020). Although variations in fluid flux have been inferred from seismic velocity models (e.g., Delph et al., 2018), no study has focused on modeling the variability of slab dehydration conditions in the CSZ due to changes in P-T paths, or explored possible relations with the variability of deep slow slip.

In this study, we determine the thermal structure of 10 margin-normal (Fig. 3.1), equally spaced profiles along the CSZ to quantify the relationship between changing patterns in fluid release from slab dehydration and along-strike variation in SSE behaviour. We first explore the potential links between metamorphic fluid generation and migration with slow slip behaviour. We then present updated thermal models of the entire CSZ. Combined with petrologic modelling of the major lithologies found in the subducting oceanic plate, we estimate fluid flux patterns in the vicinity of SSE source regions. Overall, we attempt to relate the segmented behaviour of SSEs to changing subducting plate parameters that influence the thermal and petrologic structure of a subduction zone.

3.1.1 FLUID CONTROLS ON SLOW SLIP IN CASCADIA

Along the CSZ, the young and warm Juan de Fuca plate system (Juan de Fuca, Gorda and Explorer micro-plates; see Fig.3.1) is subducting at a low dip angle, which leads to shallow termination of the seismogenic zone and the extensive exposure of the megathrust to pressure and temperature conditions favorable to SSE occurrence (e.g., Hyndman, 2013). However, the CSZ exhibits along-strike variations in SSE behavior (e.g., Brudzinski and Allen, 2007) that cannot be explained by the relatively gradual and predictable differences in temperature in the SSE source region due to slab age alone (e.g., McCrory et al., 2014). Instead, SSE may be influenced either by the spatial distribution of in situ fluid production through dehydration of the subducting plate (e.g., Condit et al., 2020), or the mobilization of slab-derived fluids to the SSE region from deeper sources (e.g., Hyndman et al., 2015). Shallow metamorphic fluid production in slabs depends in part on P-T conditions that vary based on several parameters such as subducting plate age, convergence rate, input sediment thickness, and plate interface dip. At the CSZ, subducting plate age ranges from ~9 Ma to ~5 Ma (Wilson, 1993), the convergence rate from ~33 mm/yr to ~43 mm/yr (Angus et al., 2011), and the sediment thickness from ~2500 m to ~3500 m, the majority of which is accreted onto the margin (Wang and Trehu, 2016). The plate geometry also changes with the southernmost portion dipping more steeply in comparison to the north (McCrory et al., 2012). These well-constrained changes in subduction zone parameters along the CSZ could lead to variations of in situ fluid production and explain the differences in observed SSE behaviour. At a global scale, in situ fluid production at warm subduction zones has been found to coincide with the location of SSEs (Condit et al., 2020), without requiring significant fluid migration from deeper sources.

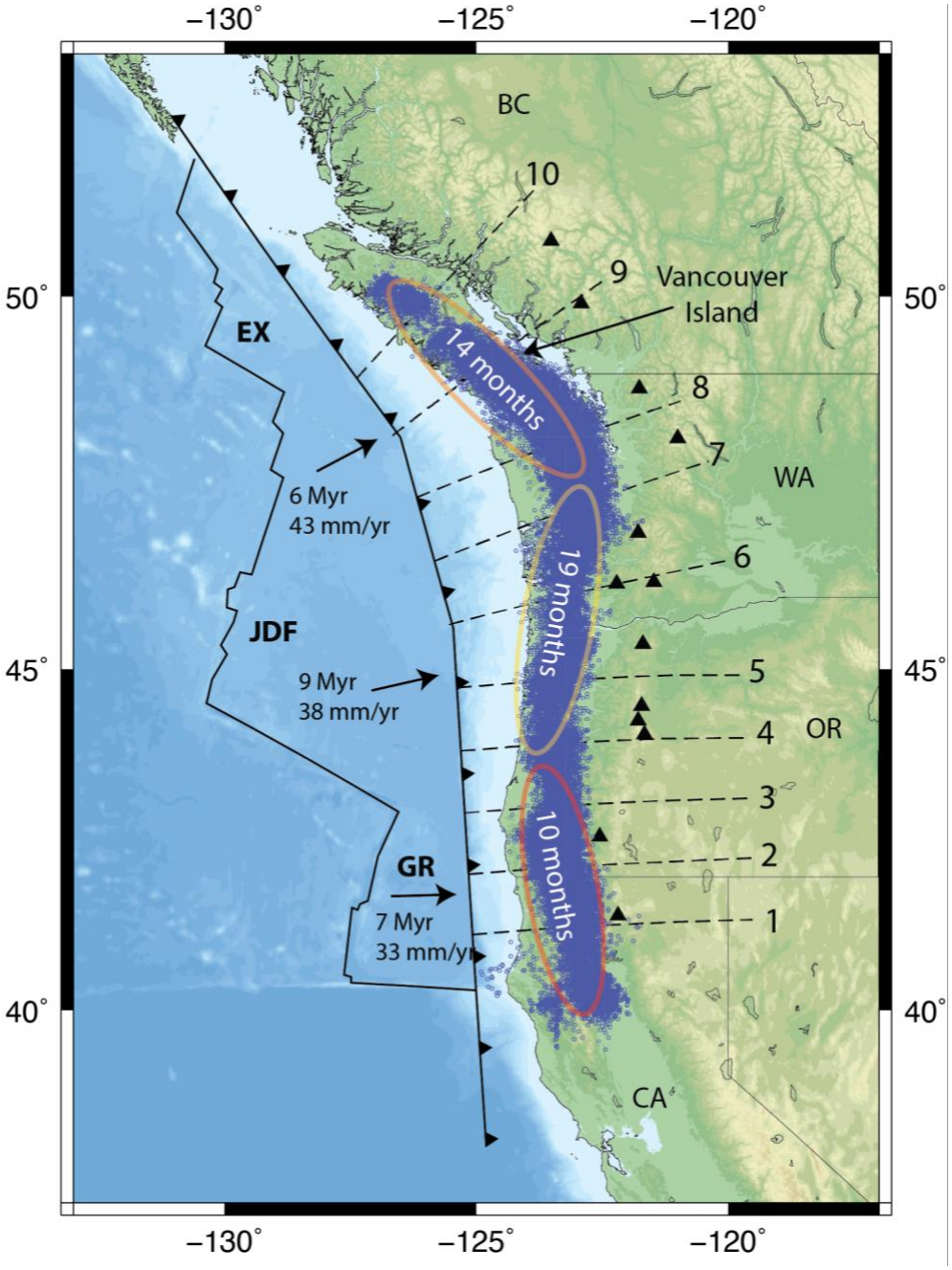

FIGURE 3.1: TREMOR MAP OF THE CASCADIA SUBDUCTION ZONE WITH THE LOCATION OF MODELLED PROFILES ANALYSED IN THIS STUDY. TREMOR DATA IS SOURCED FROM WECH AND CREAGER (2008). SUBDUCTING PLATE PARAMETERS ARE LABELLED, SHOWING THE CHANGE FROM THE SUBDUCTION OF THE GORDA PLATE (GR) IN THE SOUTH, THE JUAN DE FUCA (JDF) PLATE IN THE CENTER, AND THE EXPLORER PLATE (EX) IN THE NORTH. BLACK TRIANGLES SHOW THE LOCATION OF ARC VOLCANOES.

In contrast to the in-situ fluid production model, the spatial coincidence of the wet, serpentinized MWC in relation to tremor has led to the suggestion that fluid mobilization mediated by megathrust permeability structure may instead control SSE behavior (e.g., Hyndman et al., 2015; Audet and Bürgmann, 2014). The structural environment that hosts SSEs is characterized by a low seismic velocity layer (LVL; Abers, 2005) with anomalously high P-to-S seismic velocity ratios that suggest high pore-fluid pressure and low vertical permeability (Bostock, 2013; Audet et al., 2009; Peacock et al., 2011; Audet and Kim, 2016; Delph et al., 2018; Calvert et al., 2020). Coincidental changes in the seismic velocity of the LVL before, during and after SSEs provides evidence for the potential role in the fluctuation in pore-fluid pressures, related to cyclic fluid accumulation, in generating recurrent SSEs (Frank et al., 2015; Warren-Smith et al., 2019; Gosselin et al., 2020). In Cascadia, this type of fault-valve process is observed to coincide with the tip of the MWC (Gosselin et al., 2020). Furthermore, subduction shear zones show strong seismic anisotropy, which has been interpreted as foliated mylonites that channel migration of fluids released down dip of the MWC to lower pressure regions up dip (along the foliation plane) where SSEs are observed (Kawano et al., 2011; Song and Kim, 2012; Okazaki et al., 2013; Hyndman et al., 2015). The suppression of vertical fluid flow (i.e., orthogonal to foliation) means that elevated pore fluid pressures can be sustained, and fluids can be sourced from deeper metamorphic reactions (e.g., Angiboust et al., 2014). Under this model, in situ fluid production may not necessarily coincide spatially with the SSE source region.

In addition to slab-derived fluid effects, the geological makeup of the CSZ may play a role in controlling the episodicity of SSEs. More specifically, SSE behavior is generally segmented into three broad, 300-500 km-long regions along the subduction zone, which broadly coincide spatially with a different overriding plate geology with the Wrangellia, Siletzia, and Klamath terranes located from north to south. This correlation has led to the hypothesis that the rheology and composition of the upper plate controls slow slip patterns on the megathrust (Brudzinski and Allen, 2007). However, the effect of upper plate rheology is difficult to quantify and directly correlate with SSE, and will not be considered further.

3.2 METHODS

3.2.1 THERMAL MODELLING

We determine the thermal structure of 10 trench-normal profiles of the Cascadia subduction zone using the steady state, two-dimensional, finite-element numerical modelling code PGCtherm2D as described by Wang et al. (1995) which has been used in several thermal modelling studies (e.g., Currie et al. 2004, Wada and Wang, 2009). The main parameters that influence the thermal structure of a subduction zone include the subducting plate geometry, the oceanic plate age, the convergence rate, and the thickness of incoming sediments. In general, increasing the plate age and the convergence rate decreases slab temperatures at a given depth, whereas increasing the subducting plate dip and thickness of incoming sediments increases temperatures. Here we use a plate age model based on the marine magnetic anomalies described by Wilson (1993). The convergence rate is determined by calculating the trench normal component of plate motion based on the model described by Angus et al. (2011). Sediment thickness is estimated based on seismic refraction data by Trehu et al. (1994) and Flueh et al. (1998), as summarized by Wang and Trehu (2016). Finally, subducting plate geometry is from McCrory et al. (2012). The parameters assigned for each profile are summarized in Table 3.1. Other parameters that must be assigned include the radioactive heat generation and the thermal conductivity of each rock unit, as well as the amount of frictional heating along the subducting interface, as discussed below.

The continental and oceanic boundary conditions (i.e., geotherms) are constrained by backarc heat flow and subducting plate age, respectively. The oceanic geotherm is calculated using the GDH1 plate cooling model (Stein and Stein, 1992), modified to include the thermal effects of the thick incoming sediment layer (~3 km) observed for the CSZ. The continental geotherm is calculated assuming a backarc surface heat flow of 75 mW/m^2 at a distance of ~400 km from the trench based on the regional average for Cascadia (Currie and Hyndman, 2006). Upper and lower boundaries of the model have constant temperatures of 0 °C and 1450 °C respectively. We parameterize our model as four subdomains: the continental upper crust, the continental lower crust, the subducting oceanic lithosphere, and the continental mantle wedge. We follow Gao and Wang (2014)

TABLE 3.1: SUBDUCTING PROFILES PARAMETERS. [1]WILSON, 1993; [2]ANGUS ET AL, 2011; [3]WANG AND TREHU, 2016.

Longitude	Latitude	Age[1] (Ma)	Convergence Rate[2] (mm yr^{-1})	Sediment Thickness[3] (m)
234.92	41.14	7	33.57	2500
234.84	42.04	6.5	34.67	2500
234.76	42.94	7.5	35.76	3000
234.69	43.84	9	36.84	3200
234.61	44.73	9	37.94	3200
234.45	45.62	8	39.05	3200
234.16	46.50	7.5	40.20	2500
233.81	47.36	7.5	41.35	3000
233.33	48.19	6	42.49	3200
232.63	48.94	5.5	43.63	3500

and assign thermal conductivity values of 2.5 W m^{-1} K^{-1} for the continental crust, 3.1 W m^{-1} K^{-1} for the mantle and 2.9 W m^{-1} K^{-1} for the oceanic crust. Heat production values are assigned as 0.4 μW m^{-3} for the lower crust, and 0.02 μW m^{-3} for the oceanic lithosphere and mantle wedge. In the upper crust, the presence of accreted terranes along the Cascadia subduction zone lowers the expected heat production, which is associated with the presence of mafic materials in the forearc. Based on this, we assign a value of 0.2 μW m^{-3} throughout the upper continental forearc crust (Wang et al., 1995; Wada and Wang, 2009). The apparent coefficient of friction (μ) is set at 0.02 down to a depth of 20 km, as suggested by heat flow data (Gao and Wang, 2014).

We follow Wada and Wang (2009) and use a thin layer (100 m) of low-viscosity material along the slab interface, which results in a decoupling depth of 70 km (Wada and Wang, 2009). We assign rheological parameters of the mantle wedge based on wet olivine dislocation creep (Karato and Wu, 1993). There is currently uncertainty in the Moho depth of the overriding plate that defines the top of the MWC along the CSZ, due to the difficulty in resolving the low impedance contrast expected between the hydrated mantle wedge and overriding crust using seismic data (Bostock et al., 2002; Brocher et al., 2003). We follow McCrory et al. (2014) and assign the top of the forearc mantle wedge depth at ~37 km depth along the Vancouver Island, northern California, and Oregon profiles, and ~42 km along the Washington profiles.

3.2.2 HYDROTHERMAL CIRCULATION

Hydrothermal circulation is commonly incorporated in thermal models of subduction zones to account for heat advected by moving water found in the subducting slab crustal aquifer (Davis, 1997; Rosas et al., 2016; Spinelli et al., 2018). The result of the transfer of heat up dip within the subducting slab is to create anomalously high temperatures closer to the trench and cooler temperatures landward of the trench. The presence of vigorous hydrothermal circulation in Cascadia is still in question. Heat flow data at the trench can currently be explained without introducing the effects of hydrothermal circulation, therefore the effects of this process on the thermal structure of the CSZ is still unknown (Wang and Trehu, 2016)

In the models shown below, hydrothermal circulation is not included. However, to assess its effect on the thermal structure of the subducting plate, we compare the results of a single profile (profile 9) modeled with and without hydrothermal circulation. The proper inclusion of this effect requires the full modeling of thermal convection in permeable media, which can be computationally expensive. Since we are more interested in the thermal effects of hydrothermal circulation, we follow the methodology of previously published works (Harris et al. 2010; Rosas et al. 2016; Spinelli et al. 2018) and use a conductive proxy for the aquifer based on the Nusselt Number (Davis et al., 1997), *Nu*, which is empirically related to the Rayleigh number

$$Ra = \frac{\alpha g k L^2 \rho_f q}{\mu \kappa K}, \qquad \textit{Eq. 3.1}$$

as

$$Nu = 0.08 Ra^{0.89}, \qquad \textit{Eq. 3.2}$$

where α is the thermal expansivity, g is the gravitational acceleration, k is the permeability, L is the aquifer thickness, ρ_f is the fluid density, q is the heat flux into the base of the aquifer, μ is the fluid viscosity, κ is the thermal diffusivity, and K is the thermal conductivity of the basement rock. A conductivity proxy can then be defined as:

$$\lambda' = \lambda Nu, \qquad \textit{Eq. 3.3}$$

where λ=2.9 W m^{-1} K^{-1} is the original thermal conductivity of the aquifer (Davis et al., 1997). In our model with hydrothermal circulation, we add a 500 m sediment and 500 m aquifer layer to the top of the subducting slab and use the proxy conductivity, which is determined by fitting the calculated heat flow to measured heat flow data.

3.2.3 FLUID FLUX CALCULATION

We follow a similar procedure to that outlined in Spinelli et al. (2018) and Wada et al. (2012) to determine the total fluid expulsion rate from the slab, as a function of distance from the trench along each profile (Fig. 3.2). This approach is based on calculating equilibrium mineral assemblages and their corresponding fluid content from petrologic and thermodynamic modeling (Hacker, 2008), which allows for the calculation of fluid

release along a P-T path (Guiraud et al., 2001). Fluid content for the representative lithologies in the slab were calculated with Perple_X (Connolly, 2009) using the 2004 version of Holland and Powell (1998) thermodynamic database assuming maximum hydration and fluid saturation for all lithologies. The subducting slab (Fig. 3.2) is composed of a 500 m-thick section of under-thrusting sediment, 2 km of mid-ocean ridge basalt (MORB), and 5 km of gabbro. A peridotite layer is not included as significant dewatering is not predicted for the shallow depths considered here (< 100 km; Wada et al., 2012). Initial bulk compositions of each lithology are listed in Table 3.2. We divide the subducting slab into 500 x 500 m cells where pressure-temperature (P-T) conditions are extracted at each node of the thermal model (Fig. 3.2). The Perplex calculation was done at a low resolution to match the cell size used in the thermal models. Pressure is calculated using the bulk density of the overlying lithologies and the depth to each node. Water content at each node is determined by the phase diagrams for the corresponding lithology calculated at saturation. This procedure has been widely applied to determine fluid expulsion rates at subduction zones (e.g. Hacker, 2008; Peacock, 2009; van Keken et al., 2011; Wada et al., 2012; Rosas et al., 2016; Perry et al., 2016; Spinelli et al., 2018; Peacock, 2020), and is justified by our need for the petrological model to be compatible with the thermal models, and mathematically simple enough to be implemented.

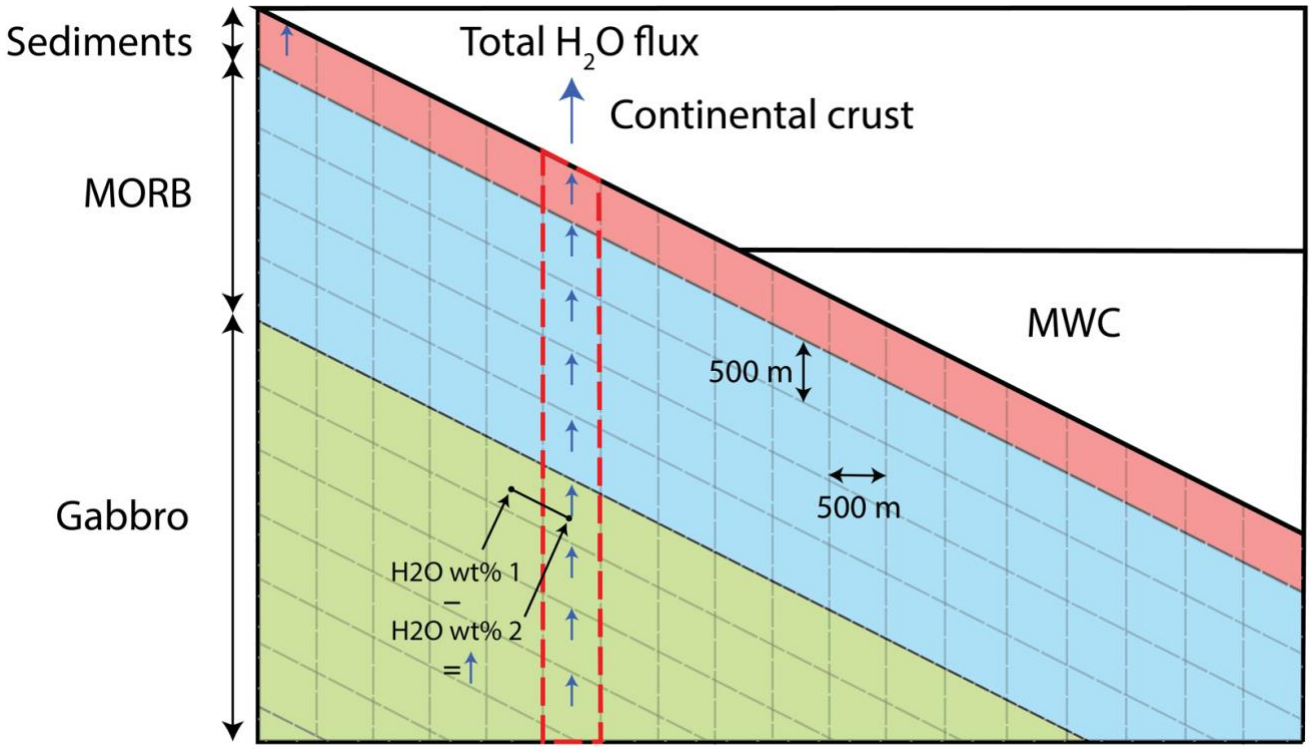

FIGURE 3.2: SCHEMATIC DIAGRAM (NOT TO SCALE) SHOWING HOW TOTAL H2O FLUX IS DETERMINED. H2O WT% IS CALCULATED FOR EACH CELL BASED ON THE MODELLED P-T CONDITIONS. IF THERE IS A DECREASE IN H2O WT% FROM ONE CELL TO THE NEXT WITHIN A GIVEN LAYER THE TOTAL EXPULSION OF H2O IS ASSUMED BASED ON THE DIFFERENCE IN WATER CONTENT BETWEEN THE TWO CELLS. THE TOTAL FLUX IS CALCULATED AS A SUM OF TOTAL H2O RELEASE FROM EACH LAYER AT A SPECIFIC TRENCH DISTANCE.

TABLE 3.2: COMPOSITION OF MATERIAL USED FOR PETROLOGICAL MODELLING. (SPINELLI, 2018)

Material	SiO_2	TiO_2	Al_2O_3	FeO	MgO	CaO	Na_2O	K_2O	H_2O at saturation	CO_2	reference
Sediment	57.9	0.8	15.4	6	3	2.4	2.9	2.4	9.2	0	Plank and Langmuir, 1998; van Keken et al., 2011
MORB	50.6	1.5	15.7	10.6	7.6	11.1	2.6	0.2	5.3	0	Pearce, 1976; Wilson, 1989; Hacker, 2008
Gabbro	50.6	0.9	16.1	6.2	9.2	12.5	2.8	0.1	5.2	0	Dick et al., 2000; Hacker, 2008

In our fluid flux estimation, we consider initial water contents of 9.2 wt% for the sediments, 4 wt% for basalt, and 1.1 wt% for gabbro. The results shown in Fig. 3.5 assume maximum hydration and fluid saturation, which allows for greater H_2O wt % content than these initial values. To account for this, our fluid flux calculations only allow water to be released once the calculated water content of a cell becomes less than the assigned initial value for each lithology (Fig. 3.5, contours) (van Keken et al., 2011). The change in water content is calculated considering only positive water loss with no H_2O ingestion. We implement this by assigning a new minimum of H_2O wt% once a cell experiences a decrease in water content (van Keken et al., 2011). H_2O is assumed to be completely expelled once the slab traverses the entire cell. We further assume instantaneous migration of liberated fluid from the site of the dehydration to the slab surface, effectively ignoring any fluid kinematics. The convergence rate controls the rate of fluid expulsion by setting the time needed for the slab to traverse an entire cell. The total flux is then calculated as the sum of the calculated H_2O released at each node in each column (Fig. 3.2).

3.3 RESULTS

3.3.1 THERMAL MODELS

Fig. 3.3 shows the resulting thermal models for each profile without including the effects of hydrothermal circulation. Table 3.3 presents the modelled slab temperature at the MWC for all profiles. We can observe significant contrast in estimated MWC temperatures varying from 400-500°C in the central region up to 500-600°C in the north. This increase in temperature can be attributed to the lower plate age and increased sediment cover along the northern profiles. Secondary influences include the lower dip of the subducting slab from south to north. Along the Washington coastline, Moho depth is estimated at ~42 km, which is deeper than what is observed along northern California, Oregon, and Vancouver Island (McCrory, 2014), and this further affects the temperature estimates at the MWC.

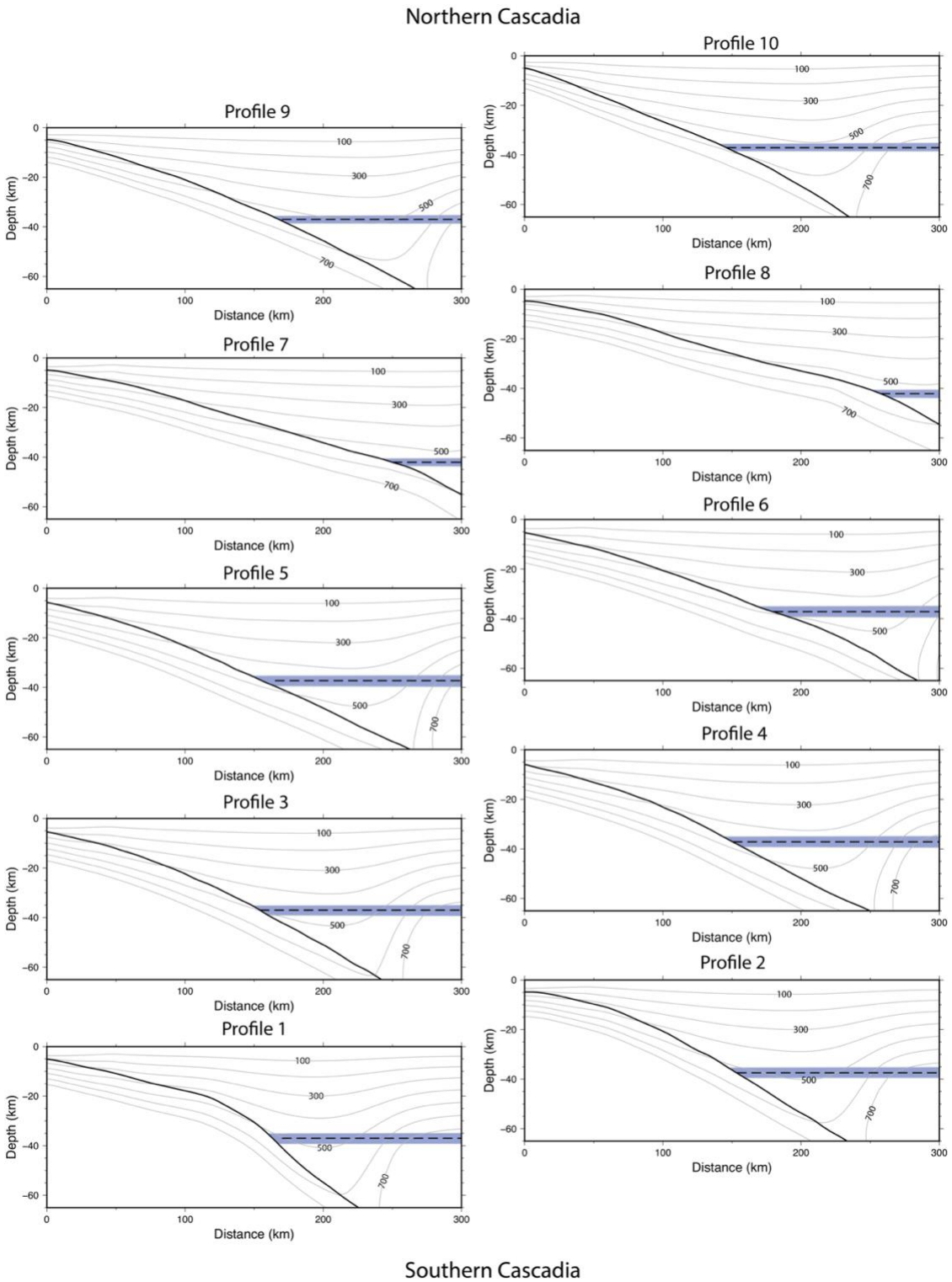

FIGURE 3.3: THERMAL MODELS SHOWING TEMPERATURE CONTOURS EVERY 100°C AND THE GEOMETRY OF THE SUBDUCTING SLAB (THICK BLACK LINE) FOR EACH PROFILE. THE DASHED HORIZONTAL LINE SHOWS THE ESTIMATED MOHO WITH ERRORS IN DEPTH REPRESENTED BY BLUE REGION BASED ON RESULTS FROM MCCRORY ET AL. (2014)

TABLE 3.3: MODELLED TEMPERATURES AT MWC FOR EACH OF THE 10 PROFILES.

Segment	Temperature at MWC (°C)
1	~520
2	~520
3	~500
4	~475
5	~475
6	~500
7	~550
8	~540
9	~550
10	~580

Slab temperatures around the SSE source region can be similarly compared between profiles. We use tectonic tremor (Wech and Creager, 2008) as a proxy for SSE source region and compare tremor distribution with slab temperatures and location of the MWC. In all cases, the number of tremor events peak at, and just up dip of, the MWC, where temperatures range between ~475°C to ~550°C. In northern California, SSE occurrence peaks at ~525°C, in central Oregon at ~475°C, and in Vancouver Island at ~550°C. In addition, the observed spatial patterns in slab temperatures in the SSE source region are broadly consistent with the segmentation of SSE recurrence times. We observe a transition from high to low and back to high temperatures from south to north, which corresponds with the transition from short to long and back to short recurrence times. However, there is no direct linear relationship between slab temperature and SSE recurrence time at this scale, as we observe higher temperatures in Vancouver Island compared to northern California but shorter recurrence times in the latter. This provides further evidence that there is no specific slab temperature required for SSE occurrence (Peacock, 2009); instead, temperature may play an indirect role, combined with other physical factors, to create the necessary conditions for SSE (e.g., McLellan and Audet, 2020).

Finally, Fig. 3.4 shows the resulting thermal model for profile 9 including the effects of hydrothermal circulation. We incorporate these results to demonstrate the effects on subducting profile temperatures in a single case. Hydrothermal circulation acts to increase temperatures near the trench and decrease temperatures near the MWC. MWC temperatures are decreased by ~50°C as compared to the case in which hydrothermal circulation is not included. Figure 3.4c shows the heat flow profile for the model that includes and excludes the effects of hydrothermal circulation. With hydrothermal circulation, we observe suppressed heat flow as the high conductivity reservoir transfers heat up dip from the MWC.

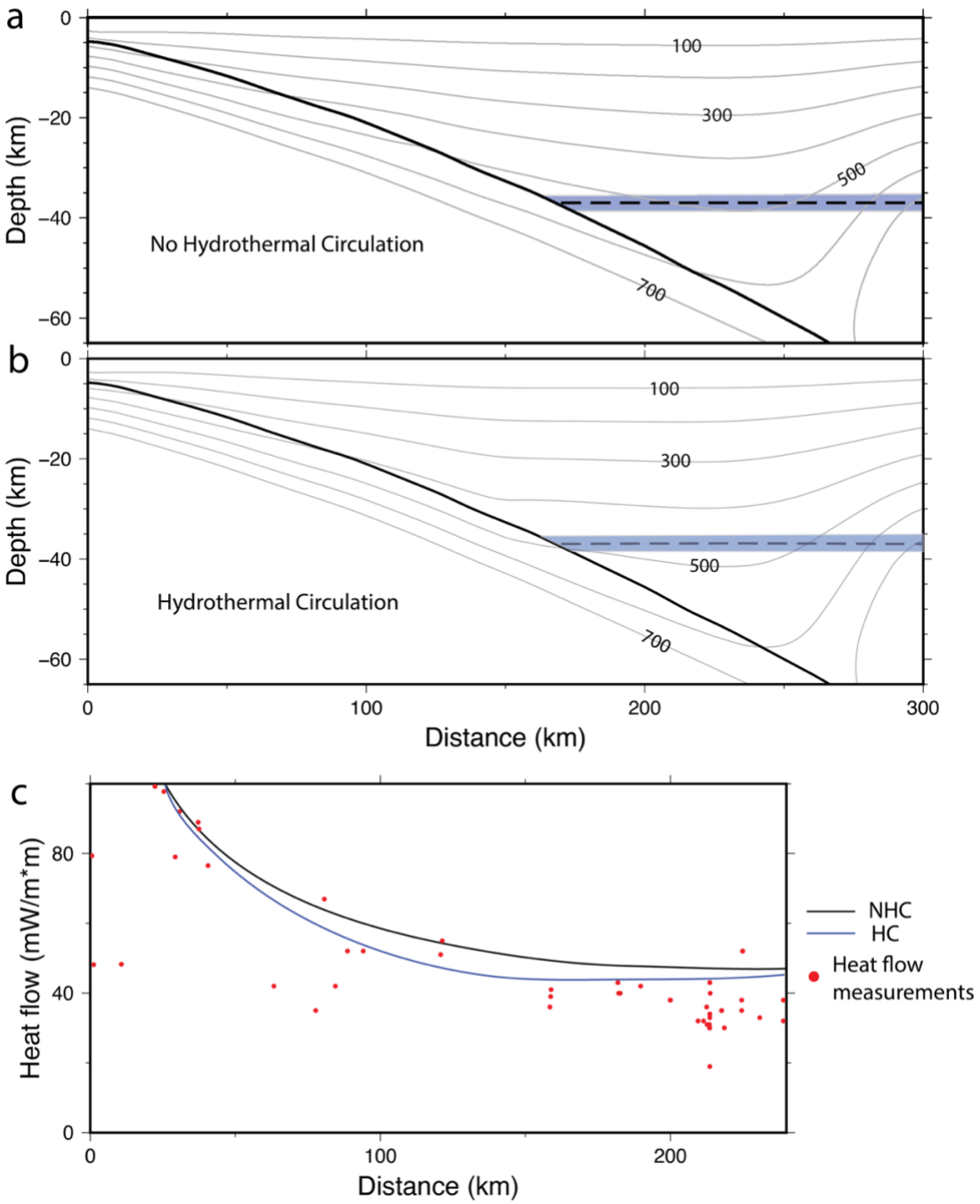

FIGURE 3.4: COMPARISON OF THERMAL MODELS FOR PROFILE 9 THAT (A) DO NOT INCLUDE AND (B) DO INCLUDE THE EFFECTS OF HYDROTHERMAL CIRCULATION. (C) CALCULATED HEAT FLOW FOR PROFILE 9 LOCATED IN SOUTHERN VANCOUVER ISLAND PLOTTED WITH MEASURED HEAT FLOW DATA. (LEWIS ET AL., 1988; DAVIS ET AL., 1990; HYNDMAN ET AL., 1993) MODELLED HEAT FLOW WITHOUT THE EFFECTS OF HYDROTHERMAL CIRCULATION (NHC) IS SHOWN IN BLACK WHILE THE MODELLED HEAT FLOW WITH THE EFFECTS OF HYDROTHERMAL CIRCULATION (HC) IS SHOWN IN BLUE. HYDROTHERMAL CIRCULATION IS SHOWN TO SUPRESS HEAT FLOW AS VIGOROUS CIRCULATION TRANSFER HEAT FROM THE MWC UP DIP TOWARDS THE TRENCH. CORRESPONDING THERMAL MODELS ARE SHOWN ABOVE FOR REFERENCE.

3.3.2 FLUID FLUX

Based on the pattern of fluid release, we separate the profiles into three regions: the southern region (profiles 1-3), central region (profiles 4-6), and northern region (profiles 7-10). Fig. 3.5 shows the calculated fluid abundance for the three lithologies and the P-T paths for three representative profiles (one for each of the three regions described here). These three distinct P-T paths lead to different sites of dewatering (i.e., decrease in H_2O content) within the slab, as new facies are reached at different P-T conditions (Fig. 3.6). Most notably, the central Cascadia profile reaches epidote-amphibolite facies assemblages at greater pressures (greater depths) than the northern and southern cases.

Fig. 3.7 shows the resulting H_2O flux calculated for three representative profiles, along with the distribution of tremor events as a function of distance from the trench. The remaining profiles are shown in the supplementary material (Fig. S3.1). We observe significant variability in fluid flux profiles along the CSZ with a different pattern observed for each profile. The southern profile (Fig. 3.7a) shows two main sites of high fluid flux. The first is located up to 50 km from the trench and is largely a result of dewatering of the sediment layer (at temperatures of ~295-360°C and pressures of ~0.19-0.28 GPa) and MORB layer (at temperatures of ~310-400°C and pressures of 0.2-0.35 GPa) (Figs. 3.5-7). The latter is associated with the transition of the MORB to the greenschist facies where a significant decrease in H_2O content is predicted (Hacker et al., 2003). A second site is observed just down dip of the MWC, occurring between a trench-normal distance of 175 and 250 km. From 175-200 km, the majority of the initial H_2O comes from the dehydration of the MORB layer, where temperatures and pressures are ~550-600°C and 1.3-17 GPa, At the onset of dewatering near the MWC, the P-T conditions are characterized by amphibolite facies assemblages (Fig. 3.6) with water contents of 2-3 wt%. The remaining water is released at the site of eclogitization, which occurs at P-T conditions of 2 GPa at 500°C to 1.5 GPa at 700°C (Fig. 3.6). This corresponds with a trench distance of 200-225 km (Fig. 3.7) which explains the continued dewatering at these distances. The dewatering of the gabbro layer begins to contribute to the total flux at conditions associated with eclogite facies assemblages where H_2O wt% drops below 1.1%. This occurs between 200 and 250 km at P-T conditions of 1.7 GPa and 600°C and 2.4 and 710 °C.

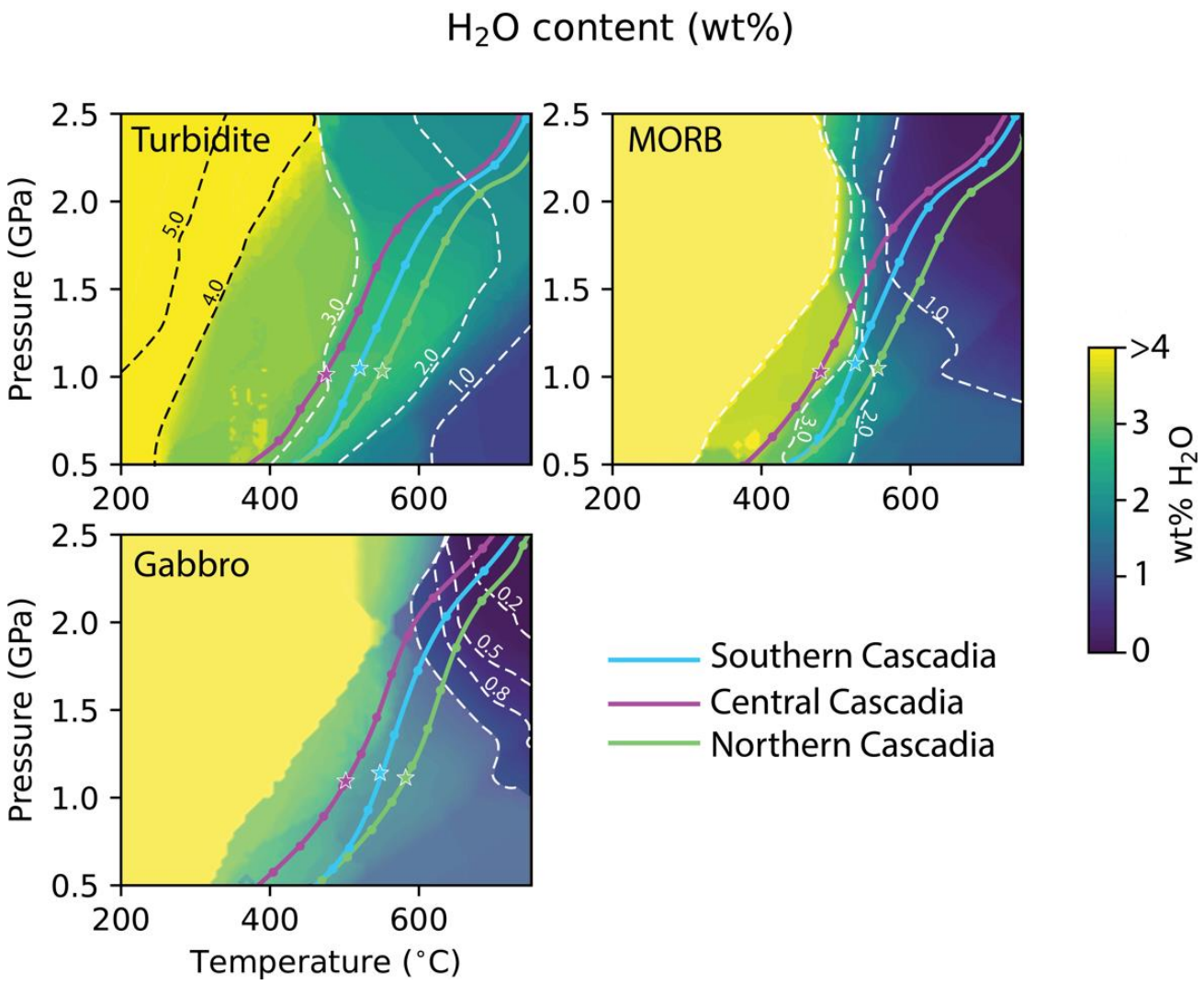

FIGURE 3.5: H2O CONTENT FOR THE THREE LITHOLOGIES IN THE SLAB CALCULATED AT SATURATION. WE APPLIED A SEMI-TRANSPARENT MASK FOR VALUES GREATER THAN THE PRESCRIBED INITIAL H2O CONTENT FOR EACH LITHOLOGY (9.2 WT% FOR TURBIDITE, 4 WT% FOR MORB, AND 1.1 WT% FOR GABBRO). WHITE DASHED LINES SHOW H2O CONTOURS USED IN THE FLUID FLUX CALCULATIONS. P-T PATHS ARE SHOWN FOR THE THREE REPRESENTATIVE PROFILES. EACH PT PATH IS CALCULATED FOR THE TOP INTERFACE OF EACH LITHOLOGY. A DECREASE IN H2O WT% IS OBSERVED WHEN MINERALOGICALLY BOUND FLUID IS RELEASED DURING PROGRADE METAMORPHIC REACTIONS. DATA ARE FROM SPINELLI ET AL. (2018).

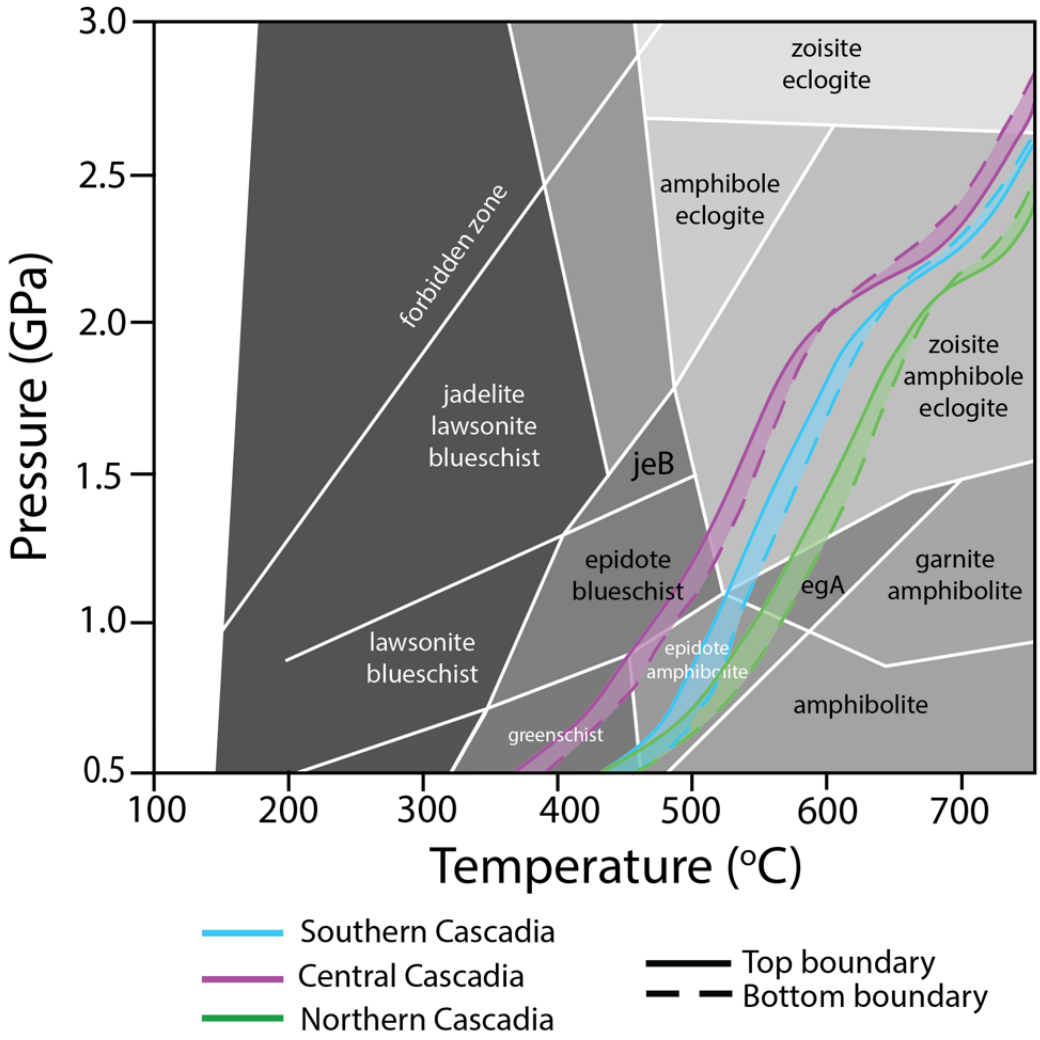

FIGURE 3.6: PHASE DIAGRAM FOR MORB (HACKER, 2003) WITH P-T PATHS FOR SOUTHERN, CENTRAL, AND NORTHERN CASCADIA. SOLID LINE INDICATES P-T CONDITIONS AT THE TOP OF MORB LAYER WHILE DASHED LINE REPRESENTS P-T CONDITIONS AT THE BOTTOM OF MORB LAYER.

In central Cascadia (Fig. 3.7b), we similarly see early dewatering of the sediment and MORB layers at trench distances of up to 50 km. In the sediment layer this corresponds to P-T conditions of ~270°C and ~0.2-0.3 GPa. In the MORB layer the P-T conditions (~0.2-0.4 and ~280-360°C) are again consistent with greenschist facies assemblages. In comparison with the southern profile, the second major site of dewatering occurs further down dip of the MWC (in comparison with the southern profile), at distances between 200 and 300 km from the trench, where P-T conditions range from ~520-690°C and ~1.4-2.4 GPa. The delayed instance of bulk dewatering in this case is a result of the lower temperatures modelled in central Cascadia. In northern Cascadia (Fig. 3.7c), we again see a shift in the pattern of dewatering, with bulk decrease in H_2O of the MORB layer at the location of the MWC, similar to what is observed in southern Cascadia. The MORB layer continues to expel water at trench distances of ~175-275 km corresponding to P-T conditions of 560-680°C and 1.1-2.1 GPa associated with the transition to amphibolite and then eclogite facies mineral assemblages (Fig. 3.6). In both the southern and northern Cascadia cases, early dewatering of the MORB layer occurs due to higher subducting slab temperatures. We again see a greater fluid flux closer to the MWC with significant dewatering of the MORB layer within 25 km of its location. In the case that includes hydrothermal circulation (Fig. 3.7c), the resulting change in the subduction zone thermal profile has modest effects on the resulting fluid flux profiles. Early dewatering of the MORB and sediment layers occurs primarily before the 50 km distance, as in the case with no hydrothermal circulation. Small differences are observed at the location of the MWC where we observe increased H_2O loss within the MORB layer near the MWC. The gabbro layer exhibits delayed peak dewatering, with highest levels reached at a distance greater than 250 km from the trench. This contrasts with a peak at ~230 km in the case with no hydrothermal circulation. The total flux profile highlights the differences with a greater proportion of water release past 250 km from the trench. The calculated total flux values at each distance from the MWC (Table 3.4) shows a modest increase in fluid flux with the inclusion of hydrothermal circulation. The difference is most pronounced further down dip of the MWC due to delayed dewatering.

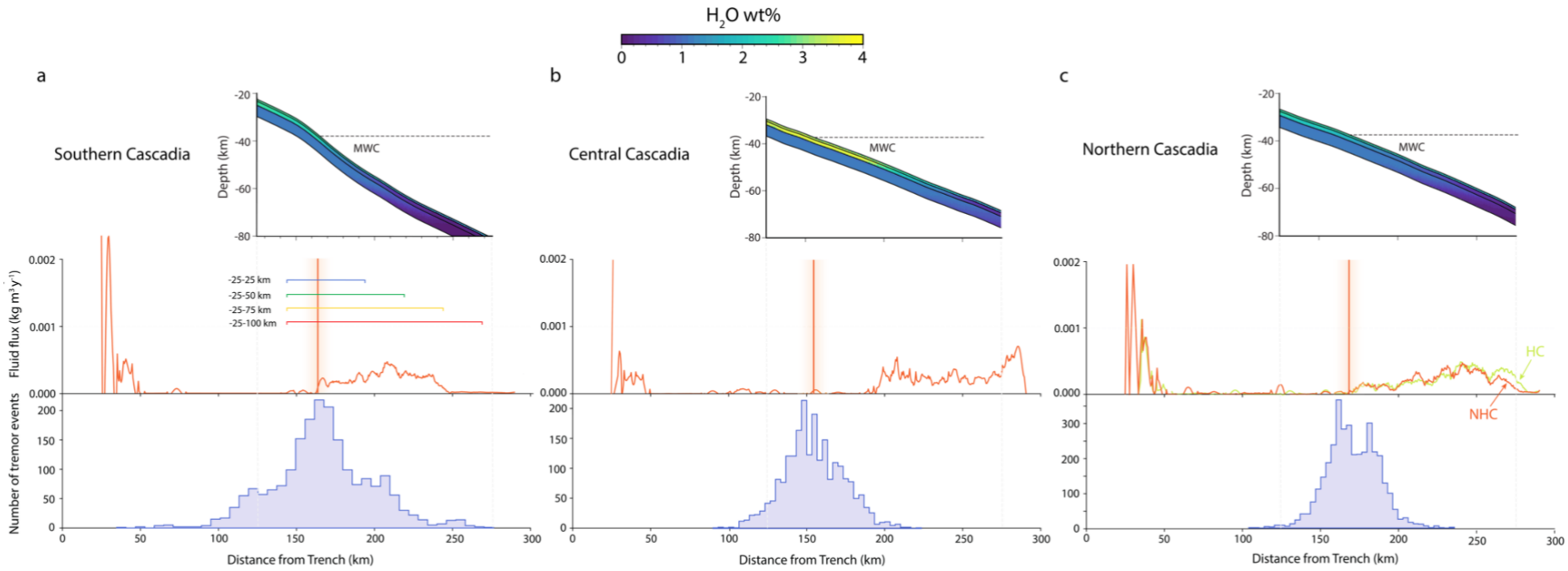

FIGURE 3.7: MODELLED H2O WT% WITHIN THE SEDIMENT, MORB, AND GABBRO LITHOLOGIES RESPECTIVELY (TOP), CALCULATED FLUID FLUX (MIDDLE) AND TREMOR DISTRIBUTION (BOTTOM) FOR THE THREE REPRESENTATIVE PROFILES: A) SOUTHERN (PROFILE 1), B) CENTRAL (PROFILE 5), AND C) NORTHERN CASCADIA (PROFILE 9; NHC AND HC CASE). FLUX RATE IS CALCULATED AS A SUM OF THE THREE LITHOLOGIES AT EACH DISTANCE SMOOTHED USING A WINDOW OF 20 KM. ESTIMATED LOCATION OF THE MWC IS SHOWN BY VERTICAL ORANGE LINE WITH ERROR BOUNDS ON EITHER SIDE. THE TREMOR DISTRIBUTION IS SHOWN TREMOR COUNTS OVER A GIVEN YEAR. THE COLORED BARS IN THE MIDDLE PANEL OF A) SHOWS THE FOUR DISTANCE RANGES OVER WHICH TOTAL FLUID FLUX IS CALCULATED AND SHOWN IN FIGURE 2.2.8.

TABLE 3.4: TOTAL FLUX RATE KG·M-3·Y-1CALCULATED WITHIN ALONG-PROFILES DISTANCE DOWNDIP OF THE MWC. AVERAGE VALUES ARE CALCULATED BASED ON THE 3 REGIONS DESCRIBED IN TEST. PROFILE 9 SHOWS RESULTS OF THE HC AND NO HC CASES. HIGHLIGHTED DATA ARE REMOVED FROM

Segment	H2O -25-25 km	H2O -25-50 km	H2O -25-75 km	H2O -25-100 km
1	8.40E-03	2.42E-02	3.78E-02	4.02E-02
2	4.08E-03	1.32E-02	3.06E-02	3.98E-02
3	2.34E-03	8.77E-03	2.12E-02	3.54E-02
AVG.	**4.94E-03**	**1.54E-02**	**2.99E-02**	**3.85E-02**
4	6.82E-04	8.77E-03	2.12E-02	3.23E-02
5	5.87E-04	4.85E-03	1.90E-02	3.00E-02
6	4.08E-04	2.37E-03	6.73E-03	2.21E-02
AVG.	**5.59E-04**	**5.33E-03**	**1.56E-02**	**2.81E-02**
7	4.15E-03	8.50E-03	8.50E-03	8.50E-03
8	4.21E-03	6.28E-03	6.28E-03	6.28E-03
9	5.50E-03	1.45E-02	3.06E-02	4.42E-02
10	6.27E-03	2.08E-02	3.86E-02	4.50E-02
AVG.	**5.03E-03**	**1.46E-02**	**3.46E-02**	**4.46E-02**
9 HC	5.16E-03	1.32E-02	2.78E-02	4.52E-02

We estimate the total amount of H_2O released at the base of the MWC as a function of distance relative to its vertex, encompassing ranges of -25 km up dip to 25, 50, 75 and 100 km down dip (Fig. 3.8). The four distance ranges are visually displayed in Fig. 3.7a (left panel). The largest fluid release is observed in the southern and northern regions at all ranges, where there is an approximate three-fold difference between that observed in the northern and southern regions compared to that in the central region. Fig. 3.7 (top panels) shows the H_2O wt% of the three lithologies based on the P-T conditions that highlights these differences. The representative central Cascadia profile (Fig. 3.7b) shows a transition to lower water content at higher pressures, and therefore greater depths, moving major sites of dewatering further down dip of the MWC. Finally, we observe a correlation between shorter SSE recurrence times and increased tremor activity with the maximum fluid flux calculated in each region, for the distance ranges -25-25 and -25-50 km from the MWC (Fig. 3.8).

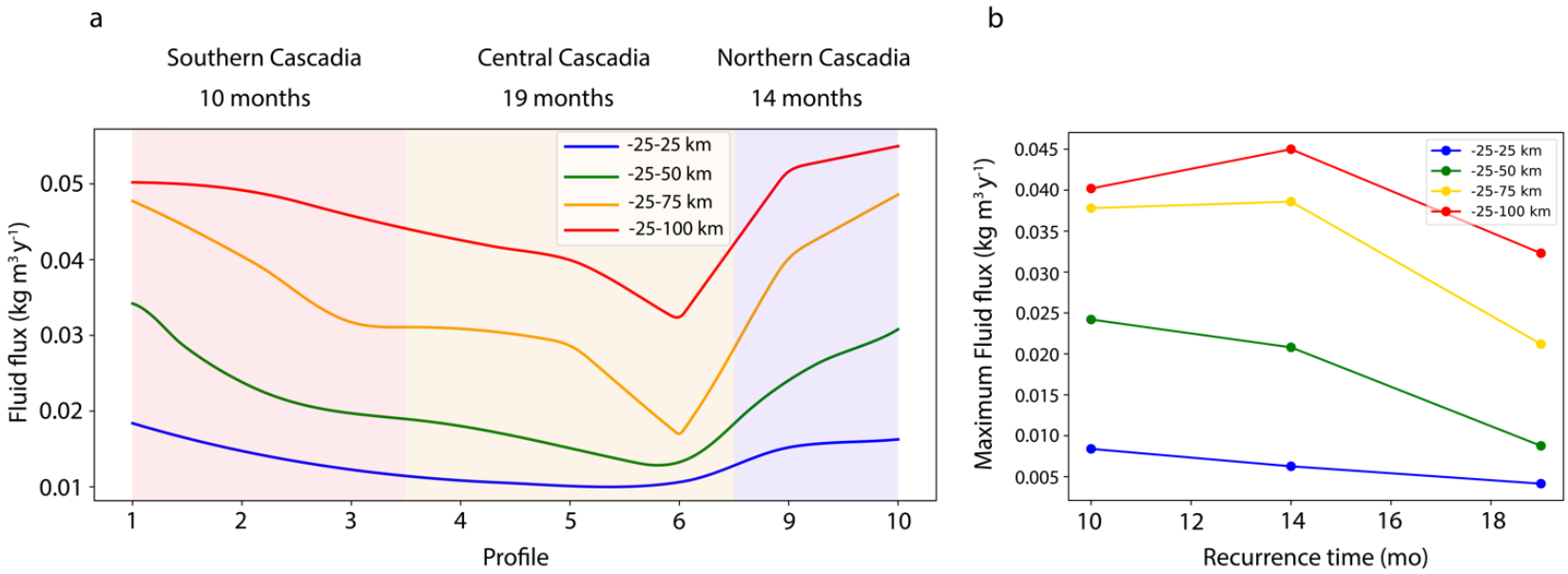

FIG. 3.8 (A): ALONG-STRIKE VARIATION IN TOTAL FLUID FLUX CALCULATED WITHIN 25 KM (BLUE), 50 KM (GREEN), 75 (KM) ORANGE, AND 100 KM (RED) DOWN DIP OF THE MWC. SHADED AREAS REPRESENT THE THREE REGIONS USED TO CALCULATE AVERAGE FLUX VALUES IN TABLE 3.4. RED AREA CORRESPONDS TO NORTHERN CALIFORNIA TO SOUTH-CENTRAL OREGON, ORANGE AREA CORRESPONDS TO CENTRAL OREGON TO CENTRAL WASHINGTON, AND BLUE AREA CORRESPONDS TO VANCOUVER ISLAND. PROFILES 7 AND 8 ARE EXCLUDED HERE AS THE DISTANCES USED TO CALCULATE THE TOTAL FLUX RATE EXCEED MODEL BOUNDS. (B): MAXIMUM FLUID FLUX FOR EACH REGION PLOTTED AGAINST THE ESTIMATED RECURRENCE INTERVAL.

3.4 DISCUSSION

3.4.1 INFLUENCE OF SUBDUCTION ZONE SEGMENT CHARACTERISTICS

Our results suggest that relatively small changes in subduction zone parameters (e.g., subduction zone geometry, subducting plate age, convergence rate, and sediment thickness) can have a significant influence on the thermal structure and therefore the pattern of fluid release along a given subduction zone. To first order, these parameters appear to be relatively uniform in Cascadia with little along-strike variations. However, the combination of these parameters varies along strike with enough magnitude to alter the observed pattern of fluid release.

Subduction zone temperatures are largely controlled by the age of the incoming subducting plate, with secondary influences from the amount of insulating sediment as well as the convergence rate. In the case of the southern and northern Cascadia, temperatures are high enough (Table 3.3) to reach dehydration reactions which include the transition to epidote-amphibolite facies assemblages where water content is decreased to 2-3 wt% at the location of the MWC. In central Cascadia, temperatures are lower at the MWC and this dehydration is reached farther down dip. Overall, the young subducting plate ages present in southern Cascadia (~7 Ma) and northern Cascadia (~6 Ma) reach higher temperatures at the MWC in comparison to those in central Cascadia where subducting plate ages are in the range of 8-9 Ma. The higher temperatures found here change the P-T path of the subducting slab enough to alter the location of major sites of dewatering. In the case of different dewatering patterns in southern and northern Cascadia, a more steeply dipping subducting plate may contribute to earlier loss of mineral bound H_2O as P-T conditions increase more rapidly. This could explain greater amounts of fluid expulsion near the location of the MWC.

The location of the MWC, as determined by the continental Moho depth and subducting plate dip, may also affect P-T paths by changing the average thermal conductivity of the upper plate. which affects the heat flux. There is significant uncertainty in the position of the MWC due to continental Moho depth uncertainty along the CSZ (McCrory et al. 2014; Audet et al. 2010), but current estimates suggest a deeper Moho in

Washington (~42 km) compared to Vancouver Island and Oregon (~37 km). Considering constant heat flux, the deeper Moho in central Cascadia lowers the thermal conductivity across a longer segment of subducting slab, and therefore leads to greater plate interface temperatures. However, this effect is largely offset by the greater slab age (and therefore cooler incoming slab) in central Cascadia, whose effect dominates the temperature field (Fig. 3.3). Steeper P-T paths in central Cascadia imply lower-temperature and higher-pressure conditions within the mantle wedge itself, which could place constraints on the degree of serpentinization, as inferred from seismic data (e.g., Bostock et al., 2002; Brocher et al., 2003). However, to properly account for this effect, the metamorphic and hydrous conditions within the mantle wedge would need to be considered.

3.4.2 FLUID FLUX

We generally observe that mean tremor density coincides with the location of the MWC, whereas fluid generation through metamorphic dehydration reactions occurs down dip of the MWC. This observation appears to be more consistent with the fluid mobilization model controlling SSE (e.g., Hyndman et al., 2015), in contrast to in situ fluid production (e.g., Fagereng and Diener, 2011; Condit et al., 2020). Assuming that: 1) our thermal-petrologic models are accurate; and 2) fluid processes do control SSEs near the MWC presumably through high pore-fluid pressure (e.g., Audet et al., 2009), it becomes relevant to examine the migration behavior of H_2O towards and within the SSE source region.

Locally, fluid production is accompanied by a decrease in solid volume, creating a transient fracture network and high permeability pathway for fluid flow (e.g., Tenthorey and Cox, 2003; Savard et al., 2018; Calvert et al., 2020). A vertical pressure gradient will move this fluid upward through the slab until it reaches a low permeability barrier, where it will likely accumulate or travel up dip along the barrier. Below the MWC, a low-permeability barrier likely results from serpentinization of peridotitic mantle wedge, which consumes fluids and results in a volume expansion (Connolly, 1997). The degree of serpentinization may therefore be another factor that controls SSE occurrence, since the amount of fluid consumed by serpentinization determines how much free fluid is left and can accumulate and increase pore fluid pressures. However, according to Brocher et al.

(2003), serpentinization is observed along the entirety of the Cascadia margin as anomalously low upper mantle velocities and weak wide-angle reflections from the top of the upper mantle. This implies that much of the fluid released along the subducting slab is readily available to accumulate in pore space. Laboratory studies show that the permeability of antigorite serpentinite is low (Katayama et al., 2012) and that higher permeability should be observed parallel to relatively high shear stresses, (i.e., parallel to the plate dip; Hacker et al. (2003)), thus potentially channeling fluid migration up dip. The depth from which this mechanism can transport fluids up to the location of SSE occurrence is unknown, but there exists some evidence of up-dip fluid flow on the distance scales discussed here. Angiboust et al. (2014) use major and trace element data to show the potential movement of fluids 20-30 km up dip of the source, in this case from down dip metasomatized eclogites in the western Alps.

The cyclic nature of SSEs can be a result of the time needed to accumulate strain after the stress drop associated with an SSE event and/or because of pore-fluid pressure build up after precipitation resealing of the fractured impermeable interface (Audet and Bürgmann, 2014; Frank et al., 2015). In the latter case (i.e., the fault-valve model), the recurrence time would be directly dependent on the rate at which the fluid can be replenished (e.g., Farge et al., 2021). The inverse relationship between total flux rate and recurrence time supports the hypothesis that the rate of pore-fluid pressure build-up after an event is the main driver of SSE recurrence time, as suggested by seismic data (Warren-Smith et al., 2019; Gosselin et al., 2020). This inverse relationship is most pronounced when limiting the inclusion of fluid production to ~50-60 km landward of the MWC. This mechanism may be plausible if this depth is the limit to which free fluid is incorporated into the pore spaces where SSEs are observed. Geological observations provide consistent evidence for the fault-valve model through: 1) the recording of low-angle thrust faulting at low shear strength and near-lithostatic pore fluid pressures with complete healing of cracks occurring over similar time intervals of SSE recurrence (Ujiie et al., 2018); 2) isotopic signatures in hydrothermal veins consistent with the precipitation from metamorphic fluids (Fagereng et al., 2018); and 3) isotopic zoning in an eclogite-facies shear zone and inferred low permeabilities (Angiboust and Raimondo, 2022;

Hoover et al., 2022). These studies further connect metamorphic dehydration reactions to pore fluid pressure build up according to the fault-valve model.

Other variations in along-strike SSE behavior in Cascadia can also be explained by changing fluid flux. Tremor is shown to have increased density in the northern and southern most regions of the margin, which in turn is inversely correlated to seismic velocities in the lowermost forearc crust (Delph et al, 2018). This is consistent with increased presence of free fluids in the lower crust. In southern Cascadia, tremor is found to be most active but the highest energy rates are observed in northern Cascadia (Wech, 2021). In central Cascadia, tremor is weaker and less frequent. Fluid flux rates are found to be correlated with tremor activity but the relationship with energy rates is less clear as higher energy rates are observed in the north while fluid flux rates are lower than in the southern case. Wech (2021) suggests a possible trade-off between tremor energy rate and recurrence interval, which may reflect a change in fault strength.

3.5 CONCLUSION

Margin-wide variations in subduction zone parameters generate temperature and pressure conditions within the downgoing Juan de Fuca slab that combine to produce different fluid flux profiles along the Cascadia subduction zone. We observe three general patterns of fluid release where the main discriminating factor is the location of the bulk of basalt and gabbro dewatering with reference to the MWC. Based on this, we observe an inverse relationship between the total amount of fluid released within 50 km down dip of the MWC and the SSE recurrence time and tremor activity, with largest total fluid flux located in southern Cascadia (northern California), followed by northern Cascadia (Vancouver Island and northern Washington), and central Cascadia (Oregon). These differences are due to the increased temperatures observed at the MWC in the two prior cases. We incorporate the effects of hydrothermal circulation and show that it only produces modest changes in the flux profiles with a trend towards deeper dewatering. Overall, these results support models where different patterns of slab dewatering and mobilization influence the rate at which pore pressures increase and generate recurrent SSEs and contributes to the observed along-strike variations in Cascadia. Further

investigation is necessary to explore the role of varying free fluid pathways and transport mechanisms in controlling SSEs.

4

SERPENTINIZATION OF THE CASCADIA MANTLE WEDGE CORNER FROM RECEIVER FUNCTION MODELING AND ITS RELATION TO SLOW SLIP

Abstract

Slow slip events (SSEs) at subduction zones occur in a fluid-rich environment characterized by the interaction of the plate interface shear zone with the mantle wedge corner (MWC) of the overriding plate. In Cascadia, the MWC is thought to be serpentinized in the vicinity of the SSE source region; however, detailed constraints on the structural makeup of the MWC (e.g., geometry, percent serpentinization, fabrics, etc.), and its relationship with SSEs, are lacking. We conduct receiver function analysis for five stations in northern Cascadia to characterize the subduction zone structure and the presence of anisotropy in the MWC We first invert for the 1D shear-wave velocity (*Vs)* structure and identify the presence of a seismic low-velocity layer (LVL) marked by low *Vs* and high compressional-to-shear velocity ratio (*Vp/Vs* > 2) for each of the five stations used in the analysis. We then use the results of the 1D inversion to solve for isotropic and anisotropic parameters in the mantle wedge corner including layer thickness, percent anisotropy, and symmetry-axis orientation. We identify an ~10 km thick MWC beneath station SNB with Vs of 3.6 km/s and *Vp/Vs* values of ~1.8, which are consistent with the presence of 40-50% serpentinization. Anisotropy is characterized by a slow axis of hexagonal symmetry with a percent anisotropy of 14%. The orientation of the slow axis corresponds with sub-horizontal foliations, consistent with the presence of serpentinite being deformed by the downgoing slab. These results support heterogeneous serpentinization in the mantle wedge corner in Cascadia. Shear-induced foliated fabrics in serpentinites above the plate interface may play an important role in generating SSEs through channelling fluids up dip and aiding in the generation of fluid overpressures.

4.1 INTRODUCTION

The subduction of the Juan de Fuca plate along the west coast of North America produces the active tectonic margin known as the Cascadia Subduction Zone (CSZ). It is known to produce megathrust earthquakes (Hyndman and Wang, 1993), but overall exhibits low levels of seismicity and is a rare case of almost aseismic subduction (Bostock et al., 2019). The young and warm subducting Juan de Fuca plate leads to the shallow termination of the seismogenic zone in Cascadia with most seismic activity being restricted to offshore microearthquake events (Stone et al., 2018). In the absence of regular onshore seismicity, it is instead one of the most reliable sources of recurrent slow slip events (SSEs) globally (Rogers and Dragert, 2003), which are geodetically observed slow megathrust fault rupture events that last from a few days to two weeks in Cascadia. Here, SSEs are observed along the entirety of the margin with recurrence times of 10-19 months (Brudzinski and Allen, 2007). These events originate within the transitional zone, located down dip of the seismogenic zone and up dip of the stable sliding zone, and coincide with the onset of the mantle wedge corner (MWC; Hyndman et al., 2015), which is the triangular prism of mantle rocks sandwiched between the subducting oceanic plate and the overlying continental crust

In northern Cascadia, the deep (~0-50 km) structure of the subduction zone forearc has been extensively studied by active and passive source seismic data in the last few decades, including reflection and refraction studies (e.g., Nedimovic et al., 2003; Calvert et al., 2004), seismic tomography (e.g., Preston et al., 2003; Ramachandran et al. 2005), teleseismic receiver functions (e.g., Cassidy and Ellis, 1993; Bostock et al., 2002; Nicholson et al., 2005; Nikulin et al., 2009; Audet et al., 2009), and joint receiver function-surface wave inversion (e.g., Delph et al., 2018). Early studies found evidence of a thin layer with low seismic velocities beneath the forearc crust onshore, which was interpreted as an underplated fluid-rich layer above the megathrust fault (e.g., Nedimovic et al., 2003; Calvert et al., 2004). Later studies that use teleseismic receiver functions, which represent P-to-S wave conversions at boundaries in subsurface seismic velocities and are more sensitive to the P-to-S seismic velocity ratio (Vp/Vs), interpreted this low-velocity layer (LVL) with high Vp/Vs as the signature of fluid overpressure within the oceanic crust

(Abers, 2005; Audet et al., 2009; Bostock, 2013). Elevated pore fluid pressures are a result of metamorphic dehydration reactions as the subducting lithosphere is subjected to higher temperature and pressures, and low vertical permeability of the plate interface (e.g., Peacock et al., 2011; McLellan et al., 2022). The now widely-recognized LVL with high Vp/Vs in subduction zone forearcs (see Audet and Kim, 2016, and references therein) is thought to host slow slip events and accompanying seismic tremor (e.g., Calvert et al., 2020). Fluid overpressures along the subducting plate interface reduce the effective normal stress and decrease the frictional strength of the fault, resulting in the occurrence of SSEs (Abers, 2005; Audet et al., 2009; Liu and Rice, 2007).

In addition to the LVL, Bostock et al. (2002) found evidence of a dramatically reduced, and even inverted, continental Moho signature above the MWC in Cascadia. This signature was interpreted as the presence of serpentinites within the MWC, which form through the interactions of water with ultramafic rocks (Hyndman and Peacock, 2003). As water is introduced into the overriding plate beneath the forearc mantle, peridotites are metamorphosed into serpentinites, drastically altering the physical characteristics of the MWC (Peacock, 1993). Serpentinization was estimated at 40-60% based on the resolved shear-wave velocity of the MWC. Other studies found additional evidence of serpentinization of the MWC, including low Moho refracted (Pn) velocities (Brocher et al., 2003), large low-gravity anomalies and high magnetic anomalies (Blakely et al., 2005) coinciding with forearc lowlands along the margin. Nikulin et al. (2009) further found evidence of serpentinization near or above the megathrust fault in central Cascadia using receiver functions.

The remarkable correlation of the location of the MWC and the site of SSE has led to the suggestion that the widespread serpentinization of the forearc mantle in Cascadia may play a role in generating, or regulating, SSEs (Hyndman et al., 2015). Sheared serpentines are highly anisotropic (Bezacier et al., 2010), and this weak foliation fabric influences the mechanical strength of the fault by creating planes along which slip can occur more easily. Serpentinites also display low permeability with values more than one order of magnitude lower for flow perpendicular to foliation than parallel to foliation (Reynard, 2013). It has been suggested that the widely serpentinized MWC may

contribute to SSE occurrence by acting as an impermeable surface, and channelling fluids up dip to the LVL to increase pore-fluid pressure (Katayama et al., 2012; Hyndman et al., 2015; McLellan et al., 2022).

The presence of serpentinite in the MWC can be readily identified as they have a relatively unique seismic signatures with low *Vs* and high Poisson's ratio (or equivalently, Vp/Vs) in comparison to dry mantle peridotites (Christensen, 2004; Bezacier al., 2010). In addition to isotropic properties, serpentinites display significant anisotropy in the form of a slow-axis of hexagonal symmetry with percent anisotropy values up to 46% in single-crystal antigorite (Bezacier al., 2010). This contrasts with other minerals making up ultramafic rocks including olivine, which has a fast axis of hexagonal symmetry with values up to 22% (Kumazawa and Anderson, 1969) and pyroxenes with values up to 24% (Kumazawa, 1969). Overall, our understanding of the relationships between the occurrence of SSEs and the structural makeup of the MWC is limited, and further geological and geophysical constraints are needed.

In this study, we attempt to characterize the isotropic and anisotropic velocity structure of the MWC in northern Cascadia. We use receiver functions to produce 1D seismic velocity models at 5 stations located at different positions along dip above the subducting plate. We then use one of these stations that sample the mantle wedge to characterize seismic anisotropy in the MWC (Fig. 4.1). We then interpret our results in terms of serpentinization of the MWC and its relation to slow slip. Improved characterization of the Cascadian MWC provides further insights into the structure of the SSE source region and will lead to a greater understanding of the mechanism of SSE generation.

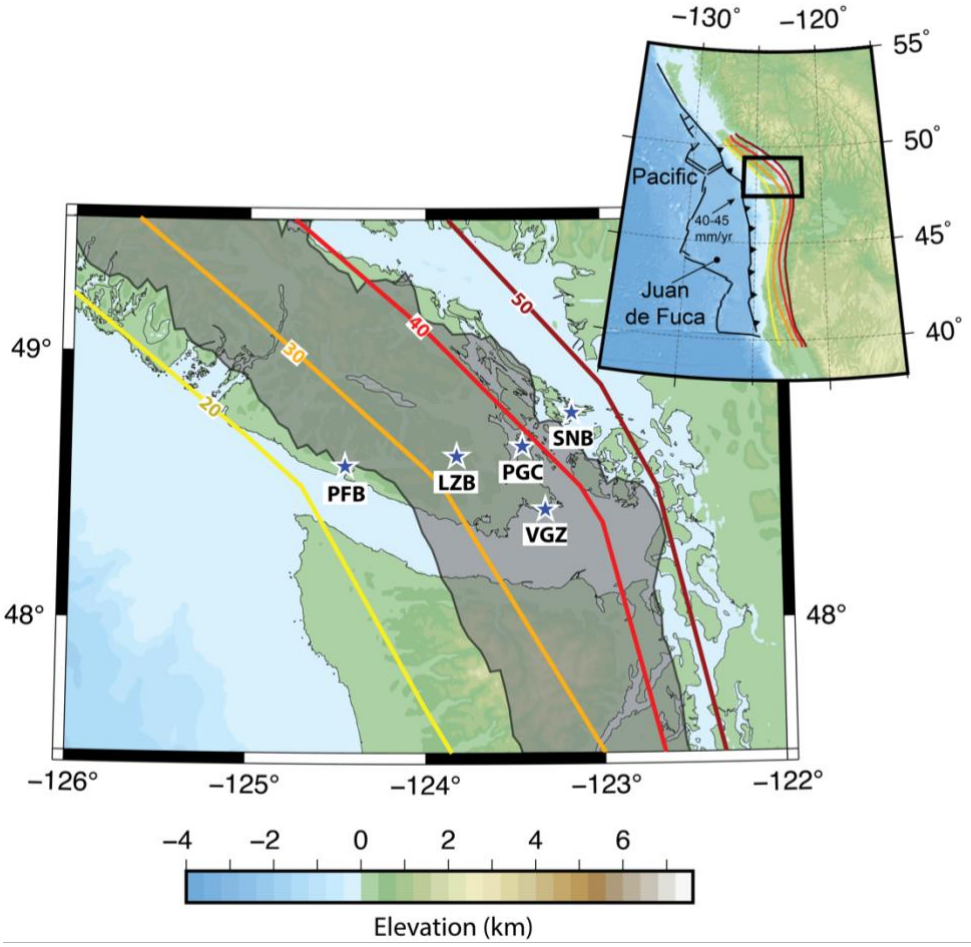

FIGURE 4.1: MAP OF NORTHERN CASCADIA SHOWING THE LOCATION OF THE 5 STATIONS USED IN THE ANALYSIS. STATION LOCATIONS ARE SHOWN BY BLUE STARS. THE GREY SHADED REGION SHOWS THE SSE SOURCE REGION INTERPRETED FROM TREMOR DENSITY. ESTIMATED SLAB DEPTH CONTOURS ARE INDICATED BY THE SOLID LINES (BOSTOCK ET AL., 2019). ADAPTED FROM GOSSELIN ET AL. (2020).

4.2 METHODS AND RESULTS

4.2.1 TELESEISMIC RECEIVER FUNCTIONS

Teleseismic earthquakes (those at epicentral distances >30°) produce many seismic body- and surface-wave phases that are recorded by the receiver along the three components of motion (vertical, and horizontal north and east). The horizontal components can be rotated to align parallel, and perpendicular to the source-receiver azimuth, known as the radial and transverse components, respectively. A receiver will record broadband teleseismic P waveforms including a direct P-wave arrival, which arrives at near vertical incidence. Found in the coda of the direct P arrival are the signals of many important P-to-S phase conversions that occur as the seismic body waves convert and reflect off interfaces separating subsurface layers with contrasting seismic wave velocities. These includes single converted phases (Ps) and free-surface reflected phases (PpPs, PsSs, and PpSs) (Fig. 4.2). A widely used technique for characterizing layer properties in the subsurface is the called the receiver function analysis (Langston, 1979), which exploits these converted phase arrivals to determine the velocity structure beneath a given seismograph station. In principle, the depth to the discontinuity could be easily extracted from determining the difference in arrival time between the direct P arrival and single reflected Ps phase. In reality, the Ps phase is often obscured by the P wave coda, which contains complex phases due to scattering and refractions resulting from the heterogenous structure of the earth at the source and along the propagation path. To characterize the structure beneath a given station, these path- and source-related effects must be removed from the signal. Receiver function analysis is the method used to remove the P pulse wavelet from the rest of the seismograms and recover the receiver-side seismic velocity structure (i.e., the Earth's impulse response).

The arrivals of several converted phases are visible in the results of a processed receiver function. Analysis of the pulses can reveal the signature of the subsurface structure through interpreting features of the signal. These features include the arrival time of the converted phase, the amplitude and polarity of the pulse, the presence of energy on the transverse component, and the variation in signal depending on back-azimuth direction.

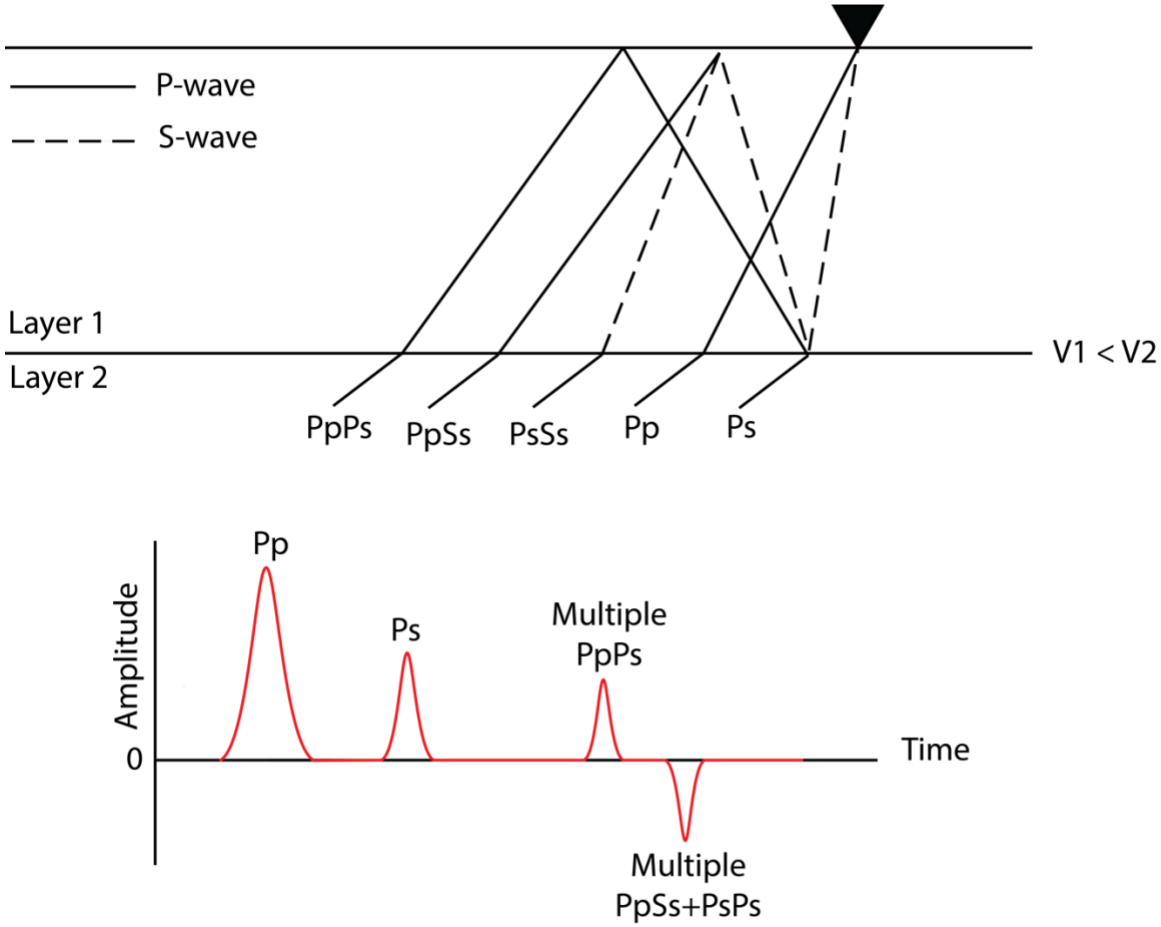

FIGURE 4.2: RECEIVER FUNCTION CONCEPTUAL DIAGRAM. (A) PHASE CONVERSIONS OBSERVED AT THE SEISMIC STATION REPRESENTED BY THE INVERTED BLACK TRIANGLE, AS P-WAVES REFLECT OFF BOUNDARIES SEPARATING LAYERS WITH AN IMPEDANCE CONTRAST. (B) SIMPLIFIED SIGNAL OBSERVED OF DIRECT P-WAVE AND CONVERTED PHASE ARRIVALS

The arrival time of the converted phases are sensitive to seismic velocities but can also be used to determine the depth to the interface between the two layers. The polarity of the pulse indicates whether the impedance contrast is positive or negative. For the direct converted phase (Ps) and the first free-surface multiple (PpPs), a positive pulse represents an upward decrease in seismic velocity across an interface, whereas a negative pulse represents the opposite case. This situation is reversed for the other free-surface multiples (PpSs + PsPs). The amplitude of the phase correlates with the velocity contrast across the two layers. In the case of a flat isotropic layered structure, all energy is confined to the radial component with no variation with back azimuth of the incoming wave as the velocity of seismic waves will be the same in all directions. The arrival time and amplitude of different phases will depend only on the incidence angle (or slowness) of the incoming P wave.

In the presence of a dipping layer (Fig. 4.3), energy will also be found on the transverse component for some back-azimuths due to out-of-plane conversions. Here, the timing and amplitude of the converted phases on both the radial and transverse components will depend on the back azimuth and the slowness of the incident ray (Fig. 4.4). Here, P-waves travelling in an up-dip direction will generate larger amplitude Ps phases on the radial component than those travelling in a down dip direction. Ps phase amplitude on the transverse component will be largest (positive and negative) at back-azimuths that correspond to along-strike directions. These differences can be used to constrain the geometry of the dipping structure including its dip direction and angle.

In the presence of material anisotropy, characterized by seismic waves velocities that vary as a function of sampling direction, P-waveform energy will again be present on the transverse component (Fig. 4.4). The arrival of pulses will depend on the orientation and amplitude of anisotropy, as well as the symmetry of anisotropy. In the case of hexagonal symmetry (i.e., described by either a fast axis or fast plane of seismic wave propagation), the orientation can be described based on the trend and plunge of the symmetry axis whereas the amplitude is described by the percent anisotropy, which is the ratio of velocities along the fast and slow axes.

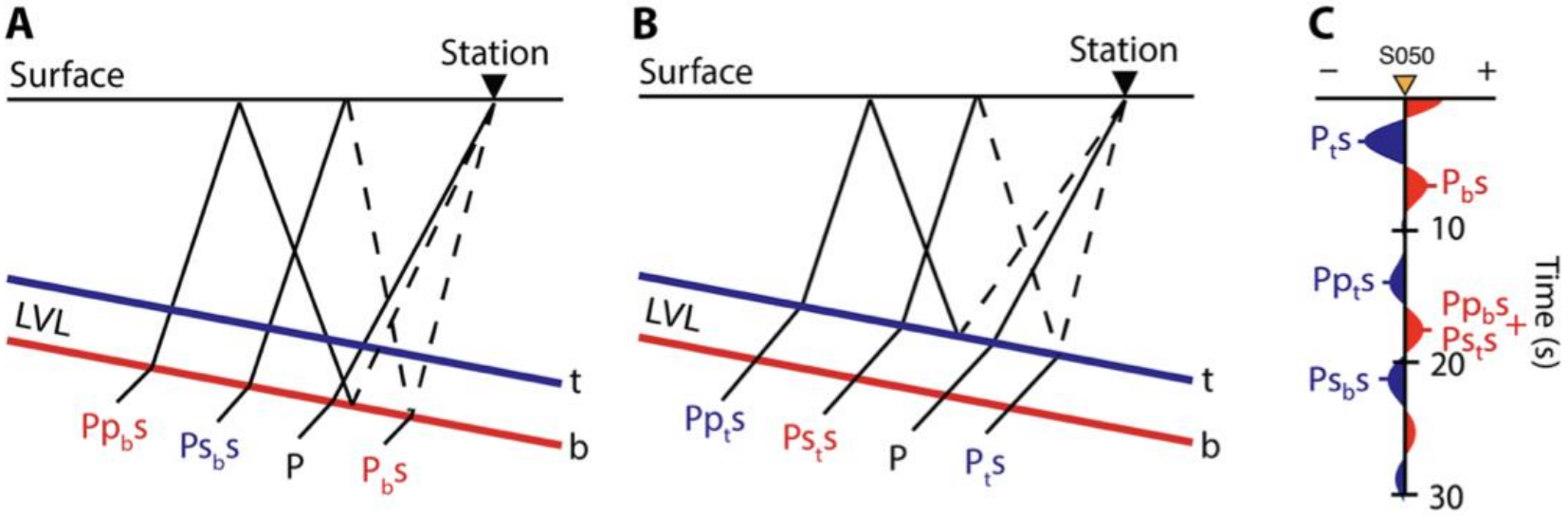

FIGURE 4.3: CONCEPTUAL DIAGRAM OF SECONDARY SEISMIC RAYS FROM INTERACTIONS OF AN INCOMING TELESEISMIC P WAVE WITH A DIPPING LOW-VELOCITY LAYER. PHASES GENERATED BY CONVERSIONS AT THE (A) BOTTOM AND (B) TOP BOUNDARIES. (C) RESULTING RECEIVER FUNCTION SHOWING POSITIVE (RED) PULSES AND NEGATIVE (BLUE) PULSES. POSITIVE PULSES ARE GENERATED FROM CONVERSIONS AT A BOUNDARY WITH POSITIVE IMPEDANCE CONTRAST WHILE NEGATIVE PULSES REPRESENT THE OPPOSITE CASE. FIGURE FROM AUDET AND SCHAEFFER (2018).

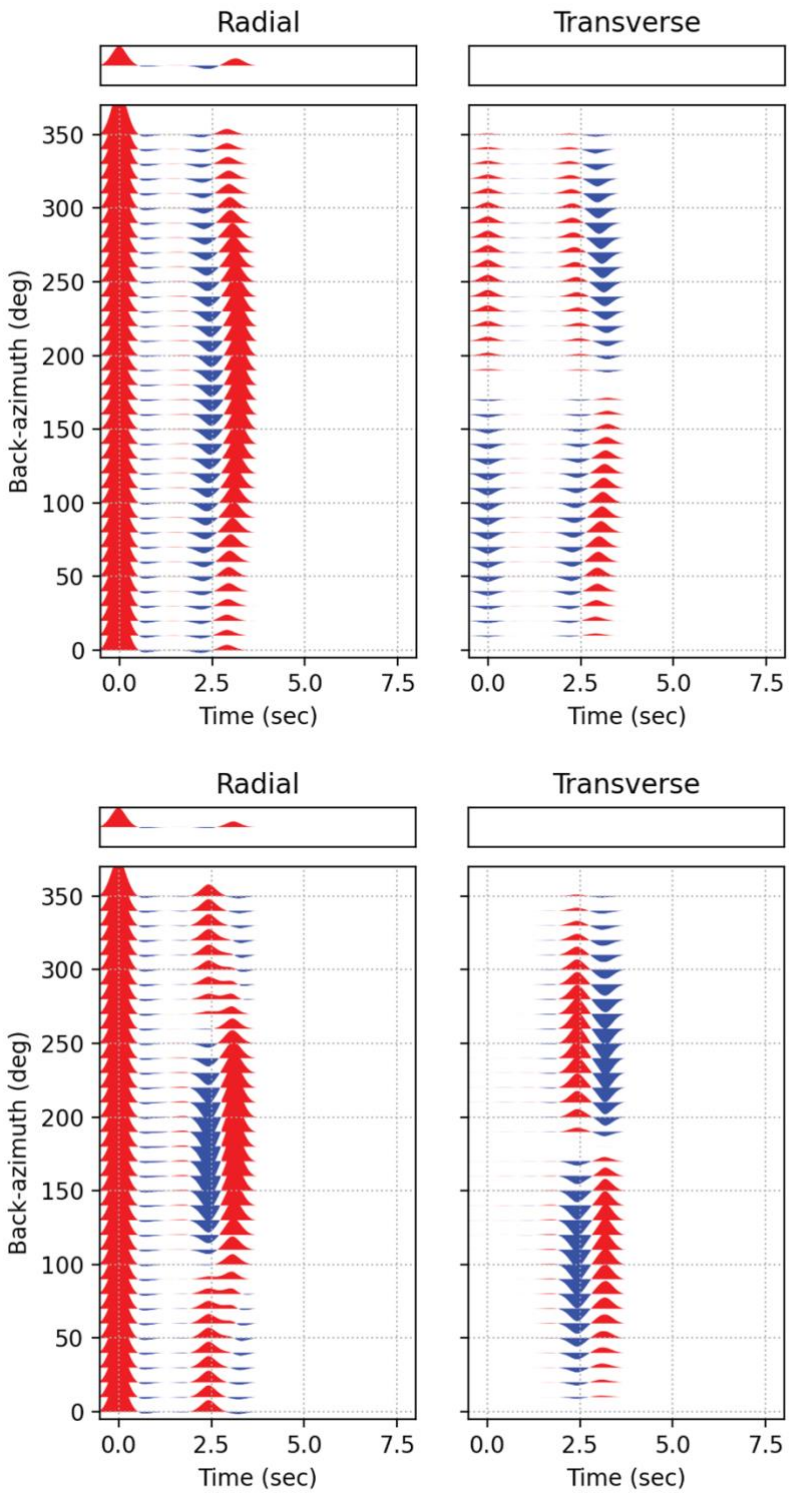

FIGURE 4.4: SYNTHETIC RADIAL AND TRANSVERSE RECEIVER FUNCTIONS SHOWING DIRECT P-TO-S PHASE ARRIVALS BASED ON THE PRESENCE OF (A) A DIPPING LOW-VELOCITY LAYER AND (B) 20% ANISOTROPY. THE TOP PANEL IN EACH CASE ARE THE STACKS OF THE RADIAL AND TRANSVERSE RECEIVER FUNCTIONS FROM ALL BACK AZIMUTHS.

If the plunge of the symmetry axis is greater than zero (i.e., non-vertical), the incident ray will travel at an angle to the fast-axis orientation, which will result in variations in seismic phase arrival times and amplitudes based on the back azimuth of the incident ray.

4.2.2 RECEIVER FUNCTION PROCESSING

The recording of a seismogram contains a combination of the source time function, the Earth's impulse response, and the instrument response. The mathematical operation relating the observed seismogram with the Earth's response and effective source time function (which includes the instrument response and any near-source attenuation) is known as convolution and can be described as:

$$u(t) = s(t) * G(t) = \int_0^{t_s} s(\tau)G(t-\tau)d\tau\,, \qquad Eq.\ 4.1$$

where $u(t)$ is the recorded seismogram, $s(t)$ is the effective source-time function, $G(t)$ is the Earth response, and t_s is the duration of the source. When imaging the Earth's subsurface, extracting $G(t)$ from $u(t)$ is necessary and is done through by reversing this operation, called deconvolution. Deconvolution is simple to accomplish in the frequency domain where it can be defined as:

$$G(\omega) = \frac{u(\omega)}{s(\omega)}, \qquad Eq.4.2$$

where $G(\omega)$, $u(\omega)$, and $s(\omega)$ are the Fourier transforms of $G(t)$, $u(t)$, and $s(t)$. This concept is applied in the case of the receiver function method where the signals of interest are those of the P-wave recording on the vertical and radial components. The particle motion of P-to-S converted phases is almost entirely horizontal and will dominate the radial component. Present on both the vertical and radial components are the source, path, and instrument effects which must be removed to extract the reflective phases. Here the receiver function can be defined as:

$$RF(\omega) = \frac{R(\omega)}{Z(\omega)}, \qquad Eq.4.3$$

where $RF(\omega)$ is the Fourier transform of the radial component of the receiver function, and $R(\omega)$ and $Z(\omega)$ are the Fourier transforms of the radial and vertical component recordings, respectively. Deconvolving the vertical component from the radial component isolates the locally generated Ps phases from the source, path, and instrument effects which results in direct sampling of the surface beneath the receiver.

In the presence of seismic noise, the functions $R(\omega)$ and $Z(\omega)$ are band-limited, which leads to near-zero values at the low- and high-frequency limits. This causes instability in the deconvolution due to the possible presence of very small values in the denominator. To account for this, the "water-level" technique (Clayton and Wiggins, 1976) stabilizes the deconvolution by introducing a regularization parameter. Langston (1979) introduced this technique in RFs, which can be written as:

$$RF(\omega) = \frac{R(\omega)\overline{Z(\omega)}}{\phi(\omega)}, \qquad Eq.4.4$$

where $\overline{Z(\omega)}$ is the complex conjugate of $Z(\omega)$, and

$$\phi(\omega)=\max\left\{Z(\omega)\overline{Z(\omega)}, c\ max\left[Z(\omega)\overline{Z(\omega)}\right]\right\}, \qquad Eq.4.5$$

where c is a constant called the "water-level", which controls the minimum allowable value for the denominator in the deconvolution calculation. The value of c is determined from the standard deviation of the pre-event noise spectrum.

4.2.3 APPLICATION TO CASCADIA

In this study, we use receiver functions (RF) to determine the isotropic and anisotropic structure of the subsurface beneath 5 stations in the forearc of northern Cascadia, belonging to the Canadian National Seismograph Network (CNSN). Data used in the analysis include P-wave seismograms from teleseismic events located at epicentral distances between 30 and 90 degrees and with magnitude > 5.5, from 1993-2021 with no constraint on back azimuth direction. Three-component P-wave seismograms were extracted for 150s time windows around the predicted P-wave arrival (from the IASP91

global reference model of Kennett and Engdahl (1991)) and down-sampled to 10 Hz. The horizontal component seismograms were rotated to the radial and transverse orientations and the data were compiled if the signal-to-noise ratio (calculated on the vertical component within a 10s window before and after the P wave arrival) was >5 dB. Receiver functions were calculated by deconvolving the vertical from horizontal components using the water level method. The RFs for each event were then bandpass filtered with corner frequencies of 0.1 and 0.5 Hz and stacked to amplify the signal.

Results of the RF calculations are shows in Fig. 4.5. At station PGC, which is thought to be located just up dip of the mantle wedge corner, the dominant signal is that of a dipping low-velocity layer (LVL). The signature of this feature is characterized by the coupled negative-and-positive pulses at ~5s on both the radial and transverse components, which is associated with the top and bottom boundaries of the LVL, respectively. This signal is again visible at stations VGZ and LZB, which are located just up dip of station PGC, but at earlier delay times due to the shallowing of the LVL. We also see a decrease in amplitude of both the negative and positive pulses at the latter two stations which is associated with the thinning of the LVL up dip (Audet and Schaeffer, 2018). Further up dip, the signal of the LVL is diminished with a low amplitude polarity reversal at station PFB. At station SNB, which is located furthest down dip, we see the latest arrival of the negative and positive pulses, which is consistent with the deeper location of the subducting slab. The receiver function signals at SNB show greater amplitudes than those observed further up dip, and with greater complexity in terms of variations with back-azimuths. This indicates a more complex structural environment than the simple dipping LVL model.

4.2.4 RECEIVER FUNCTION MODELING

4.2.4.1 ISOTROPIC VELOCITY PROFILES

As a first step in our analysis, we use receiver functions to determine the 1D isotropic seismic velocity structure beneath each station to produce a background model with flat layers. Because this model does not produce signal on the transverse component, we consider only the radial component and stack all data to produce a single representative RF

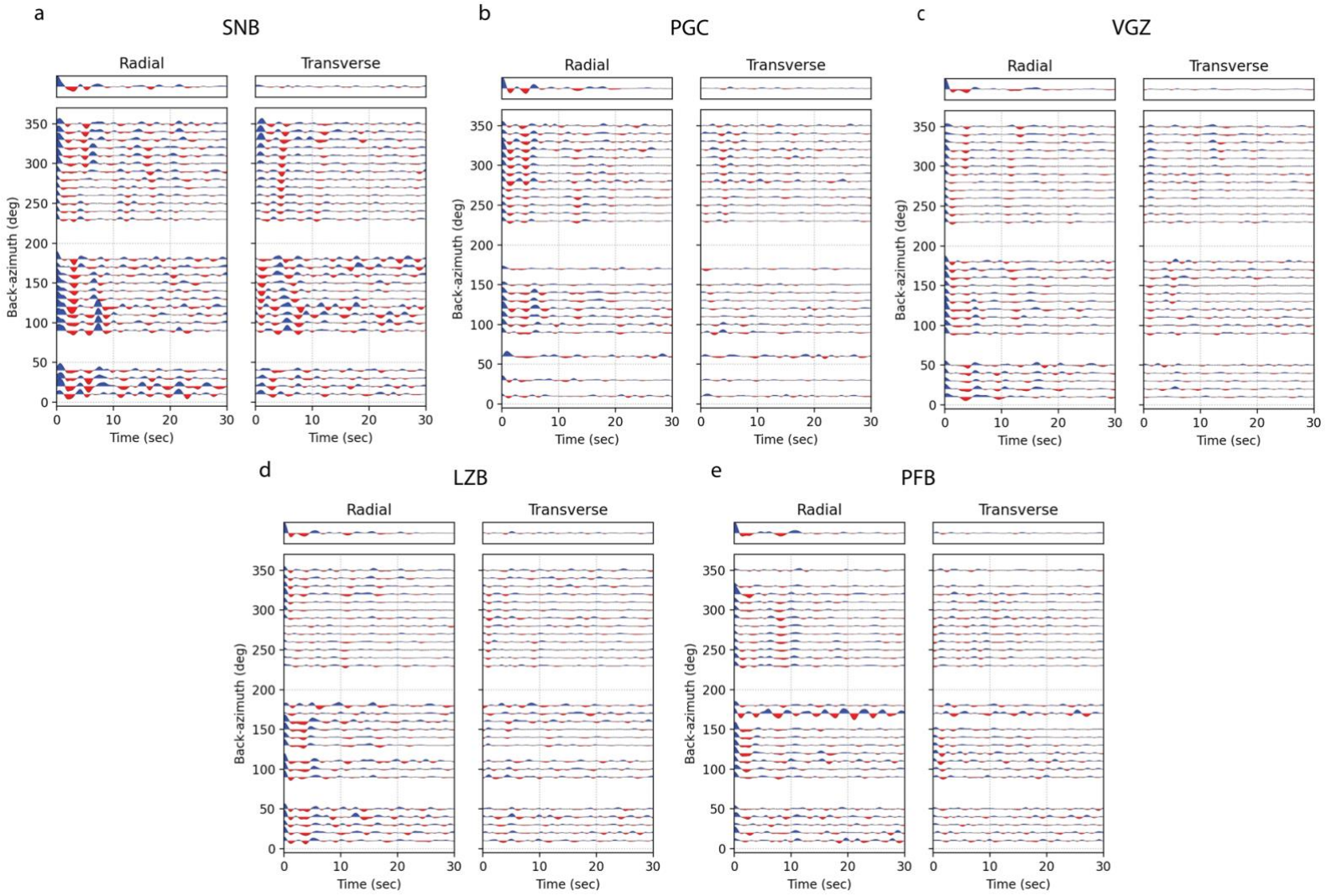

FIGURE 4.5: RECEIVER FUNCTIONS SORTED BY BACK AZIMUTH FOR STATIONS (A) PGC (B) SNB (C) VGZ (D) LZB (E) PFB. LEFT PANEL SHOWS THE RADIAL COMPONENT WHILE THE RIGHT PANEL SHOWS THE TRANSVERSE COMPONENT. THE STACKED RECEIVER FUNCTION IS SHOWN IN THE TOP PANEL IN EACH CASE.

seismogram. To obtain a preferred background 1D seismic velocity model beneath each station, teleseismic P-wave seismograms are synthesized using a subsurface model parameterized by a series of discrete, horizontal layers with uniform thickness, density and seismic velocity. Receiver functions are calculated from the synthetic seismograms using the process described previously. In practice, we use 30 layers equally spaced in depth between 0 (surface) and 60 km depth. Because receiver functions are primarily sensitive to the P-to-S velocity ratio (Vp/Vs), we fix the background density and P-wave velocity profiles, where Vp is 5.5 km/s at the surface, smoothly increases to 7.8 km/s between 15 and 55 km depth (which encompasses Moho depth), and remains constant thereafter, and estimate S-wave velocity (Vs, or equivalently, Vp/Vs) within each layer.

We calculate a misfit between the observed and predicted receiver functions using waveform anti-correlation (i.e., 1 – CC, where CC is the correlation coefficient), which has been shown to be more adequate than least-squares-based misfits in receiver function modeling studies (e.g., Frederiksen et al., 2003). The anti-correlation misfit is minimized using a global optimization method based on dual annealing (Xiang et al., 1997). The result of a single iteration of this procedure is a profile of Vs (or Vp/Vs) as a function of depth. We account for uncertainty in the reference P-wave velocity model by randomly perturbing Vp within each individual layer, where perturbations are drawn from a normal distribution with mean of zero and standard deviation of 0.2 km/s and re-estimating a Vs profile. This is repeated 20 times to capture the effects of uncertain reference models, and the Vs profiles are plotted as an ensemble of acceptable models. We select the mean of the ensemble as the preferred seismic velocity model for each station.

Fig. 4.6 shows the estimated isotropic Vs and Vp/Vs model for station PGC and the ensemble of best-fit predicted RFs. We see an increase in Vs from ~3 km/s to 4.5 km/s down to ~30km, where it drops back to ~3 km/s within a 4-6 km thick layer. This drop in Vs corresponds with an increase in Vp/Vs to ~2.2 over the same depth range. This inference is consistent with results from previous studies and suggest a layer of low seismic velocities and high Vp/Vs (i.e., the LVL) at crustal depths. Roughly similar signatures are observed at all stations, with a LVL depth that matches the location of the plate interface from Bostock et al. (2019) (Fig. 4.7). We note that for all stations, the LVL

is located immediately above the plate interface, and the subducting oceanic crust is characterized by a ~6 km thick gradient in Vs from the base of the LVL to upper mantle seismic velocities around 4.5 km/s. At station SNB, the LVL signature has a more subtle drop in Vs but is still characterized by high Vp/Vs at depths of ~40-50 km. We note that both Vs and Vp/Vs above the inferred LVL signal are generally higher at station SNB than at station PGC, and that the LVL at station SNB is located deeper than estimated Moho depth of the overriding (continental) plate from previous studies (~35-40 km, McCrory et al., 2014). These observations suggest that RF data beneath SNB are sampling a portion of the mantle wedge corner (MWC).

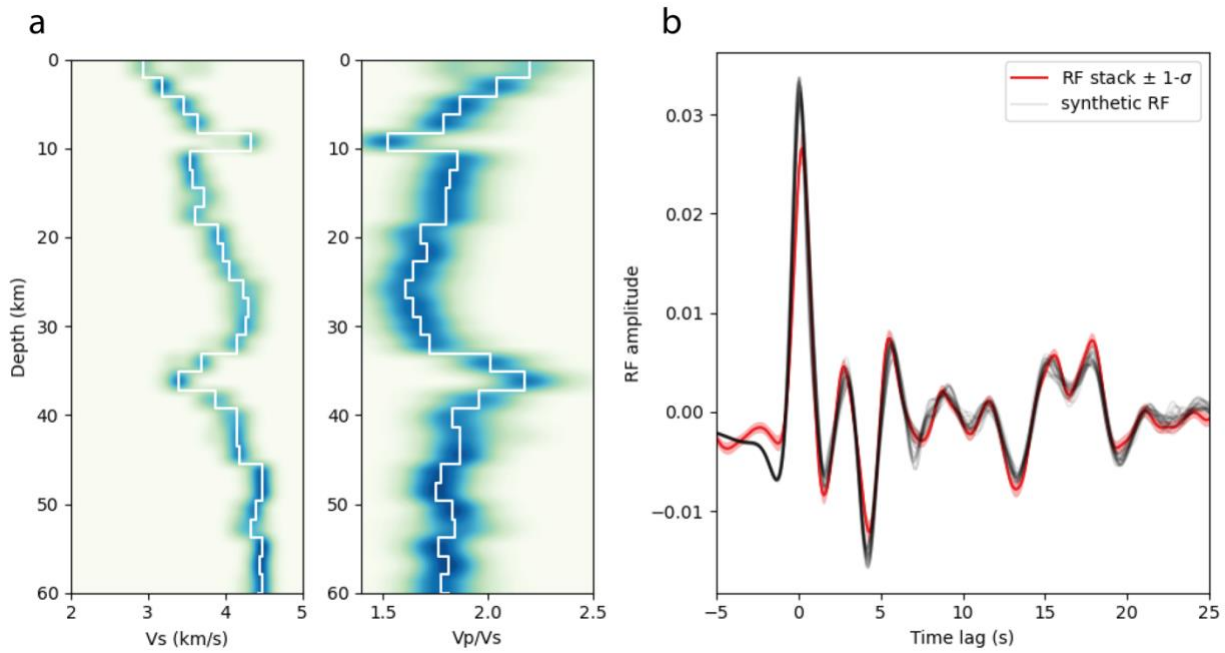

FIGURE 4.6: (A) RESULT OF 1D INVERSION FOR STATION PGC. LEFT PANEL SHOWS VS AS A FUNCTION OF DEPTH WHILE RIGHT PANEL SHOWS VP/VS RATIO. (B)BEST FIT PREDICTED RF PLOTTED WITH OBSERVED RF STACK WITH 1-SIGMA UNCERTAINTY.

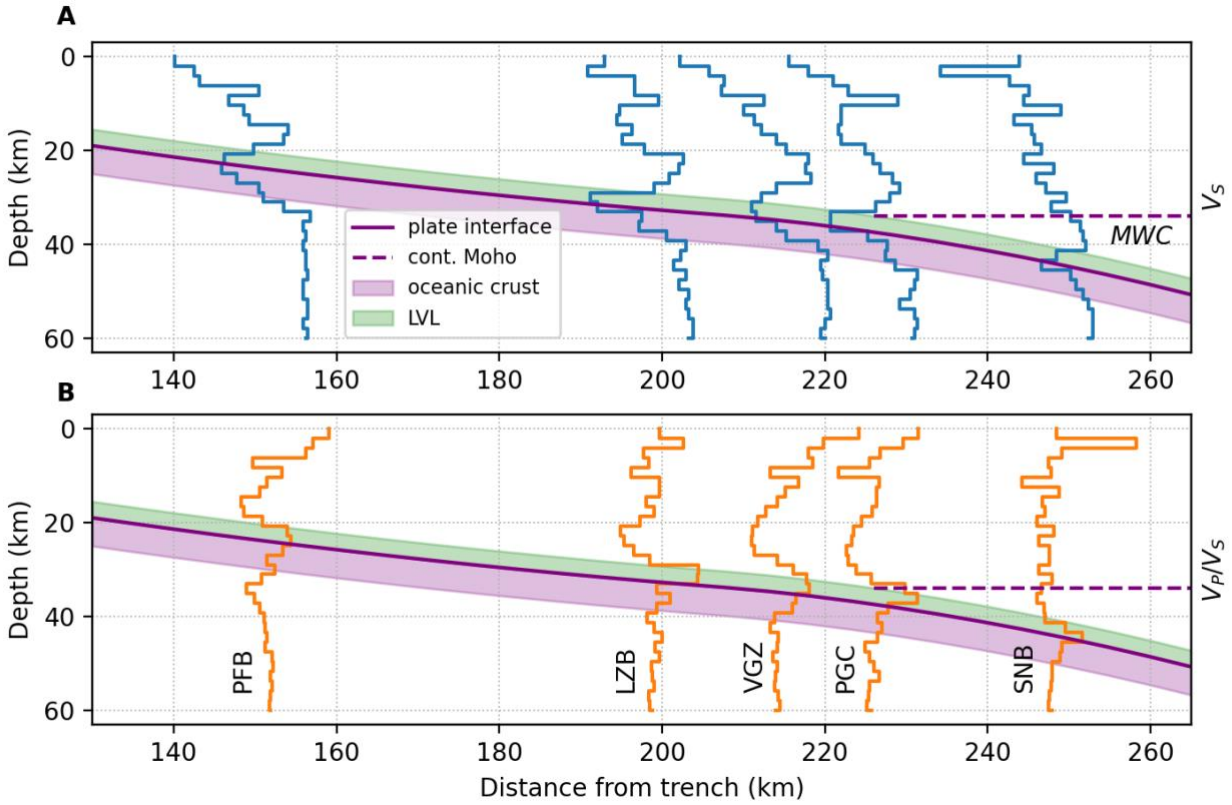

FIGURE 4.7: 1D (A) VS STRUCTURE AND (B) VP/VS STRUCTURE FOR THE 5 STATIONS ANALYSED. 1D PROFILES ARE PLOTTED BASED ON THE STATION DISTANCE FROM THE TRENCH. THE STRUCTURE OF THE SUBDUCTING SLAB IS SHOWN IN PURPLE WITH A 3.5 KM THICK LVL SHOWN ABOVE THE SLAB IN GREEN. THE DEPTH OF THE OBSERVED DECREASE IN VS AND INCREASE IN VP/VS CORRELATES WITH THE LOCATION OF THE LVL IN EACH CASE.

4.2.4.2 DIPPING LVL AND MANTLE WEDGE ANISOTROPY

Based on the observed signals in the RF data and the estimated 1D seismic velocity profiles, we infer the presence of a dipping low-velocity layer beneath all stations, with increased structural complexity beneath station SNB where the LVL may be in contact with the MWC. This analysis deliberately omitted the effects of layer dip and anisotropy in the background velocity model on RF data by ignoring variations with back-azimuth in both the radial and transverse components, which could be a severe limitation that can distort and bias interpretation. However, modeling seismograms for layer dip and material anisotropy is significantly more time-consuming than a simple 1D isotropic velocity model, and the number of model parameters to estimate becomes unwieldy in a global optimization procedure. Instead, we use the previous results to discretize the velocity model into five major units for station SNB and four major units for all other stations. The layers include: the continental crust, the continental mantle (only for station SNB; this layer corresponds to the MWC), the dipping low-velocity layer, the dipping oceanic crust, and the oceanic mantle represented by a half space. A second inversion is then performed to solve for the thickness of each layer, their average Vs, as well as the dip direction and angle of the LVL and oceanic crust (equal for both layers). This again is done by minimizing the anti-correlation misfit between generated and observed RFs, where in this case the generated RFs are synthetized using a forward modeling code that accounts for interface dip and possible anisotropy (Audet and Bloch, 2022), and we use the full range of both radial and transverse RF data including variations in both slowness and back-azimuth. In a final step, we attempt to identify the presence of anisotropy in the MWC beneath station SNB by fixing the isotropic model parameters based on results in the previous step and estimating the five parameters of the MWC (thickness, Vs, percent anisotropy, trend and plunge of the symmetry axis). We note that a limitation associated with the optimization problem based on dual annealing is the lack of uncertainty in the resulting estimates.

Table 4.1 shows the results of the inversion for station PGC in the isotropic case while Fig. 4.8 shows the observed and predicted receiver functions. We observe an ~3.6 km thick LVL with *a Vp*/*Vs* ratio of 2.5. This is consistent with previous estimates of *Vp*/*Vs* beneath station PGC (Audet et al., 2009) supporting the robustness of the inversion.

Table 2 shows the result of the inversion for station SNB in the isotropic case (i.e., without anisotropy in the MWC). The inversion solves for 8 parameters, which include the thickness and Vs of the continental crust, MWC, LVL, and oceanic crust. The results show an ~3.4 km LVL at depths of ~52 km below the surface, with an elevated Vp/Vs of ~2.2 which is consistent with previous observations (Audet et al., 2009). The results also show an ~10 km thick MWC at this location. If we assume a distance of ~25 km between the beginning of the MWC corner and station SNB based on the modelling of Moho depth by McCrory et al., 2014, as well as a slab dip of 15°-25°, the expected thickness of the MWC is ~6.7-11.6 km. Therefore, our estimate is within the range predicted from the geometry of the subducting slab. The results also indicate a Vs of ~3.6 km/s and a Vp/Vs ratio of 1.8 within the MWC. Using these results, the model was further parameterized to only solve for the anisotropic structure of the MWC beneath station SNB, by fixing the isotropic structure just determined. With a fixed Vp and estimated Vs (which returns the same value as the previous step), the anisotropy is further characterized by three parameters, which include the percent anisotropy and the trend and plunge of the axis of symmetry. The results estimate ~-14% anisotropy with a trend of ~235° and a dip of ~89°. The negative percent anisotropy implies a slow axis of symmetry.

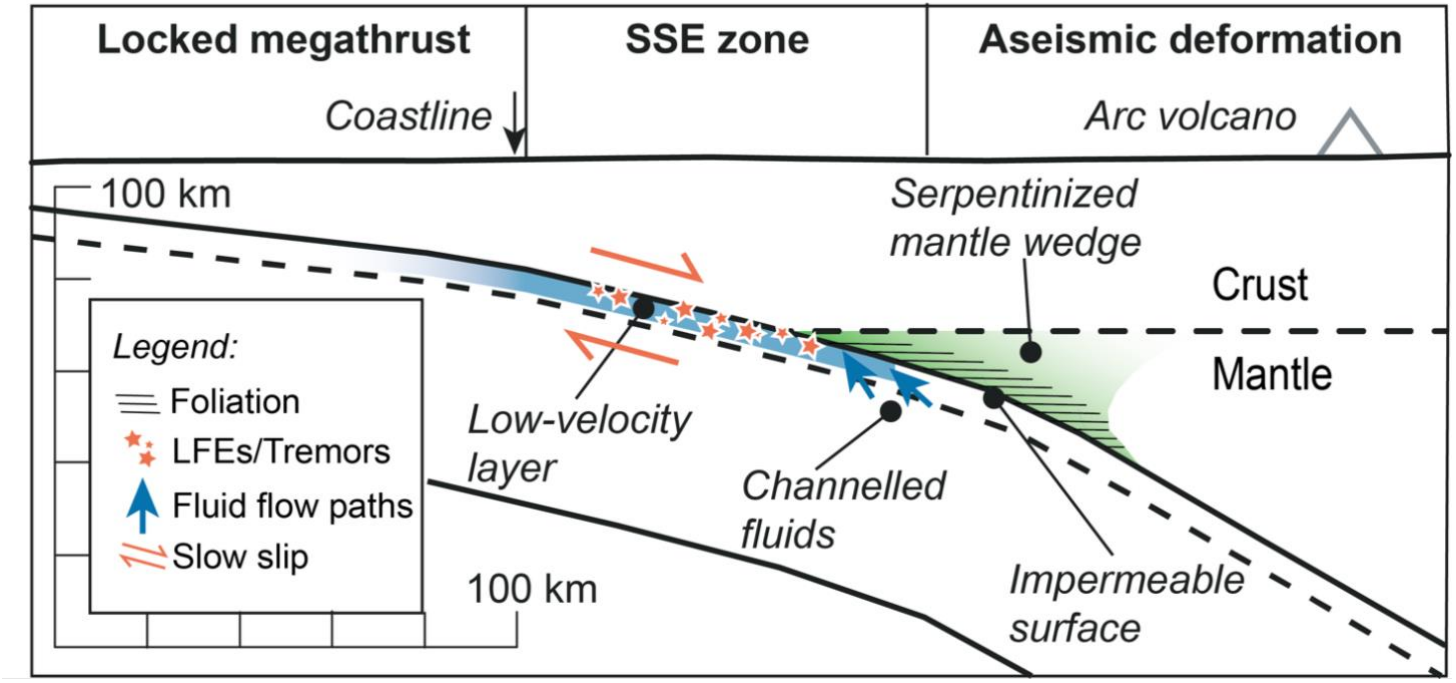

FIGURE 4.8: CONCEPTUAL DIAGRAM OF THE CASCADIA SUBDUCTION ZONE. THE PRESENCE OF HIGHLY SHEARED SERPENTINITE IN THE MWC CREATES AN IMPERMEABLE SURFACE VIA SUB-HORIZONTAL FOLIATION WHICH CAN CHANNEL FLUIDS UP DIP TO THE LVL. FLUID ACCUMULATION IN THIS REGION LEADS TO ELEVATED PORE FLUID PRESSURES, WHICH CONTRIBUTE TO SLOW SLIP OCCURRENCE, ILLUSTRATED HERE BY THE OCCURRENCE OF LOW-FREQUENCY EARTHQUAKES OR TREMORS WITHIN THE LVL. FIGURE ADAPTED FROM GOSSELIN ET AL., 2020

TABLE 4.1: RESULTS OF THE INVERSION FOR STATION PGC IN THE ISOTROPIC CASE. WE SOLVE FOR LAYER THICKNESS AND VS OF THE UPPER CRUST, LVL, SLAB CRUST, AND VS OF THE SLAB MANTLE.

	Thickness (m)	Density* (kg/m^3)	Vp* (m/s)	Vs (m/s)
Upper Crust	35684	2600	6540	3679
LVL	3570	2600	6540	2532
Slab Crust	4235	2600	6540	3710
Slab Mantle	N/A	3200	8000	4619

TABLE 4.2: RESULTS OF THE INVERSION FOR STATION SNB. WE FIRST SOLVE FOR THE THICKNESS AND VS IN THE ISOTROPIC CASE FOR THE UPPER CRUST, MWC, LVL, AND SLAB CRUST, AND THE VS OF THE SLAB MANTLE. THESE VALUES ARE THEN FIXED, AND A SECOND INVERISON IS DONE TO SOLVE FOR ANISOTROPY IN THE MWC.

	Thickness (m)	Density* (kg/m^3)	Vp* (m/s)	Vs (m/s)	Percent Anisotropy	Slow-axis-trend (deg)	Slow-axis plunge (deg)
Upper Crust	43167	2600	6540	3965	N/A	N/A	N/A
MWC	9760	2620	6600	3609	-14	235	89
LVL	3398	2600	6540	2973	N/A	N/A	N/A
Slab Crust	6966	2600	6540	3802	N/A	N/A	N/A
Slab Mantle	N/A	3200	8000	4619	N/A	N/A	N/A

*These values are fixed in the inversion.

4.3 DISCUSSION

4.3.1 EVIDENCE OF MANTLE WEDGE SERPENTINIZATION

The results shown here are consistent with widespread serpentinization of the MWC in Cascadia. We observe low Vs and high Vp/Vs which differ from the values of normal upper mantle peridotite; therefore, a largely peridotite MWC is unlikely. Furthermore, olivine gives rise to seismic anisotropy represented by a fast axis of symmetry where percent anisotropic values of ~10% are considered high. Vs and Vp/Vs values estimated here are instead consistent with typical values observed for antigorite-serpentinite (Vs of 3.5-3.8 km/s and Vp/Vs of ~1.85; Reynard, 2013). The estimate of Vs can be used to approximate a 40-50% level of serpentinization, which supports previous observations of incomplete serpentinization in the MWC (Bostock et al., 2002). Values up to 40-50% anisotropy have been observed in naturally foliated serpentinite, which represents an end-member case of extreme anisotropy (Bezacier et al., 2010). The magnitude of seismic anisotropy found here (~14%) again provides support for incomplete serpentinization of the MWC in Cascadia as lower percent anisotropy may reflect the heterogeneous distribution of serpentinite and peridotite in this region.

The anisotropy of foliated serpentinite is characterized by a slow axis of symmetry, resulting in two fast axes (which form a fast plane) aligned parallel to foliation, and one slow axis aligned perpendicular to foliation. Therefore, based on our results, the anisotropic parameters correspond with a sub-horizontal planar foliation fabric with a strike of ~325° and a dip of ~1°. The predicted strike of foliation is nearly parallel to the trench while the dip is at an angle of ~15-25° from the subducting plate. This is consistent with that of a highly sheared serpentinite being deformed by the downgoing slab, similar to S-C mylonitic fabric (Song and Kim, 2012). These results are in agreement with predicted anisotropy patterns from lab measurements (Katayama et al., 2009) and observed anisotropy from seismic studies (Long and van der Hilst, 2006; Smith et al., 2001).

4.3.2 IMPLICATION FOR SLOW SLIP IN CASCADIA

The presence of an LVL with high Vp/Vs has been widely observed at the top of subducting slabs at global subduction zones (Abers, 2005; Audet and Kim, 2016) and is well correlated with the site of SSE occurrence. Metamorphic dehydration reactions, occurring in the slab as it undergoes an increase in P-T conditions, are known to release fluids near the site of the MWC and LVL (Condit et al., 2020; McLellan et al., 2022), which can raise pore fluid pressures at the plate interface to near lithostatic levels (Audet al., 2009). This has the effect of reducing the effective normal stress and allowing slip to occur in regions that would otherwise be frictionally stable (Gao and Wang, 2017). There is current debate on whether the fluids are produced *in situ* (Condit et al., 2020) or are transported up dip from beneath the MWC (Hyndman et al., 2015; McLellan et al., 2022). The remarkable correlation between tremor location and the MWC along the entirety of the CSZ provides strong support for the latter hypothesis as the permeability structure of serpentinite may play a vital role in mobilizing fluids along the plate interface (Kawano et al., 2011). Our results, as well as previous observations (e.g. Bostock et al., 2002, Bocher et al. 2004), suggest that the MWC in Cascadia is widely, but incompletely, serpentinized.

Serpentinite has significant effects on the permeability structure of the interface between the overriding forearc mantle and subducting slab. Laboratory studies indicate that there is strong permeability anisotropy in serpentinite, with higher permeability being observed parallel to shear, and thus plate dip (Katayama et al., 2009; Kawano et al., 2011; Okazaki et al., 2013). In this case, the impermeable serpentinite plays two roles in generating fluid over pressures, first by creating an impermeable seal to trap fluids by restricting vertical movement, and secondly, by channelling fluids up dip where they can accumulate more readily. Furthermore, the inferred fault-valve behaviour of the plate interface during slow slip, whereby cyclic accumulation and release of fluid pressure accompanies slow slip events, is observed at stations near the MWC in Cascadia (Gosselin et al., 2020). This lends further support to the fluid mobilization hypothesis (Hyndman et al., 2015; McLellan et al., 2022). Finally, we note that serpentinite fabrics may also play a role in the frictional process itself by controlling the dynamic friction and slip stability (Scuderi and Carpenter, 2022).

4.3.3 OTHER IMPLICATIONS

The 40-50% level of serpentinization estimated here may have implications regarding transport pathways of fluids through the overriding plate. Based on the P-T condition and age of the subducting system in Cascadia, complete serpentinization of the MWC would be expected from simple fluid diffusion through a porous medium (Abers et al., 2017). Our estimated 40-50% serpentinization indicates that fluid diffusion may not be effective in the MWC, most likely due to the large permeability anisotropy just discussed (Kawano et al., 2011). Serpentinization may be complete near the interface where fluids are abundant but may prevent the vertical movement of fluid, and thus further serpentinization of the MWC, upwards of this serpentinite-rich layer. Instead, this excess fluid can be channeled up dip and accumulate in the LVL (Fig. 4.8). We note that our data would not resolve a vertical gradient in serpentinization, and only provide a bulk estimate over the entire MWC.

Due to the weak rheology and low density of serpentinite, widespread serpentinization of the MWC has significant implications for mantle wedge convection models where a fully coupled subducting slab and mantle wedge are typically assumed (McKenzie, 1969). In this case, the mantle wedge moves downwards at the same velocity as the subducting slab. In the case of a hydrated mantle wedge, the weak rheology of serpentinite will decrease the coupling between the subducting slab and mantle wedge focusing deformation in the serpentinized layer preventing full mantle wedge convection (Hyndman and Peacock, 2003). The low density of serpentinite also creates positive buoyancy which counteracts typical convection patterns of mantle wedge flow (Davies and Stevenson, 1992; Kincaid and Sacks, 1997). With normal flow patterns occurring elsewhere in the MWC, the hydrated forearc mantle can become isolated from the overall mantle wedge flow system (Hyndman and Peacock, 2003). This presents another possible explanation for incomplete serpentinization due to sluggish mantle mixing from convection induced flow. Here, peridotites from deeper within the mantle may be cycled up dip resulting in a heterogenous distribution of serpentinites and peridotites in the MWC.

4.4 CONCLUSIONS

We use receiver function analysis to identify the presence and nature of anisotropy in the Cascadia MWC. We estimate an ~10km thick mantle beneath station SNB with low *Vs* and high *Vp/Vs* which is consistent with the presence of serpentinite. We observe 14% anisotropy with a slow-axis of symmetry that corresponds with trench-parallel and sub-horizontal foliations. This is consistent with the presence of highly sheared serpentinite being deformed by the downgoing slab. The seismic properties of serpentinite measured here imply incomplete serpentinization of the Cascadia MWC. We hypothesize that the permeability anisotropy of serpentinite may prevent vertical fluid flow, thus limiting widespread serpentinization to the region surrounding the plate interface. We further suggest that serpentinite may play an important role in channelling fluids up dip to the site of the LVL, which promotes the generation of SSEs. This potentially implicates the serpentinized MWC in playing an important role in setting the conditions necessary for slow slip. Further characterization of serpentinites in global subduction zone forearc mantles will continue to provide insight into the role it plays in slow slip occurrence.

PART III: CONCLUSIONS

5

5.1 SUMMARY OF RESULTS

In this thesis, three approaches were used to answer questions regarding the physical conditions that facilitate the nucleation of SSEs on a global scale as well as along a single subduction zone. Machine Learning techniques were used to determine the relationship between short-term and long-term SSEs and subducting plate features, including the oceanic plate age, sediment thickness entering the subduction zone, seafloor roughness, slab dip, and relative plate velocity. We find a strong correlation between young subducting oceanic lithosphere and short-term SSEs, which is consistent with models of SSEs where elevated temperatures are necessary to generate fluids through metamorphic dehydration reactions at the shallow depth of the transitional friction zone. More moderate correlations are observed with sediment thickness and relative velocity where a thicker sediment layer is positively correlated with short-term SSE and relative velocity is negatively correlated with short-term SSE. The models trained in the short-term case showed sufficient predictive power with mean accuracies between 85 and 100%. We used these models to predict the occurrence of short-term events along South America, northern Sumatra, southern Mexico, the Aleutian Islands, Ryuku, and Vanuatu. There is less obvious correlation between these features and long-term SSEs. The relationship between subducting plate age and these events is not established here and the models in the long-term case showed less success with model accuracies between 70 and 90%. This may provide support for models of slow slip that invoke different driving mechanisms of fault weakening in each case.

The second approach involved constructing thermal models along the entirety of the CSZ to determine margin-wide variations in slab dehydration. The thermal structure of a subduction zone depends on many of the physical characteristics described in the previous approach. This includes the subducting plate age that determines the geotherm of the incoming plate, the plate dip that describes the geometry of the slab, sediment

thickness that acts as an insulating layer affecting the geotherm, and the plate convergence rate that affects shear heating along the plate interface. The variations in these parameters along strike in Cascadia are significant enough to produce different patterns of slab dehydration. We observe greater fluid flux rates in northern and southern Cascadia in the vicinity of the MWC and site of slow slip in comparison with those observed in central Cascadia, which correlates with recurrence times between events in these regions. These results are consistent with models where the rate at which fluid overpressures are generated drive variations in SSE behaviour along strike.

The third approach utilized teleseismic receiver functions to estimate isotropic and anisotropic seismic velocity structure of the Cascadia forearc, specifically in the MWC. We invert for these structural parameters by minimizing the misfit between observed and synthetic receiver functions generated for different model setups. In the isotropic case, we estimate *Vs* and *Vp/Vs* in the MWC that are consistent with 40-50% levels of serpentinization. Anisotropy is characterized by values of 14% with a slow axis of symmetry that corresponds with sub-parallel foliations. This final approach considers the role of the overriding plate in generating slow slip, where the presence of widespread serpentinization near the interface facilitates fluid mobilization to the site of SSEs.

5.2 THESIS TOPICS REVISTED

Overall, this thesis provides insight into the following questions:

I) Why does fault slip behaviour vary across global subduction zones?

The results of chapter I indicate that variations in the physical characteristics of the subducting slab likely play a role in the type of slip behaviour observed at subduction zones. Young subducting lithosphere is strongly correlated with short-term SSEs indicating that the thermal structure of the forearc may play an important role in generating the conditions necessary for slow slip. The results of chapter II indicate that slip behaviour along a given subduction zone may vary based on the P-T conditions near the plate interface. These conditions control the pattern of slab dehydration, which in turn can drive recurrence patterns of SSEs. The thermal structure and geometry of the subducting slab vary widely globally, which may influence slip behaviour based on the depth of important metamorphic dehydration reactions. These results also favour models where serpentinization plays a role in localizing SSEs near the MWC through fluid mobilization. The results of chapter III provide evidence for the role of serpentinization of the MWC in generating elevated pore fluid pressures near the site of SSEs. The degree of serpentinization of the MWC in global forearcs varies greatly based on the thermal structure and geometry of the subducting slab as described above. If serpentinization plays an important role in facilitating episodic deep SSE, an MWC that lacks widespread serpentinite may also lack the conditions necessary for slow slip.

II) Can slow slip behaviour be explained by a single process, e.g., slab dehydration, or are there various mechanisms by which the mechanical strength of the slab is altered that can produce these events?

The results of chapter I suggest that different mechanisms may be behind generating short-term versus long-term SSEs. Parameters that control the thermal structure, and in turn patterns of slab dehydration, correlate more closely with short-term rather than long-term events. This may support the idea

that the difference in location and behaviour (e.g., lack of tectonic tremor) of long-term events may be a result of a different mechanism of nucleation. The results of chapter II support models of slow slip where metamorphic dehydration reactions are a mechanism of fault weakening through the generation of elevated pore-fluid pressures. Here, an abundance of fluid is released in the vicinity of the MWC, which may then be channeled to the site of slow slip. Furthermore, the along-strike variation in SSE behaviour and calculated slab dehydration patterns is consistent with the rate of fluid production being a mechanism of generating diverse slow slip behaviour.

III) What role does the down-going versus overriding plate have in creating the necessary conditions for slow slip nucleation.

The results of chapter I and II provide evidence for the role of the down-going plate in producing the conditions necessary for SSEs. Down-going plate features such as subducting plate age, sediment thickness, and relative plate velocity correlate with the observance of short-term SSEs. The mechanism in which variations in these parameters control the spectrum of slow slip behaviour is explored in chapter II, where they are shown to alter the pattern of slab dehydration. Chapter III looks at the role of widespread serpentinization in the overriding plate mantle in facilitating the generation of elevated pore fluid pressures at the site of SSEs. The correlation between the location of the MWC and slow slip as well as the incomplete nature of serpentinization in Cascadia support mechanisms in which serpentinites in the overlying mantle acts as an impermeable layer that channels fluid up dip to the location of SSEs.

5.3 FUTURE CONSIDERATIONS

Continuing research with a focus on slow slip at a global scale will provide further insight into whether slow slip is a universally observed mechanism of stress accommodation or whether its occurrence is constrained to regions with certain physical properties. Improvements in GNSS and seismograph station density will provide clarity to these questions as the detection threshold for events is lowered, providing further constraints on where slow slip is and isn't observed. It will also provide insight into the different mechanisms behind short-term and long-term SSEs, including whether they are generated by the same processes (i.e., elevated pore-fluid pressures) or if the different site of their nucleation represents different mechanisms of fault-strength weakening. Chapter I of this thesis represents the first iteration of the novel application of machine learning methods to the study of global slow slip. This type of work will benefit greatly from improvements in slow slip detection by removing limitations associated with a small dataset as well as providing further constraints on models predicting slow slip. Further work of this nature can explore more characteristics of subduction zones, most notably those of the upper plate which were not explored here, to further our understanding of the conditions that favor slow slip.

Further improvements in thermal and petrologic modelling of subduction zones will provide a better understanding of the conditions that generate SSEs. Current limitations associated with thermal modelling include uncertainty in specific model parameters including the degree of hydrothermal circulation, the amount of heat generated through shear heating, the contribution of heat producing elements, as well as in subduction zone structure (e.g. depth to Moho, slab contours). Further resolving these estimates will produce more accurate models, better revealing the conditions at the site of slow slip occurrence. Chapter II of this thesis represents a rare attempt to model the along-strike variation in P-T conditions at high resolution along a single subduction zone. Applying this methodology to different subduction zones will provide further constraints on the relationship between fluid flux and slow slip, as well as the role the MWC plays in generating the conditions necessary for slow slip.

Geochemical analysis of major and trace-element data and isotopic compositions can be used to determine the degree of fluid mobilization which will provide important constraints on the rate at which fluid overpressures are generated. The mechanism of slow slip generation presented in this thesis implicates the role of fluid transportation in generating elevated pore fluid pressures. Studying exhumed subduction zone rocks will provide further constraints on the extent of fluid transport as well as how widespread these processes are. This will aid in distinguishing the relative importance in the rate of processes that generate fluids (e.g., slab dehydration; fluid mobilization) versus those that trap fluids (e.g., mineral precipitation).

Characterizing the environment of slow slip will aid in the generation of models of fault-slip that can explain the diverse spectrum of stress accommodation in subduction zones. Constraints on the rheology of important lithologies, structural heterogeneity, P-T conditions, and pore-fluid pressures are all necessary to meaningfully parameterize models to better represent the subduction zone system.

General improvements in geophysical and geological observations in subduction zones will further our understanding of the earthquake cycle and the role that slow slip plays in it. The significant amount of stress accommodated by SSEs globally has important implications on earthquake hazard estimates. A universal model of subduction zone deformation, which accounts for the spectrum of slip transients as well as other modes of deformation, will increase our understanding of earth processes. In doing so, it will improve hazard mitigation efforts which have far reaching societal implications, both economically and for public safety.

BIBLIOGRAPHY

Abers, G.A. (2005), Seismic low-velocity layer at the top of subducting slabs: observations, predictions, and systematics. Phys. Earth Planet. Inter. 149: 7-29, doi:10.1016/j.pepi.2004.10.002

Abers, G.A., MacKenzie, L.S., Rondenary S., Zhang, Z., Wech, A.G., Creager K.C. (2009), Imaging the source region of cascadia tremor and intermediate-depth earthquakes. Geology. 37: 1119-1122, doi:10.1130/G30143A.1

Abers, G.A., van Keken, P.E., Hacker, B.R. (2017), The cold and relatively dry nature of mantle forearcs in subduction zones. Nature geoscience. Doi:10.1038/NGEO2922

Angiboust, S., Pettke, T., De Hoog, J.C.M., Caron, B., Oncken, O. (2014), Channelized fluid flow and eclogite-facies metasomatism along the subduction shear zone. J. Petrol. 55: 883-916, doi:10.1093/petrology/egu010

Angiboust, S. and Raimondo, T. (2022), Permeability of subducted oceanic crust revealed by eclogite facies vugs. Geology. 50(8): 964-968, doi:10.1130/G50066.1

Angus, D.F., Gordon, R.G., DeMets, C. (2011), Geologically current motion of 56 plates relative to the no-net rotation reference frame. Geochemistry, Geophysics, Geosystems. 12(11): 13, doi:10.1029/2011GC003751

Audet, P., Bostock, M.G., Christensen, N.I., Peacock, S.M. (2009), Seismic evidence for overpressured subducted oceanic crust and megathrust fault sealing. Nature. 457(7225): 76-78

Audet, P., Bostock, M.F., Boyarko, D.C., Brudzinski, M.R., Allen, R.M. (2010), Slab morphology in the Cascadia fore arc and its relation to episodic tremor and slip. J. Geophys. Res. 115, B00A16, doi:10.1029/2008JB006053

Audet, P. and Burgmann, R. (2014), Possible control of subduction zone slow-earthquake periodicity by silica enrichment. Nature. 510: 389-392, doi:10.1038/nature13391

Audet, P., Kim, Y. (2016), Teleseismic constraints on the geological environment of deep episodic slow earthquakes in subduction zone forearcs: a review. Tectonophysics. 670: 1-15

Audet, P. and Schaeffer, A.J. (2018), Fluid pressure and shear zone development over the locked to slow slip region in Cascadia. Science advances. (4)3, eaar2982

Audet, P., & Bloch, W. (2022), PyRaysum: Software for modeling ray-theoretical body-wave propagation. Zenodo, doi.org/10.5281/zenodo.6095749

Bassett, D. and Watts, A. (2017), Trench Axis Geometries for Global Subduction Zones. Interdisciplinary Earth Data Alliance (IDEA). doi:10.1594/IEDA/324029

Beavan, J., Wallace, L., Fletcher, H., Douglas, A. (2007), Slow Slip Events on the Hikurangi Subduction Interface, New Zealand. In: Tregoning, P., Rizos, C. Dynamic Planet. International Association of Geodesy Symposia. 130, doi:10.1007/978-3-540-49350-1_64

Behr, W.M. and Burgmann, R. (2021), What's down there? The structures, materials and environment of deep-seated slow slip and tremor. Phil. Trans. R. Soc. 379: 20200218, doi:10.1098/rsta.2020.0218

Benioff, H. and Press, F. (1958), Progress report on long period seismographs. Geophysical Journal of the Royal Astronomical Society. 1(3): 208-215, doi: 10.1111/j.1365-246X.1958.tb00054.x

Beroza, G.C. and Jordan, T.H. (1990), Searching for slow and silent earthquakes using free oscilations. Journal of Geophysical Research-Solid Earth and Planets. 95(B3): 2485-2510, doi: 10.1029/JB095iB03p02485

Beroza, G. C. and Ide, S. (2011), Slow Earthquakes and Nonvolcanic Tremor. The Annual Review of Earth and Planetary Sciences. 30: 271-296

Bezacier, L., Reynard, B., Bass, J.D., Sanchez-Valle, C., Van de Moortele, B.V. (2010), Elasticity of antigorite, seismic detection of serpentinites, and anisotropy in subduction zones. Earth and Planetary Sciences Letters. 289: 198-208

Blakely, R.J., Brocher, T.M., Wells, R.E. (2005), Subduction-zone magnetic anomalies and implications for hydrated forearc mantle. Geology. 33(6): 445-448, doi:10.1130/G21447.1

Bonvalot, S., Balmino, G., Briais, A., Kuhn, M., Peyrefitte, A., Vales, N., Biancale, R., Gabalda, G., Reinquin, F., Sarrailh, M. (2012), World Gravity Map. Commission for the Geological Map of the World.

Bostock, M.G., Hyndman, R.D., Rondenay, S., Peacock, S.M. (2002), An inverted continental Moho and serpentinization of the forearc mantle. Nature. 417: 536-538, doi:10.1038/417536a

Bostock, M.G. (2013), The Moho in subduction zones. Tectonophysics. 609: 547-557, doi:10.1016/j.tecto.2012.07.007

Bostock, M.G., Christensen, N.I., Peacock, S.M. (2019), Seismicity in Cascadia. Lithos. 332: 55-66, doi:10.1016/j.lithos.2019.02.019Boyarko, D.C. and Brudzinski, M.R. (2010), Spatial and temporal patterns of nonvolcanic tremor along the southern Cascadia subduction zone. Journal of Geophysical Research-Solid Earth. 115, B00A22, doi:10.1029/2008JB006064

Breiman, L. (2001), Random Forests. Machine Learning. 45: 5-32,doi:10.1023/A:1010933404324

Brocher, T.M., Parsons, T., Trehu, A.M., Snelson, C.M., Fisher, M.A. (2003), Seismic evidence for widespread serpentinized forearc upper mantle along the Cascadia margin. Geology. 31: 267-270, doi:10.1130/0091-7613

Brudzinski, M.R. and Allen, R.M. (2007), Segmentation in episodic tremor and slip all along Cascadia. Geology. 35(10): 907-910, doi:10.1130/G23740A.1

Brudzinski, M., Cabral-Cano, E., Correa-Mora, F., Demets, C., Marquez-Azua, B. (2007), Slow slip transients along the Oaxaca subduction segment from 1993 to 2007. Geophysical Journal International. 171: 523-538

Brudzinski, M.R., Schlanser, K.M., Kelly, N.J., et al. (2016), Tectonic tremor and slow slip along the northwestern section of the Mexico subduction zone. Earth and Planetary Science Letters. 454: 259-271

Bürgmann, R. (2018), The geophysics, geology and mechanics of slow fault slip. Earth and Planetary Science Letters. 495: 112-134

Calvert, A.J. (2004), Seismic reflection imaging of two megathrust shear zones in the northern Cascadia subduction zone. Nature. 428(6979): 163-167, doi:10.1038/nature02372

Calvert, A.J., Preston, L.A. Farahbod, A.M. (2011), Sedimentary underplating at the Cascadia mantle-wedge corner revealed by seismic imaging. Nat. Geosci. 4: 545-548, doi:10.1038/ngeo1195

Calvert, A.J., Bostock, M.G., Savard, G., Unsworth, M.J. (2020), Cascadia low frequency earthquakes at the base of an overpressured subduction shear zone. Nature communications. 11(3874), doi:10.1038/s41467-020-17609-3

Cassidy, J.F. and Ellis, R.M. (1993), S-wave velocity structure of the northern Cascadia subduction zone. J. Geophys. Res.-Solid Earth. 98(B3): 4407-4421, doi:10.1029/92JB02696

Chawla, N.V., Bowyer, K.W., Hall, L.O., Kegelmeyer, W.P. (2002), SMOTE: Synthetic minority over-sampling technique. Journal of Artificial Intelligence Research. 16: 321-357

Chouet, B.A. (1996), Long-period volcano seismicity: its source and use in eruption forecasting, Nature. 380: 309-316, doi:10.1038/380309a0

Christensen, N.I. (2004), Serpentinites, peridotites, and seismology. International Geology Review. 46(9): 795-816, doi:10.2747/0020-6814.46.9.795

Clayton, R.W. and Wiggins, R.A. (1976), Source shape estimation and deconvolution of teleseismic body-waves. Geophysical Journal of the Royal Astronomical Society. 47(1): 151-177, doi:10.1111/j.1365-246X.1976.tb01267.x

Condit, C.B., Guevara, V.E., Delph, J.R., French, M.E. (2020), Slab dehydration in warm subduction zones at depths of episodic slip and tremor. Earth and Planetary Science Letters. 552, 116601, doi:10.1016/j.epsl.2020.116601

Connolly, J.A.D. (1997), Devolatization-generated fluid pressure and deformation-propagated fluid flow during prograde regional metamorphism. Journal of Geophysical Research. 102: 18149-18173, doi:10.1029/97JB00731

Connolly, J.A.D. (2009), The geodynamic equation of state: What and how. Geochemistry, Geoophysics, Geosystems. 10(10), doi:10.1029/2009GSC002540

Cooper, G.F. and Herskovits, E. (1992), A Bayesian method for the induction of probabilistic networks from data. Machine Learning. 9(4): 309-347

Cortes, C. and Vapnik, V. (1995), Support-vector networks. Machine Learning. 20(3): 273-297

Cover, T. and Hart, P. (1967), Nearest neighbor pattern classification. IEEE Transactions on Information Theory. 13(1): 21-27

Cox, D.R. (1958), The Regression Analysis of Binary Sequences. Journal of the Royal Statistical Society. Series B (Methodological). 20(2): 215-242

Currie, C.A., Hyndman, R.D., Wang, K., Kostoglodov, V. (2004), The thermal effects of steady-state slab-driven flow above a subducting plate: the Cascadia subduction zone and backarc. Earth and Planetary Science Letters. 223: 35-48, doi:10.1016/j.epsl.2004.04.020

Currie, C.A. and Hyndman, R.D. (2006), The thermal structure of subduction zone back arcs. J Geophys. Res. 111, B08404, doi:10.1029/2005JB004024

Davis, E.E., Hyndman, R.D., Villinger, H. (1990), Rates of fluid explusion across the northern Cascadia accretionary prism constraints from new heat flow and multichannel seismic reflection data. Journal of Geophysical Research. 95(B6): 8869-8889, doi:10.1029/JB095iB06p08869

Davis, E.E., Wang, K., He, J., Chapman, D.S., Villinger, H., Rosenberger, A. (1997), An unequivocal case for high Nusselt number hydrothermal convection in sediment-buried igneous oceanic crust. Earth and Planetary Science Letters. 146: 137-150

Dieterich, J.H. (1979), Modeling of rock friction .1. Experimental results and constitutive equations. Journal of Geophysical Research. 94(NB5): 2161-2168, doi:10.1029/JB084iB05p02161

Dieterich, T.G. (2000), Ensemble methods in machine learning. Multiple Classifier Systems. 1857: 1-15

Dai, H.C. and MacBeth, C. (1997), The application of back-propagation neural network to automatic picking seismic arrivals from single-component recordings. Journal of Geophysical Research-Solid Earth. 102(B7): 15105-15113

Davies, J.H. and Stevenson, D.J. (1992), Physical model of source region of subduction zone volcanics. J, Geophys. Res. 97: 2037-2070

Delph, J.R., Levander, A., Niu, F. (2018), Fluid Controls on the Heterogeneous Seismic Characteristics of the Cascadia Margin. Geophysical Research Letters. 45(20): 11021-11029, doi:10.1029/2018GL079518

Dick, H.J.B, Natland, J.H., Alt, J.C., Bach, W., Bideau, D., et al. (2000), A long in situ section of the lower ocean crust: results of ODP Let 176 drilling at the Southwest Indian Ridge. Earth and Planetary Science Letters. 179(1): 31-51, doi:10.1016/S0012-821X(00)00102-3

Dragert, H., Wang, K.L., James, T.S. (2001), A silent slip event on the deeper Cascadia subduction interface. Science. 292(5521): 1525-1528

Dragert, H., Wang, K., Rogers, G. (2004), Geodetic and seismic signatures of episodic tremor and slip in the northern Cascadia subduction zone. Earth Planets and Space. 56(12):1143-1150

Fagereng, A. and Diener, J.A. (2011), Non-volcanic tremor and discontinuous slab dehydration. Geophysical Research Letters. 38(15), doi:10.1029/2011GL048214

Fagereng, A., Diener, J.A., Meneghini, F., Harris, C., Kvadsheim, A. (2018), Quartz vein formation by local dehydration embrittlement along the deep, tremorgenic subduction thrust interface. Geology. 46(1): 67-70, doi:10.1130/G39649.1

Farge, G., Jaupart, C., Shapiro, N.M. (2021), Episodicity ad Migration of Low Frequency Earthquakes Modeled With Fast Fluid Pressure Transients in the Permeable Subduction Interface. Journal of Geophysical Research: Solid Earth. 126(9), doi:10.1029/2021JB021894

Feng, L., Hill, E.M., Elosegui, P., Qiu, Q., Hermawan, I., Banerjee, P., Sieh, K. (2015), Hunt for slow slip events along the Sumatran subduction zone in a decade of continuous GPS data. Journal of Geophysical Research: Solid Earth. 120: 8623-8632

Fisher, R.A. (1912), On an absolute criterion for fitting frequency curves. Messenger of Mathematics. 41: 144-160

Fisher, R.A. (1936), The use of multiple measurements in taxonomic problems. Annals of human genetics. 7(2): 179-188

Fix, E. and Hodges, J.L. (1951), Discriminatory analysis, nonparametric discrimination: Consistency properties. Technical Report 4, USAF School of Aviation Medicine, Randolph Field, Texas.

Flueh, E.R., et al. (1998), New seismic images of the Cascadia subduction zone from cruise SO108-ORWELL. Tectonophysics. 293: 69-84

Frank, W.B., Shapiro, N.M., Husker, A.L., Kostoglodov, V., Bhat, H.S., Campillo, M. (2015), Along-fault pore-pressure evolution during a slow-slip event in Guerrero, Mexico. Earth Planet. Sci. Lett., 413: 135-143, doi:10.1016/j.epsl.2014.12.051

Frederiksen, A.W., Folsom, H., Zandt, G. (2003), Neighbourhood inversion of teleseismic Ps conversion for anisotropy and layer dip. Geophysical Journal International. 155: 200-212

Fu, Y. and Freymueller, J.T. (2013), Repeated large Slow Slip Events at the southcentral Alaska subduction zone. Earth and Planetary Science Letters. 375: 303-311

Gallego, A., Russo, R.M., Comte, D., Mocanu, V., Murdie, R.E., Vandecar, J.C. (2013), Tidal modulation of continuous nonvolcanic seismic tremor in the Chile triple junction region. Geochemistry Geophysics Geosystems. 14(4): 851-863

Gao, X. and Wang, K. (2014), Strength of stick-slip and creeping subducting megathrusts from heat flow observations. Science. 345 (1038), doi:10.1126/science.1255487

Gao, X., and Wang, K. (2017), Rheological separation of the megathrust seismogenic zone and episodic tremor and slip, Nature, 543, 416-419.

Graham, S., DeMets, C., Cabral-Cano, E., Kostoglodov, V., Rousset, B., Walpersdorf, A., Cotte, N., Lasserre, C., McCaffrey, R., Salazar-Tlaczani, L. (2015), Slow Slip History for the Mexico Subduction Zone: 2005 Through 2001. Pure Applied Geophysics. 173: 3445-3465

Gentili, S. and Michelini, A. (2006), Automatic picking of P and S phases using a neural tree. Journal of Seismology. 10(1): 39-63

Gosselin, J.M., Audet, P., Esteve, C., McLellan, M. Mosher, S.G. (2020), Seismic evidence for megathrust fault-valve behavior during episodic tremor and slip. Science Advances. 6(4), doi:10.1126/sciadv.aay5174

Gripp, A.E. and Gordon, R.G. (2002), Young tracks of hotspots and current plate velocities. 150(2): 321-361

Guiraud, M., Powell, R., Rebay, G. (2001), H_2O in metamorphism and unexpected behaviour in the preservation of metamorphic mineral assemblages. Journal of Metamorphic Geology. 19(4): 445-454, doi:10.1046/j.0263-4929.2001.00320.x

Hacker, B.R., Abers, G.A., Peacock, S.M. (2003), Subduction factory 1: Theoretical mineralogy, density, seismic wave speeds, and H2O content. J. Geophys. Res. Doi:10.1029/2001JB001127

Hacker, B.R., Peacock, S.M., Abers, G.A., Holloway, S.D. (2003), Subduction factory 2: Are intermediate-depth earthquakes in subducting slabs linked to metamorphic dehydration reactions? J. Geophys. Res. 108, doi:10.1029/2001JB001129

Hacker, B. (2008), H_2O subduction beyond arcs. Geochemistry, Geophysics, Geosystems. 9(3), doi:10.1029/2007GC001707

Hansen, R.T.J., Bostock, M.H., Christensen, N.I. (2012), Nature of the low velocity zone in Cascadia from receiver function waveform inversion. Earth Planet. Sci. Lett. 337-338: 25-38, doi:10.1016/j.epsl.2012.05.031

Harris, R.N., Spinelli, G., Ranero, C.R., Grevemeyer, I., Villinger, H., Barckhausen, U. (2010), Thermal regime of the Costa Rican convergent margin: 2. Thermal models of the shallow Middle America subducting zone offshore Costa Rica. Geochemistry, Geophysics, Geosystems. 11, doi:10.1029/2010GC003273

Hawkins, D.M. (2004), The Problem of Overfitting. Journal of Chemical Information and Computer Sciences. 44(1): 1-12

Hayes, G.P., Moore, G.L., Portner, D.E., Hearne, M., Flamme, H., Furtney, M., Smoczyk, G.M. (2018), Slab2, a comprehensive subduction zone geometry model. Science. 362(6410): 58-61

Hirose, H., Hirahara, K., Kimata, F., Fujii, N., Miyazaki, S. (1999), A slow thrust slip event following the two 1996 Hyuganada earthquakes beneath the Bungo Channel, southwest Japan. Geophysical Research Letters. 26(21): 3237-3240

Hirose, H. and Obara, K., (2005), Repeating short- and long-term slow slip events with deep tremor activity around the Bungo channel region, southwest Japan. Earth Planets Space. 57: 961-972

Ho, T.K. (1998), The random subspace method for constructing decision forests. IEEE Transactions on Pattern Analysis and Machine Intelligence. 20(8): 832-844.

Holland, T.J.B and Powell, R. (1998), An internally consistent thermodynamic data set for pahses of petrologic interest. J. Metamorph. Geol. 16: 309-343, doi:10.1111/j.1525.1314.1998.00140.x.

Hoover, W,F., Penniston-Dorland, S., Baumgartner, L., Bouvier, A., Dragovic, B., Locatelli, M., Angiboust, S., Agard, P. (2022), Episodic fluid flow in an eclogite-facies shear zone: Insights from Li isotope zoning in garnet. Geology, 50(6): 746-750, doi:10.1130/G49737.1

Husker, A.L., Kostoglodov, V., Cruz-Atienza,V.M., Legrand, D., Shapiro, N.M., Payero, J.S., Campillo, M., Huesca-Perez, E. (2012), Temporal variations of non-volcanic tremor (NVT) locations in the Mexican subduction zone: Finding the NVT sweet spot. Geochemistry Geophysics Geosystems. 13: Q03011

Husker, A., Frank, W.B., Gonzalez, G., Avila, L., Kostoglodov, V., Kazachkina, E. (2019), Characteristic Tectonic Tremor Activity Observed Over Multiple Slow Slip Cycles in the Mexican Subduction Zone. Journal of Geophysical Research-Solid Earth. 124(1): 599-608

Hyndman, R.D. and Wang, K., (1993), Thermal Constraints on the Zone of Major Thrust Earthquake Failure: The Cascadia Subduction Zone. Journal of Geophysical Research. 98(B2): 2039-2060

Hyndman, R.D., Wang, K., Yuan, T., Spence, G.D. (1993), Tectonic sediment thickening, fluid expulsion, and the thermal regime of subduction zone accretionary prisms: The Cascadia margin off Vancouver Island. Journal of Geophysical Research. 98(B12): 21865-21876, doi:10.1029/93JB02391

Hyndman, R. and Peacock, S. (2003), Serpentinization of the forearc mantle. Earth and Planetary Science Letters. 212: 417-432

Hyndman, R.D. (2013), Downdip landward limit of Cascadia great earthquake rupture. Journal of Geophysical Research: Solid Earth. 118(10): 5530-5549, doi:10.1002/jgrb.50390

Hyndman, R.D., McCrory, PA., Wech, A., Kao, H., Ague, J. (2015), Cascadia subducting plate fluids channeled to fore-arc mantle corner: ETS and silica deposition. J. Geophys. Res. 120: 4344-4358

Ide, S. (2012), Variety and spatial heterogeneity of tectonic tremor worldwide. Journal of Geophysical Research-Solid Earth. 117: B03302

Jarrard, R.D. (1986), Relations among subduction parameters, Rev. geophys. 24(2), 217-283

Jiang, Y., Liu, Z., Davis, E.E., et al. (2017), Strain release at the trench during shallow slow slip: The example of Nicoya Peninsula, Costa Rica. Geophysical Research Letters. 44(10): 4846-4854.

Jolivet, R. and Frank, W.B. (2020), The transient and intermittent Nature of Slow Slip. AGU Advances. 1, e2019AV000126, doi:10.1029/2019AV000126

Kanamori, H. (1972), Relation between tectonic stress, great earthquakes and earthquake swarms. Tectonophysics. 14(1), doi:10.1016/0040-1951(72)90002-9

Kanamori, H. and Stewart, G.S. (1979), Slow earthquake. Physics of the Earth and Planetary Interiors. 18(3): 167-175, doi:10.1016/0031-9201(79)90112-2

Karato, S. and Wu, P. (1993), Rheology of the upper mantle-A synthesis. Science. 260(5109): 771-778

Katayama, I., Hirauchi, K., Michibayashi, K., Ando, J. (2009), Trench-parallel anisotropy produced by serpentine deformation in the hydrated mantle wedge. Nature. 461: 1114-1117, doi:10.1038/nature08513

Katayama, I., Terada, T., Okazaki, K., Tanikawa, W. (2012), Episodic tremor and slow slip potentially linked to permeability contrasts at the Moho. Nature Geoscience. 5: 731-734

Kato, A., Iidaka, T., Ikuta, R., Yoshida, Y., Katsumata, K., Iwasaki, T., Sakai, S., Thurber, C., Tsumura, N., Yamaoka, K., Watanabe, T., Kunitomo, T., Yamazaki, F., Okuba, M., Suzuki, S., Hirata, N. (2010), Variations of fluid pressure within the subducting oceanic crust and slow earthquakes. Geophysical Research Letters. 37: L14310

Kaufl, P., Valentine, A., Trampert, J. (2016), Probabilistic point source inversion of strong-motion data in 3-D media using pattern recognition: A case study for the 2008 M-w 5.4 Chino Hills earthquake. Geophysical Research Letters. 43(16): 8492-8498

Kawano, S., Katayama, I., Okazaki, K. (2011), Permeability anisotropy of serpentinite and fluid pathways in a subduction zone. Geology. 39: 939-942, doi:10.1130/G32173.1

Kennett, B. and Engdahl, E. (1991), Travel times for global earthquake location and phase identification. Geophysical Journal International. 122(1): 108-124

Kent, A., Berry, M., Luehrs, F., Perry, J.W. (1955), Machine literature searching VIII. Operational critieria for designing information retrieval systems. American Documentation. 6(2): 93

Kincaid, C. and Sacks, I.S. (1997), Thermal and dynamical evolution of the upper mantle in subduction zones. J. Geophys. Res. 102: 12295-12315

Kirby, S.H. (1983), Rheology of the lithosphere. Review of Geophysics. 21(6): 1458-1487, doi:10.1029/RG021i006p01458

Klein, E., Duputel, Z., Zigone, D., Vigny, C., Boy, J.P., Doubre, C., Meneses, G. (2018), Deep Transient Slow Slip Detected by Survey GPS in the Region of Atacama, Chile. Geophysical Research Letters. 45(12): 263-273

Kobayashi, A. (2014), A long-term slow slip event from 1996-1997 in the Kii Channel, Japan. Earth, Planets and Space. 66(9), doi:10.1186/1880-5981-66-9

Kobayashi, A. (2017), Objective detection of long-term slow slip events along the Nankai Trough using GNSS data (1996-2016). Earth Planets and Space. 69(171)

Kostoglodov, V., Singh, S.K., Santiago, J.A., Franco, S.I., Larson, K.M., Lowry, A.R. (2003), A large silent earthquake in the Guerrero seismic gap, Mexico. Geophysical Research Letters. 30(15): 1807

Kuhn, S., Cracknell, M.J., Reading, A.M. (2018), Lithologic mapping using Random Forests applied to geophysical and remote-sensing data: A demonstration study from the Eastern Goldfields of Australia. Geophysics. 83(4): B183-B193

Kumazawa, M. (1969), The elastic constants of single-crystal orthopyroxene. J. Geophys. Res. 74: 5973-5980

Kumazawa, M. and Anderson, O.L. (1969), Elastic moduli, pressure derivatives, and temperature derivatives of single-crystal olivine and single-crystal forsterite. J. Geophys. Res. 74 (25): 5961-5972

Langston, C.A. (1979), Structure under Mount Rainier, Washington, inferred from teleseismic body waves, Journal of Geophysical ResearchL Solid Earth, 84(B9), 4749-4762

Lewis, T.J., Bentkowski, W.H., Davis, E.E., Hyndman, R.D., Wright, J.A. (1988), Subduction of the Juan de Fuca plate: Thermal consequences. Journal of Geophysical Research. 93(B12): 15207-15225, doi:10.1029/JB093iB12p15207

Li, D. and Liu, Y. (2016), Spatiotemporal evolution of slow slip events in a nonplanar fault model for northern Cascadia subduction zone. Journal of Geophysical Research: Solid Earth.121: 6828-6845, doi:10/1002/2016JB012857

Linde, A.T., Gladwin, M.T., Johnston, M.J.S., Gwyther, R.L., Bilham, R.G. (1996), A slow earthquake sequence on the San Andreas fault. Nature. 383: 65-68, doi:10.1038/383065a0

Liu, Y. and Rice, J.R. (2007), Spontaneous and triggered aseismic deformation transients in a subduction fault model. J. Geophys. Res. 112, B09404, doi:10/1029/2007JB004930

Liu, Y., and Rubin, A.M. (2010), Role of fault gouge dilatancy on aseismic deformation transients, Journal of Geophysical Research, 115, B10414.

Liu, Y.J. (2013), Numerical simulations on megathrust rupture stabilized under strong dilatancy strengthening in slow slip region. Geophysical Research Letters. 40(7), doi:10.1002/grl.50298

Long, M. D. & van der Hilst, R. D. (2006), Shear wave splitting from local events beneath the Ryukyu arc: trench-parallel anisotropy in the mantle wedge. *Phys. Earth Planet. Inter.* **155**: 300–312

Lowry, A.R., Larson, K.M., Kostoglodov, V., Bilham, R. (2001), Transient fault slip in Guerrero, southern Mexico. Geophys. Res. Lett. 28: 3753-3756

Maury, J., Ide, S., Cruz-Atienza, V.M., Kostoglodov, V. (2018), Spatiotemporal Variations in Slow Earthquakes Along the Mexican Subduction Zone. Journal of Geophysical Research: Sold Earth. 123: 1559-1575

McCaffrey, R., Wallace, L.M., and Beavan, J. (2008), Slow slip and frictional transition at low temperature at the Hikurangi subduction zone. Nature Geoscience. 1: 316-320, doi:10.1038/ngeo178

McCrory, P.A., Blair, J.L., Waldhauser, F., Oppenheimer, D.H. (2012), Juan de Fuca slab geometry and its relation to Wadati-Benioff zone seismicity. Journal of Geophysical Research: Solid Earth. 117(B9), doi:10.1029/2012JB009407

McCrory, P.A., Hyndman, R.D., Blair, J.L. (2014), Relationship between the Cascadia fore-arc mantle wedge, nonvolcanic tremor, and the downdip limit of seismogenic rupture. Geochemistry, Geophysics, Geosystems. 1071-1095, doi:10.1002/2013GC005144

McKenzie, D.P. (1969), Speculations on the consequences and causes of plate motions, Geophys. J. Int. RAS 18: 1-32

McLellan, M. and Audet, P. (2020), Uncovering the physical controls of deep subduction zone slow slip using supervised classification of subducting plate features. Geophysical Journal International. 223(1): 94-110, doi:10.1093/gji/ggaa285

McLellan, M., Audet, P., Rosas, J.C., Currie, C. (2022), Margin-wide variations in slab dehydration in Cascadia and their relationship to slow slip. Lithos. 434, doi:10.1016/j.lithos.2022.106912

Melbourne, T.I., Szeliga, W.M., Miller, M.M., Santillan, V.M. (2005), Extent and duration of the 2003 Cascadia slow earthquake. Geophysical Research Letters. 32(4): L04301

Meltzner, A.J., Sieh, K., Chiang, H.W., Wu, C.C., Tsang, L.L.H., Shen, C.C., Hill, E.M., Suwargadi, B.W., Natawidjaja, D.H., Philibosian, B., Briggs, R.W. (2015), Time-varying interseismic strain rates and similar seismic ruptures on the Nias-Simeulue patch of the Sunda megathrust. Quaternary Science Reviews. 122: 258-281

Miller, M.M., Melbourne, T., Johnson, D.J. Sumner, W.Q. (2002), Periodic slow earthquakes from the Cascadia subduction zone. Science. 295(5564): 2423-2423

Mousavi, S.M., Horton, S.P., Langston, C.A., Samei, B. (2016), Seismic features and automatic discrimination of deep and shallow induced-microearthquakes using neural network and logistic regression. Geophysical Journal International. 207(1): 29-46

Mueller, R. D., Sdrolias, M., Gaina, C., Roest, W.R. (2008), Age, spreading rates, and spreading asymmetry of the world's ocean crust. Geochemistry Geophysics Geosystems. 9: Q04006

Nakajima, J. and Uchida, N. (2018), Repeated drainage from megathrusts during episodic slow slip. Nat. Geosci. 11: 351-356

Nedimovic, M.R., Hyndman, R.D., Ramachandran, K., Spence, G.D. (2003), Reflection signature of seismic and aseismic slip on the northern Cascadia subduction interface. 424(6947): 416-420, doi:10.1038/nature01840

Nicholson, T., Bostock, M., Cassidy, J.F. (2005), New constraints on subduction zone structure in northern Cascadia. Geophysical Journal International. 161(3): 849-859, doi:10.1111/j.1365-246X.2005.02605.x

Nikulin, A., Levin, V., Park, J. (2009), Receiver function study of the Cascadia megathrust: Evidence for localized serpentinization. Geochemistry Geophysics Geosystems. 10, Q07004, doi:10.1029/2009GC002376

Nishimura, T., Matsuzawa, T., and Obara, K. (2013), Detection of short-term slow slip events along the Nankai Trough, southwest Japan, using GNSS data. Journal of Geophysical Research: Solid Earth. 118: 3112-3125

Nishimura, T. (2014), Short-term slow slip events along the Ryukyu trench, southwestern Japan, observed by continuous GNSS. Progress in Earth and Planetary Science. 1: 22

Obara, K. (2002), Nonvolcanic deep tremor associated with subduction in southwest Japan. Science. 296(5573): 1679-1681, doi:10.1126/science.1070378

Obara, K. and Kato, A. (2016) Connecting slow earthquakes to huge earthquakes. Science. 353(6296): 253-257.

Ohta, Y., Freymueller, J.T., Hreinsdottir, S., Suito, H. (2006), A large slow slip event and the depth of the seismogenic zone in the south-central Alaska subduction zone. Earth and Planetary Science Letters. 257(1-2): 108-116

Okazaki, K., Katayama, I., Noda, H. (2013), Shear-induced permeability anisotropy of simulated serpentinite gouge produced by triaxial deformation experiments. Geophys. Res. Lett. 40: 1290-1294, doi:10.1002/grl.50302

Outerbridge, K.C., Dixon, T.H., Schwartz, S.Y., Walter, J.I., Protti, M., Gonzalez, V., Biggs, J., Thorwart, M. Rabbel, W. (2010), A tremor and slip event on the Cocos-Caribbean subduction zone as measured by a global positioning system (GPS) and seismic network on the Nicoya Peninsula, Costa Rica. Journal of Geophysical Research: Solid Earth. 115(B10), doi:10.1029/2009JB006845

Ozawa, S., Murakami, M., Kaidzu, M., Tada, T, Hatanaka, Y., Yarai, H., Nishimura, T. (2002), Detection and monitoring of ongoing aseismic slip in the Tokai region, central Japan. Science. 298: 1009-1012, doi:10.1126/science.1076780

Ozawa, S., Miyazaki, S., Hatanaka, Y., Imakiire, T., Kaidzu, M., Murakami, M. (2003), Characteristic silent erathquakes in the eastern part of the Boso Peninsula, central Japan. Geophys. Res. Lett. 30(6), 1283, doi:10.1029/2002GL016665

Ozawa, S. (2017). Long-term slow slip events along the Nankai trough subduction zone after the 2011 Tohoku earthquake in Japan. Earth Planets and Space. 69(56)

Panakkat, A., Adeli, H. (2009), Recurrent Neural Network for Approximate Earthquake Time and Location Prediction Using Multiple Seismicity Indicators. Computer-Aided Civil and Infrastructure Engineering. 24(4): 280-292

Peacock, S.M. (1990), Fluid Processes in Subduction Zones. Science. 248(4953): 329-337.

Peacock, S.M. (2009), Thermal and metamorphic environment of subduction zone episodic tremor and slip. Journal of Geophysical Research-Solid Earth. 114, B00A07, doi:10.1029/2008JB005978

Peacock, S.M., Christensen, N.I., Bostock, M.G., Audet, P. (2011), High pore pressures and porosity at 35 km depth in the Cascadia subduction zone. Geology. 39(5): 471-474

Peacock, S.M. (2020), Advances in the thermal and petrologic modeling of subduction zone. Geosphere. 16(4): 936-952, doi:10/1130/GES02213.1

Pearce, J.A. (1976), Statistical analysis of major element patterns in basalt. J. Petrol. 17: 15-43

Perry, M., Spinelli, G.A., Wada, I., He, J. (2016), Modeled temperatures and fluid source distributions for the Mexican subduction zone: Effects of hydrothermal circulation and implications for plate boundary seismic processes. Geochemistry, Geophysics, Geosystems. 17: 550-570, doi:10.1002/2015GC006148

Peterson, C., McNutt, S., Christensen, D. (2011), Nonvolcanic Tremor in the Aleutian Arc. Bulletin of the Seismological Society of America. 101(6): 3081-3087, doi:10.1785/0120100241

Plank, T. and Langmuir, C.H. (1998), Chemical composition of bottom sediments at DSDP Sites 91-595 and 91-596 and ODP Sites 114-701 and 129-801. PANGAEA. doi:10.1594/PANGAEA.706145

Preston, L.A., Creager, K.C., Crosson, R.S., Brocher, T.M., Trehu, A.M. (2003), Intraslab earthquakes: dehydration of the Cascadia slab. Science. 302: 1997-1200

Radiguet, M., Cotton, F., Vergnolle, M., Campillo, M., Walpersdorf, A., Cotte, N., Kostoglodov, V. (2012), Slow slip events and strain accumulation in the Guerrero gap, Mexico. Journal of Geophysical Research. 117: B04305

Ramachandran, K., Dosso, S.E., Spence, G.D., Hyndman, R.D., Brocher, T.M. (2005), Forearc structure beneath southwestern British Columbia: A three-dimensional tomographic velocity model. Journal of Geophysical Research-Solid Earth. 110(B2), B02303, doi:10.1029/2004JB003258

Reinen, L.A., Weeks, T.E., Tullis, T.E. (1991), The frictional behavior of serpentinite: Implications for aseismic creep on shallow crustal faults. Geophs. Res. Lett. 18: 1921-1924

Reynard, B. (2013), Serpentine in active subduction zones. Lithos. 178: 171-185, doi:10.1016/j.lithos.2012.10.012

Reynen, A. and Audet, P. (2017), Supervised machine learning on a network: application to seismic event classification and detection. Geophysical Journal International. 210(3): 1394-1409

Rogers, G. and Dragert, H. (2003), Episodic tremor and slip on the Cascadia subduction zone: The chatter of silent slip. Science. 300(5627): 1942-1943

Rosas, J.C., Currie, C.A., Harris, R.N., He, J. (2016), Effect of hydrothermal circulation on slab dehydration for the subduction zone of Costa Rica and Nicaragua. Physics of the Earth and Planetary Interiors. 225: 66-79, doi:10.1016/j.pepi.2016.03.009

Rousset, B., Campillo, M., Lasserre, C., Frank, W.B., Cotte, N., Walpersdorf, A., Socquet, A., Kostoglodov, V. (2017), A geodetic matched filter search for slow slip with application to the Mexico subduction zone. Journal of Geophysical Research-Solid Earth. 122(12): 10498-10514

Ruina, A. (1983), Slip instability and state variable friction laws. Journal of Geophysical Research. 88(NB12): 359-370, doi:10.1029/JB088iB12p10359

Ruiz, S., Metois, M., Fuenzalida, A., Ruiz, J., Leyton, F., Grandin, R., Vigny, C., Madariaga, R., Campos., J. (2014), Intense foreshocks and a slow slip event preceded the 2014 Iquique M_w 8.1 earthquake. Science. 345(6201): 1165-1169

Savard, G., Bostock, M.G., Christensen, N.I. (2018), Seismicity, Metamorphism, and Fluid Evolution Across the Northern Cascadia Fore Arc. Geochemistry, Geophysics, Geosystems. 19: 1881-1897, doi:10.1029/2017GC007417

Schmidt, D.A. and Gao, H. (2010), Source parameters and time-dependent slip distributions of slow slip events on the Cascadia subduction zone from 1998 to 2008. Journal of Geophysical Research. 115: B00A18

Scholz, C.H. (1998), Earthquakes and friction laws. Nature. 391: 37-42, doi:10.1038/34097

Schwartz, S.Y. and Rokosky, J.M. (2007), Slow slip events and seismic tremor at circum-Pacific subduction zones. Rev. Geophys. 45

Scuderi, M. M. and Carpenter B.M. (2022), Frictional stability and hydromechanical coupling of serpentinite-bearing fault gouge. Geophysical Journal International. 231(1): 290-305, doi:10.1093/gji/ggac188

Segall, P., Rubin, A.M., Bradley, A.M., and Rice, J.R. (2010), Dilatant strengthening as a mechanism for slow slip events. Journal of Geophysical Research, 115, B12305.

Sekine, S., Hirose, H., and Obara, K. (2010), Along-strike variations in short-term slow slip events in the southwest Japan subduction zone, Journal of Geophysical Research: Solid Earth. 115: B00A27

Shahnas, M.H., Yuen, D.A., Pysklywec, R.N. (2018), Inverse Problems in Geodynamics Using Machine Learning Algorithms. Journal of Geophysical Research-Solid Earth, 123(1): 296-310

Shelly, D.R. (2017), A 15 year catalog of more than 1 million low-frequency earthquakes: tracking tremor and slip along the deep San Andreas Fault. Journal of Geophysical Research: Solid Earth. 122: 3739-3753, doi:10.1002/2017JB014047

Smith, G. P. et al. (2001), A complex pattern of mantle flow in the Lau backarc. Science 292: 713–716

Socquet, A., Valdes, J.P., Jara, J., Cotton, F., Walpersdorf., A., Cotte, N., Specht, S., Ortega-Culaciati, F., Carrizo, D., and Norabuena, E. (2017), An 8 month slow slip event triggers

progressive nucleation of the 2014 Chile megathrust. Geophysical Research Letters. 44(9): 4046-4053

Song, T. and Kim, Y. (2012), Localized seismic anisotropy associated with long-term slow-slip events beneath southern Mexico. Geophysical Research Letters. 39(9), doi:10.1029/2012GL051324

Spinelli, G., Wada, I., Wang, K., He, J., Harris, R., Underwood, M. (2018), Diagenetic, metamorphic, and hydrogeologic consequence of hydrothermal circulation in subducting crust. Geosphere. 14(6): 2337-2354, doi:10.1130/GES01653.1

Stein, C.A. and Stein, S. (1992), A model for the global variation in oceanic depth and heat flow with lithospheric age. Nature. 359: 123-129, doi:10.1038/359123a0

Stern, R.J. (2002), Subduction zones. Reviews of Geophysics. 40(4), 1012, doi:10.1020/2001RG000108

Stone, I., Vidale, J.E., Han, S.S., Roland, E. (2018), Catalog of Offshore Seismicity in Cascadia: Insights Into the Regional Distribution of Microseismicity and its Relation to Subduction Processes. Journal of Geophysical Research-Solid Earth. 123(1): 641-652, doi:10.1002/2017JB014966

Suito, H. and Ozawa, S. (2009), Transient crustal deformation in the Tokai district. J. Seismol. Soc. Jpn. 69: 113-135

Takagi, R., Obara, K., Maeda, T. (2016), Slow slip event within a gap between tremor and locked zones in the Nankai subduction zone. Geophysical Research Letters. 42(3): 1066:1074, doi:10.1002/2015GL066987

Tanaka, Y., Suzuki, T., Imanishi, Y., Okubo, S., et al. (2018), Temporal gravity anomalies observed in the Tokai area and a possible relationship with slow slips. Earth, Planets and Space. 70(25), doi:10.1186/s40623-018-0797-5

Taetz, S., John, T., Brocker, M., Spandler, C., Stracke, A. (2018), Fast intraslab fluid-flow events linked to pusles of high pore fluid pressure at the subducted plate interface. Earth and Planetary Science Letter. 482: 33-43, doi:10.1016/j.epsl.2017.10.044

Tenthorey, E. and Cox, S.F. (2003), Reaction-enhanced permeability during serpentine dehydration. Geology. 31(10): 921-924, doi:10.1130/G19724.1

Todd, E.K., Schwartz, S.Y. (2016), Tectonic tremor along the northern Hikurangi Margin, New Zealand, between 2010 and 2015. Journal of Geophysical Research-Solid Earth. 121(12): 8706-8719

Trehu, A.M., Asudeh, I., Brocher, T.M., Luetgert, J.H., Mooney, W.D., Nabelek, J.L., Nakamura, Y. (1994), Crustal architecture of the Cascadia forearc. Science 266: 237-243.

Tsang, L.L.H., Meltzner, A.J., Philibosian, B., Hill, E.M., Freymueller, J.T., Sieh, K. (2015), A 15 year slow-slip event on the Sunda megathrust offshore Sumatra. Geophysical Research Letters. 42(16): 6630-6638

Ujiie, K., Saishu, H., Fagereng, A., Nishiyama, N., Otsubo, M, Masuyama, H., Kagi, H. (2018), An Explanation of Episodic Tremor and Slow Slip Constrained by Crack-Seal Veins and Viscous

Shear in Subduction Melange. Geophysical Research Letters. 45(11): 5371-5379, doi:10.1029/2019GL078374

Vaca, S., Vallee, M., Nocquet, J.M., et al. (2018), Recurrent slow slip as a barrier to the northward rupture propagation of the 2016 Pedernales earthquake (Central Ecuador). Tectonophysics. 724: 80-92

Vallee, M., Nocquet, J.M, Battaglia, J., et al. (2013), Intense interface seismicity triggered by a shallow slow slip event in the Central Ecuador subduction zone. Journal of Geophysical Research-Solid Earth. 118(6): 2965-2981

van Keken, P.E., Hacker, B.R., Syracuse, E.M., Abers, G.A. (2011), Subducting factory: 4. Depth-dependeth flux of H_2O from subducting slabs worldwide. Journal of Geophysical Research. 116, B01401, doi:10.1029/2010JB007922

Villafuerte, C. and Cruz-Atienza, V.M. (2017), Insights into the causal relationship between slow slip and tectonic tremor in Guerrero, Mexico. Journal of Geophysical Research-Solid Earth. 122(8): 6642-6656

Voss, N.K., Malservisi, R., Dixon, T.H., Protti, M. (2017), Slow slip events in the early part of the earthquake cycle. Journal of Geophysical Research: Solid Earth. 112: 6773-6786

Wada, I. and Wang, K. (2009), Common depth of slab-mantle decoupling: Reconciling diversity and uniformity of subduction zones. Geochemistry Geophysics Geosystems. 10(10), Q10009, doi:10.1029/2009GC002570

Wada, I., M. D. Behn, and A. M. Shaw (2012), Effects of heterogeneous hydration in the incoming plate, slab rehydration, and mantle wedge hydration on slab-derived fluid flux in subduction zones, Earth Planet. Sci. Lett., 353-354, 60-71

Wang, K., Mulder, T., Rogers, G.C., and Hyndman, R.D. (1995), Case for very low coupling stress on the Cascadia subduction fault., J. Geophys. Res. 100(12): 907-12918

Wallace, L.M. and Beavan, J. (2006), A large slow slip event on the central Hikurangi subduction interface beneath the Manuwatu region, North Island, New Zealand. Geophysical Research Letters. 33(11): L11301

Wallace, L. and Beavan, J. (2010), Diverse slow slip behavior at the Hikurangi subduction margin, New Zealand. Journal of Geophysical Research-Solid Earth. 115: B12402

Wallace, L.M., Beavan, J, Bannister, S., Williams, C. (2012), Simultaneous long-term and short-term slow slip events at the Hikurangi subduction margin, New Zealand: Implications for processes that control slow slip event occurrence, duration, and migration. Journal of Geophysical Research. 117: B11402

Wallace, L.M., Eberhart-Phillips, D. (2013), Newly observed, deep slow slip events at the central Hikurangi margin, New Zealand: Implications for downdip variability of slow slip and tremor, and relationship to seismic structure. Geophysical Research Letters. 40: 5393-5398

Wallace, L.M., Kaneko, Y., Hreinsdottir, S., Hamling, I., Peng, Z., Bartlow, N., D'Anastasio, E., Fry, B. (2017), Large-scale dynamic triggering of shallow slip enhanced by overlying sedimentary wedge. 10: 765-770

Wallace, L.M. (2020), Slow Slip Events in New Zealand. Annual Review of Earth and Planetary Sciences. 48: 175-703, doi:10.1146/annurev-earth-071719-055104

Walter, J.I., Schwartz, S.Y., Protti, M., Gonzalez, V. (2013), The synchronous occurrence of shallow tremor and very low frequency earthquakes offshore of the Nicoya Peninsula, Costa Rica. Geophysical Research Letters. 40(8): 1517-1522

Wang, K. and Bilek, S.L. (2014), Invited review paper: Fault creep caused by subduction of rough seafloor relief. Tectonophysics. 610: 1-24

Wang, K. and Trehu, A.M. (2016), Invited review paper: Some outstanding issues in the study of great megathrust earthquakes—The Cascadia example. Journal of Geodynamics.

Wang, J. and Teng, T.L. (1995), Artificial Neural-Network-Based Seismic Detector. Bulletin of the Seismological Society of America. 85(1): 308-319

Warren-Smith, E., Fry, B., Wallace, L., Chon, E., Henrys, S., Sheehan, A., Mochizuki, K., Schwartz, S., Webb, S., Lebedev, S. (2019), Episodic stress and fluid pressure cycling in subducting oceanic crust during slow slip. Nature Geoscience. 12: 475-481, doi:10.1038/s41561-019-0367-x

Wech, A.G. and Creager, K.C. (2008), Automated detection and location of Cascadia tremor. Geophysics Research Letters. 35, L20302, doi:10.1029/2008GL035458

Wech, A. G., Creager, K. C., Melbourne, T. I. (2009), Seismic and geodetic constraints on Cascadia slow slip. Journal of Geophysical Research. 114: B10316

Wech AG, Boese CM, Stern TA, Townend J. (2012), Tectonic tremor and deep slow slip on the alpine fault. Geophys. Res. Lett. 39, L10303, doi:10.1029/2012gl051751

Wech, A.G. (2016), Extending Alaska's plate boundary: Tectonic tremor generated by Yakutat subduction. Geology. 44(7): 587-590.

Wech, A.G. (2021), Cataloging tectonic tremor energy radiation in the Cascadia subduction zone. Journal of Geophysical Research: Solid Earth. doi:10.1029/2021JC022523

Wei, M., McGuire, J.J., Richardson, E. (2012), A slow slip event in the south-central Alaska Subduction Zone and related seismicity anomaly. Geophysical Research Letters. 39: L15309

Wilson, M. (1989), Igneous Petrogenesis: A Global Tectonic Approach. doi.org/10.1007/978-1-4020-6788-4

Wilson, D.S. (1993), Confidence intervals for motion and deformation of the Juan de Fuca plate, J. Geophys. Res. 98: 16053-16071, doi:10.1029/93JB01227

Xiang Y, Sun DY, Fan W, Gong XG. (1997), Generalized Simulated Annealing Algorithm and Its Application to the Thomson Model. Physics Letters A, 233, 216-220

Yabe, S., Ide., S., Yoshioka, S. (2014), Along-strike variations in temperature and tectonic tremor activity along the Hikurangi subduction zone, New Zealand. Earth Planets and Space. 66: 142

APPENDIX

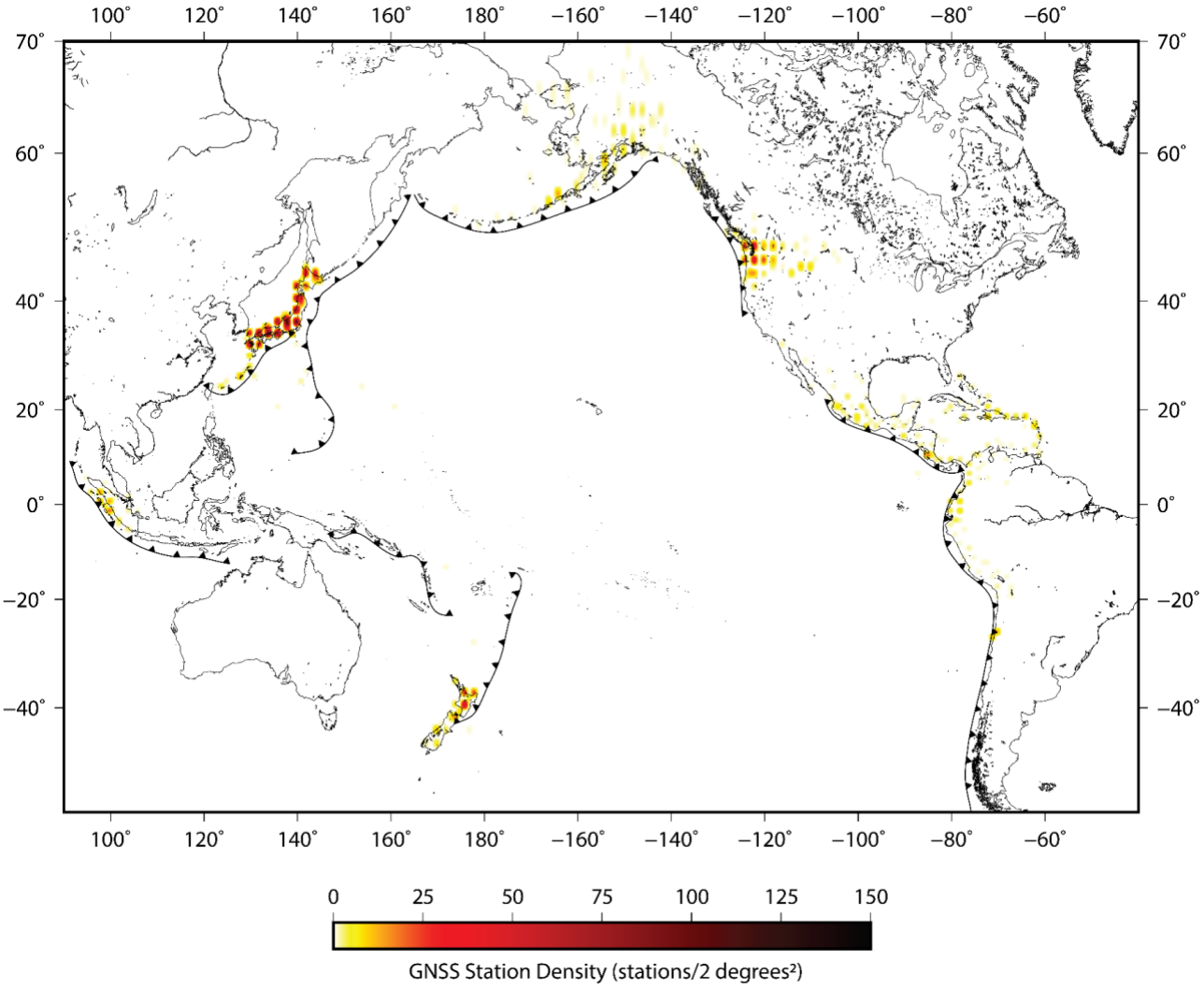

FIGURE S2.1: MAP OF GNSS STATION DENSITY FOR EACH SUBDUCTION ZONE OF INTEREST.

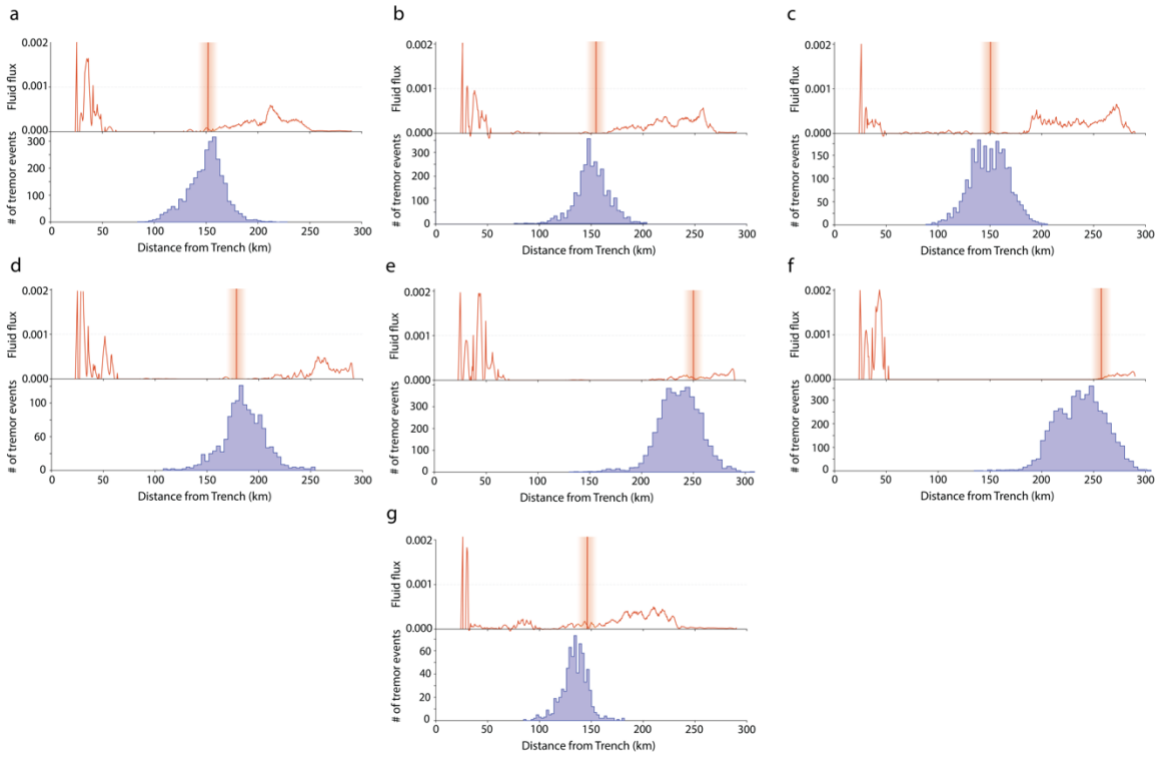

FIGURE S3.1: TOTAL FLUID FLUX ($KG \cdot M^{-3} \cdot YR^{-1}$) ESTIMATES FOR PROFILES (A) 2; (B) 3; (C) 4; (D) 6; (E) 7; (F) 8; (G) 10. ESTIMATED LOCATION OF THE MWC IS SHOWN BY VERTICAL ORANGE LINE WITH ERROR BOUNDS REPRESENTED BY THE SHADED REGION.

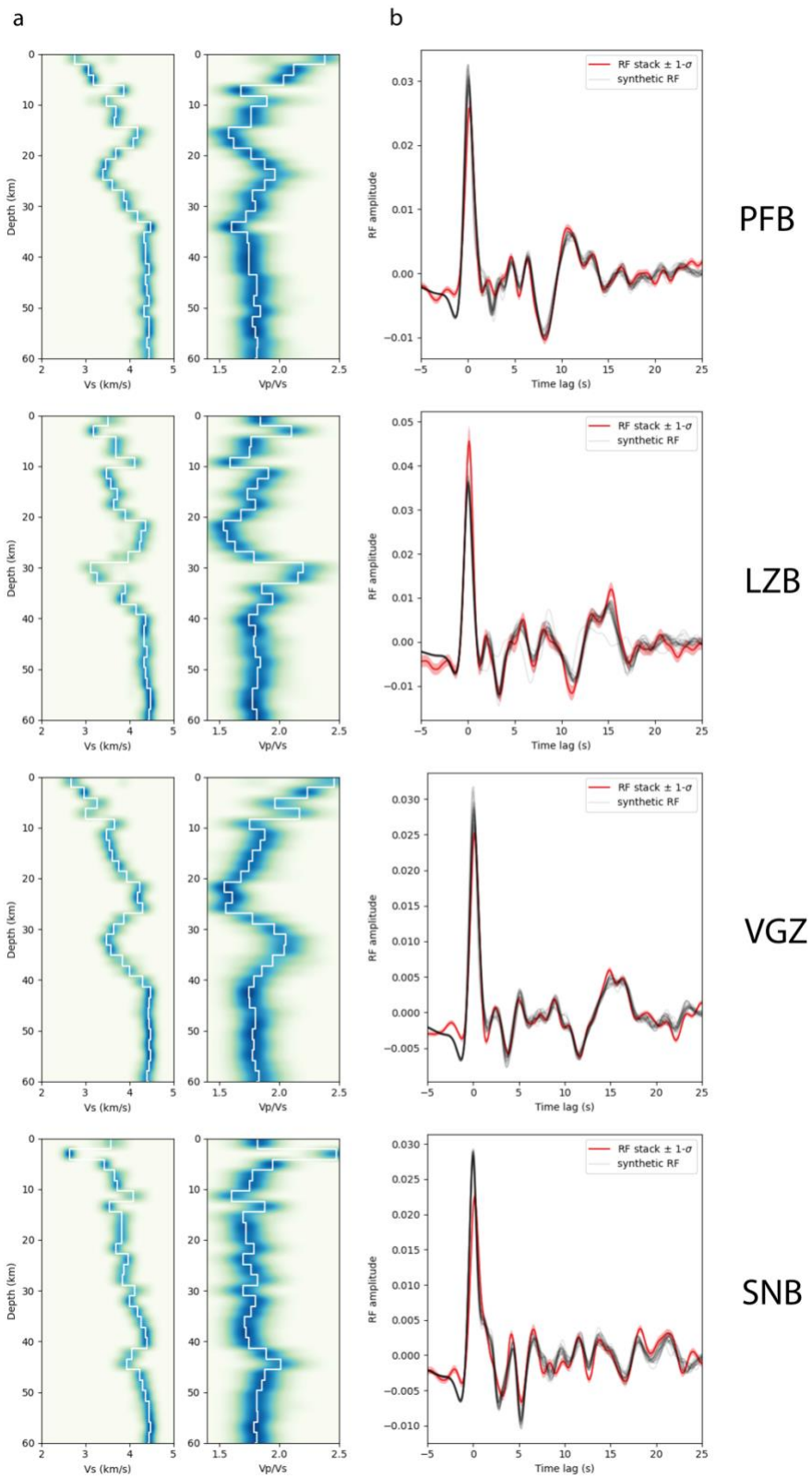

FIGURE S4.1: RESULT OF 1D INVERSION FOR REMAINING STATIONS ANALYSED. LEFT PANEL SHOWS VS AS A FUNCTION OF DEPTH WHILE RIGHT PANEL SHOWS VP/VS RATIO. (B)BEST FIT PREDICTED RF PLOTTED WITH OBSERVED RF STACK.